FACULTY OF SCIENCE
UNIVERSITY OF COPENHAGEN

Ph.D. Thesis

High resolution water isotope data from ice cores

By:

Vasileios Gkinis

Academic supervisor:
Sigfus J. Johnsen

Submitted 03/10/2011

Abstract

We here present a new technique for the measurement of water isotope ratios in an online fashion using Cavity Ring Down spectroscopy in the Near Infra Red region. The technique reaches a level of precision comparable or better to what can be achieved with traditional Mass Spectrometry achieving very low instrumental drifts. Attached to an ice core melter the system can offer water isotope measurements of unprecedented resolution. We demonstrate the feasibility of the technique by deploying the system on the Greenland ice sheet during the NEEM ice core project. The online nature of the data calls for a different approach regarding data analysis. We outline the methods we use in order to put the water isotope time series on a depth scale. Based on a step response analysis we are able to derive transfer functions that describe the attenuation of signals with different wavelengths. Allan variance analysis is also used to assess the precision and long term stability of the analytical system. Results are compared to discrete samples and an overall agreement is observed.

The high resolution obtained with this technique can be useful for temperature reconstructions based on the study of the isotopic diffusion in firn. In this work we describe the process of water isotope firn diffusion and derive expressions for the diffusion length. Based on a diffusivity parametrization and a series of different temperature history scenarios we are able to model the diffusion length history. Spectral estimation techniques applied on the time series can yield the diffusion length value. We show how this is practically done and exemplify it by using available water isotope high resolution data from Dome C. We compare the model and data outcome and based on that we infer past isotope slopes for the last 90 kyr for the Dome C site. Our results indicate a variable isotope slope during this period. The temperature history inferred from the estimated isotope slope shows a glacial– interglacial step of approximately 9 °K and warming events during Marine Isotope Stages 3 and 4 that reach Holocene levels in terms of temperature.

,

Contents

List of Figures

Acknowledgements

The work that I am presenting here benefited from the support and input of various people. During the last years, Dorthe Dahl Jensen and Jørgen Peder Steffensen put significant efforts to create a working environment based on creativity, openness and free interaction between individuals on all levels. This environment has been very beneficial for the development and the implementation of the ideas presented here and for that I would like to express my gratitude to them. In particular the NEEM ice core drilling project gave me the chance to perform measurements in the field and collaborate with researchers with long experience in Continuous Flow Analysis systems. The contributions of Mathias Biggler and Simon Schüpbach have been extremely valuable, during the operation of the experimental system in Greenland as well as during the writing phase of both papers included here. The very constructive critique of professor James White and Bruce Vaughn was beneficial for the quality of the presented work and was a very important motivation for me during the years. Bo Møllesøe Vinther, Sebastian Bjerregaard Simonsen and Christo Buizert were the "usual suspects" with whom I could share ideas, excitement and occasional frustration about water isotope diffusion modelling, gas thermometry reconstructions and firn densification, while Sussane Lilja Buchardt was always there to give me the last updates on accumulation reconstructions and dating for the NEEM ice core. Trevor James Popp and Christopher Stowasser have been two very influential companions during this project and without them this work as well as my life in Copenhagen would have been very different. The time I spent with them in the field, the lab, as well as during the off - work hours have been very important for me. In a personally difficult moment Inger Seirstad introduced me to Sigfus Johnsen and supported my decision to move to Copenhagen for this project. Without her this thesis would not have been written. Dànjal à Neystabø and Nina Mourier, have from different roles been the two most important links to the life out of the academic environment and I would like to thank them both for that. During the last and rather lonely months of writing the music of Tom Waits, Hildur Guðnasdóttir, J. S. Bach and Jolie Holland conquered my headphones and kept me going...thanks guys.

It is common of course for a student to thank his supervisor for his excellent supervision and scientific input. Sigfus stands behind most, if not all of the work presented here. He has been the main influence during the development of the experimental work included in this thesis showing a remarkable ability to offer valuable scientific input for instrumentation as modern as the cavity ring down spectrometer. His idea of utilizing a glass capillary for the water isotope measurements I present here, is based on his elegant and most important simple way of thinking. His intervention on my work has not been frequent and was

done at the right moments with the right way, bringing me back on track if I had deviated or boosting my work and productivity at those "low" moments. This approach also helped me stand on my feet and work independently. But the case with Sigfus is also a little bit different. This is because the gratitude I am expressing here does not concern only the actual scientific input and supervision. It also concerns the attitude towards science, research and mostly life in general. The moments of joy over a cold beer or delicious food and the feeling of togetherness Sigfus and his wife Pàllinà created for us over numerous occasions. I don't know if I was a good student but I have the feeling that some of Sigfus' words will follow me for life and for that I would like to thank him as a supervisor and mostly as a friend.

Chapter 1

Introduction

In this work we deal with high resolution water isotope records from ice cores. This thesis is divided into two parts. The main research challenge that is addressed in the first part, is to investigate the possibility of performing water isotopic analysis of ice cores in a continuous way. When this work was initiated, continuous online measurements with the use of ice core melters had been performed for chemical impurities. Some examples of this can be found in the work of Sigg et al. (1994) and Röthlisberger et al. (2000).

The standard method for the measurement of water isotope ratios from ice cores had up to that point been the use of mass spectrometry combined with a variation of methods for the sample preparation, as described in chapter 2. These measurements were performed in a discrete fashion by cutting ice core samples that were subsequently melted and preped for the mass spectrometry measurements. Based on the research questions to be addressed these samples were cut in various resolutions. For an ice core that is 2-3 km long, this process can yield tens of thousands of ice core samples. The time required to complete the sampling and the water isotope analysis can be as long as several years.

In the same time, cavity ring down infra red spectroscopy that had already been applied successfully for the measurement of various molecules in the gas phase, became commercially available. Our interest was to use a commercially available spectrometer in combination with an existing melter, previously used for the distribution of liquid sample for the purpose of chemical impurities measurements in ice cores. As the ice core melter system distributes a continuous stream of liquid sample, while in the same time the laser spectrometer performs measurements in a continuous flow of gaseous sample, it becomes apparent that for the purpose of the measurement under consideration we needed an interface system that can continuously vaporize the liquid water stream. That itself constitutes a critical experimental challenge as incomplete phase changes result in isotopic fractionation.

Our approach was to use a continuous evaporation system that assures complete evaporation and avoids any isotopic fractionation effects. With simple experiments involving the vaporizer, the laser spectrometer and meteoric waters in liquid form, we assessed the accuracy, the precision and long term stability of the technique. During this first stage the ice core melting procedure was not considered and our aim was to perform experiments and validate our data by using the simplest setup possible. Considering though that ultimately our goal

was to perform high resolution isotopic analysis, we performed step response tests that allowed us to obtain an estimate of the attenuation caused by the vaporizer and the laser spectrometer. One step further, influenced by already published results by Brand et al. (2009), we investigated the response of the laser spectrometer to different levels of injected water vapor sample. This led to a set of correction coefficients that were later applied on actual ice core measurements in order to account for varying levels of water sample in the system.

The overall results were promising and set the experimental and theoretical foundation on which ice core measurements were later performed and post processed. The procedures we followed during this first stage are outlined in chapter 2. This work has been published in *Isotopes in Environmental and Health Studies* (Gkinis et al., 2010).

Acquiring real ice core data required the use of an ice core melter and a sample debubbling and distribution system. The NEEM ice core drilling project served as the ideal platform for this project. First because it made real ice core samples available and second because a Continuous Flow Analysis (CFA) system was deployed in the field for the purpose of chemical impurities measurements. We collaborated closely with the Continuous Flow Analysis (CFA) team towards addressing the technical issues regarding sample distribution. Our approach was to introduce as few changes to the CFA side as possible, while reducing our sample size demands to the minimum possible without altering the performance of the analytical system. Several sections of the NEEM ice core were measured with our system in high resolution and precision.

The post processing of the online water isotope data posed some particular challenges that we had to overcome. The two main challenges we faced concerned the conversion of the time scale at which the data were acquired to a properly calibrated depth scale based on the monitoring of the melting procedure. One additional problem that had to be solved was to correctly estimate the signal attenuation caused by the total sampling and measurement procedure. Using a set of numerical methods and experiments we were able to accurately determine the depth scale of several measured sections of the NEEM core. Comparison with discrete samples from the same depth allowed for characterization of the analytical system in terms of resolution, from the point of melting until the optical cavity of the spectrometer. We quantify the resolution via the estimation of the diffusion length and derive transfer functions that describe the attenuation of signals with different wavelengths.

We describe this work in chapter 3, which is a version of the manuscript that was submitted in *Atmospheric Measurement Techniques* (Gkinis et al., 2011). The manuscript has been reviewed for publication in *Atmospheric Measurement Techniques* and we are currently processing a revised version following the guidelines of the reviews.

Chapter 4 deals with work that is currently still in progress. Contrary to the concise way chapters 2 and 3 are written as they were prepared for submission to peer reviewed journals, in chapter 4 we follow an in depth approach describing the work that has been done in the subject of water isotope firn diffusion. During this project, we built on the work that has been done over years by Sigfus J. Johnsen on the subject and we use a combination of models and data to further investigate the possibility of using the method for paleotemperature reconstructions. The feasibility of such an effort is very much dependent on the availability and accuracy of past accumulation reconstructions and dating

models. For the particular case of NEEM, only preliminary versions of these estimates are available due to the fact that the water isotope record is still incomplete.

It is obvious that the development of a new thermometry method has a great interest from a technical point of view. One can question though what is the knowledge gained from the paleoclimate perspective. For that reason we look into a specific open question that can yet not be addressed by the currently available temperature reconstruction methods. This case concerns the temperature evolution of the Dome C site on the east Antarctic plateau. Based on the results of gas isotopic studies, borehole temperature reconstructions and stable water isotope models, there appears to be a lack of consensus as to how the temperature over Dome C has evolved during the past 100,000 years. In chapter 4 we present a preliminary temperature history for the past 90,000 years based on the study of water isotope firn diffusion as estimated from high resolution stable isotope data. Commenting on the findings of our estimates, we conclude that this is not a conclusive study and propose further research that can help to refine the results of the study.

Finally in chapter 5 and based on the work that has already been conducted the author presents his ideas for the future. These ideas concern development of new analytical techniques for ice core measurements, further processing of high resolution data and modelling approaches for development and validation of the water isotope diffusion paleothermometer.

Chapter 2

Calibration of an IR cavity ring down spectrometer

Published in *Isotopes in Environmental and Health Studies*; Refer to Gkinis et al. (2010)

Abstract

A new technique for high resolution simoultaneous isotopic analysis of δ^{18}O and δD in liquid water is presented. A continuous stream flash evaporator has been designed that is able to vaporise a stream of liquid water in a continuous mode and deliver a stable and finely controlled water vapour sample to a commercially available Infra Red Cavity Ring Down Spectrometer. Injection of sub μl amounts of the liquid water is achieved by pumping liquid water sample through a fused silica capillary and instantaneously vaporizing it with a 100% efficiency in a home made oven at a temperature of 170^{o}C. The system's simplicity, low power consumption and low dead volume together with the possibility for automated unattended operation, provides a solution for the calibration of laser instruments performing isotopic analysis of water vapour. Our work is mainly driven by the possibility to perform high resolution on line water isotopic analysis on Continuous Flow Analysis systems typically used to analyze the chemical composition of ice cores drilled in polar regions. In the following we describe the system's precision and stability, sensitivity to varying levels of sample size and we assess the observed memory effects. A test run with standard waters of different isotopic composition is presented, demonstrating the ability to calibrate the spectrometer's measurements on a VSMOW scale with a relatively simple and fast procedure.

2.1 Introduction

High precision stable isotope analysis of water is typically performed offline via discrete sampling with traditional isotope ratio mass spectrometry (hereafter IRMS). While high precision and accuracy can routinely be achieved with IRMS

systems, water isotope analysis remains an elaborate process, which is demanding in terms of sample preparation, power consumption, sample size, consumable standards, and carrier gases. In the most common IRMS techniques, water molecules are not measured as such, but are converted to a different gas prior to measurement. For $\delta^{18}O$ analysis, the CO_2 equilibration method Epstein (1953) has been widely used, whereas δD analysis commonly involves the reduction of water to hydrogen gas over hot uranium Bigeleisen et al. (1952); Vaughn et al. (1998) or chromium Gehre et al. (1996).

However, combined use of these methods rules out simultaneous analysis of both water isotopologues on a given sample. More recently , in combination with continuous flow mass spectrometers, conversion of water to CO and H_2 is performed in a pyrolysis furnice Begley and Scrimgeour (1997); Gehre et al. (2004) and allows simultaneous measurement, but still on a discrete sample.

Laser spectroscopy at the near and mid infrared regions has been demonstrated as a potential alternative for water isotope analysis, presenting numerous advantages over IRMS Kerstel et al. (1999); Iannone et al. (2009a). A major advantage of the technique is the ability to directly inject the sampled water vapour in the optical cavity of the spectrometer where both isotopic ratios $^{18}O/^{16}O$ and $^{2}H/^{1}H$ are simultaneuously measured. Nowadays, commercial IR spectrometers are available with a precision comparable to IRMS systems Lis et al. (2008); Brand et al. (2009). These units typically receive a continuous stream of water vapour sample and offer ease of use and portability.

The problem of the calibration of an IR spectrometer for isotopic analysis of water vapour has been addressed in the past by other studies. Wang et al Wang et al. (2009) calibrated an IR - spectrometer in an Off - Axis Integrated Cavity Output (OA - ICOS) configuration by monitoring the differences between a measured and a theoretically predicted Rayleigh distillation curve. In order to obtain a saturated gas stream they make use of a dew point generator. This approach requires precise measurement of the total time of the Rayleigh distilation process. The initial and final masses of the liquid water standard used, also need to be measured. The time required for the process to complete depends on the required precision and is of the order of 12-24 hours.

A different approach to the problem, is the generation of water vapour with known isotopic composition, by introducing liquid water standards in a dry gas stream, preferably at high temperatures. In this case, immediate 100% evaporation is essential in order to avoid isotopic fractionation effects. Proper control of the injected amount of liquid water and the dry gas flow is essential for a stable water mixing ratio, while it can in principle allow for tuning of the system to different humidity levels. A dripper device, used by Lee et al Lee et al. (2005) introduced liquid water in a heated evaporation chamber filled with high purity nitrogen. The device operates in the range 800-30,000 ppm and delivers water vapour sample to a direction absorption spectrometer operating in the mid IR region (6.66 μm). Iannone et al Iannone et al. (2009b), use a piezoelectric microdroplet generator Ulmke et al. (2001) in order to inject sub μl amounts of water in a stream of dry gas where 100% evaporation takes place. The sample is then forwarded to a V-shaped high reflectivity cavity in an Optical Feedback - Cavity Enhanced Absorption Spectroscopy (OF-CEAS) configuration Morville et al. (2005); Kerstel et al. (2006). Aiming for in situ isotopic analysis of water vapour in the Upper Troposphere - Lower Stratosphere region where water mixing ratios are extremely low, the latter system is optimised in the range

between 12 and 3500 ppm. Both evaporation systems use a relatively large volume, (order of mL) static liquid water reservoir as a sample (or standard) source.

The motivation of this study lies in the area of ice core research with the goal to develop a system that can perform on line δD and δ^{18}O isotopic analysis on a liquid sample stream originating from a continuously melting ice rod. Similar melting systems have been developed and used in lab or field environments for the analysis of chemical impurities or gases entrapped in the ice core Fuhrer et al. (1993); Kaufmann et al. (2008); Schüpbach et al. (2009). In this way, it is possible to perform measurements with high resolution when compared to equivalent measurements performed on discrete samples. Portability, low power consumption and cost have been parameterers that were considered for this system.

2.2 Experimental

2.2.1 NIR Cavity Ring Down Spectroscopy

Water molecules present spectral absorption lines in the area of mid and near infra red due to ro-vibrational (fundamental and overtone) transitions. At low sample pressures, the absorption lines are narrow enough to permit distinction between different isotopologues. These spectral features are unique and their relative intensities can be linked to relative isotopic abundances, hence providing the necessary information to calculate isotopic ratios. For a comprehensive description on the various optical techniques and analysis of the signals in IR spectroscopy as applied for isotopic analysis, the reader may refer to Kerstel (2005). In this study we use a commercial IR spectrometer purchased from Picarro Inc. ($L1102-i$) Gupta et al. (2009).

For high signal to noise ratio at a relatively low water concentration, the spectrometer utilises a high finesse cavity in a Cavity Ring Down (CRDS) configuration Crosson (2008) . In a typical CRDS experiment the laser light is coupled into the optical cavity and stays in resonance until the intensity builds up to a maximum value. The light source is then turned off and the light intensity in the cavity decays exponentially as photons "leak" through the mirrors of finite reflectivity. The result is that every photon completes thousands of roundtrips in the cavity, thus interacting with the injected absorbing sample through a path length of the order of kilometers. The time constant of this decay, commonly refered to as "ring down time", depends only on the reflectivity of the mirrors $\mathcal{R}$, the length of the cavity l_c and the absorption coefficient of the selected absorption feature $\alpha(\nu)$ Berden et al. (2000). The ring down time is described in Eq. 3.5. Absorption spectra can thus be derived by the measurement of τ at different emmision wavenumbers ν.

$$\tau(\nu) = \frac{l_c}{c\left[(1-\mathcal{R}) + \alpha(\nu)\, l_c\right]} \tag{2.1}$$

In our system the IR spectrometer operates in a continuous flow-through mode, maintaining a cavity pressure of 35 Torr at a gas sample flow rate of $\approx 30\ mL/min$ at STP via two PID controlled proportional valves up and downstream of the optical cavity.

The temperature of the cavity is regulated at 80 ^{o}C. The acquisition rate of the instrument is one data point in ≈6 seconds.

2.2.2 Sample preparation

We implement a continuous liquid water stable isotope analysis by converting a stream of liquid water to water vapour and thereafter introducing the latter into the optical cavity of a NIR-CRDS spectrometer. A sketch of the system is given in Figure 2.1. Different liquid water samples (or standards) can be selected via a 6 port selection valve (V1). Transfer of the sample is done using a peristaltic pump that maintains a liquid flow rate of 0.1 ml/min over the sample line. This flow rate can be adjusted according to the needs of the application or potential sample limitations. High purity Perfluoroalkoxy (PFA) tubing with an ID of 0.5 mm is used in this section.

A water level in the range of 17,000 - 22,000 ppmv in the optical cavity results in optimum spectrometer performance. With a nominal gas flow rate of 30 mL/min STP and a concentration of 20,000 ppmv the required injection rate is $\approx 0.5\mu L/min$ of liquid water. In order to introduce this- quantity of liquid water in the oven, we split off a fraction of the main sample line through a fused silica capillary. The split takes place in a PEEK Tee split with ⌀0.5 mm bore (T1 in Figure 2.1).

The small ID of the capillary tube acts as a restriction that imposes a back pressure at T1. In order to balance the capillary back pressure we apply a restriction on the waste line downstream of the T1 Tee by using tubing with an ID smaller than the ⌀0.5 mm of the main sample line. Assuming laminar flow, an estimate of the pressure build up along a tube is given by the Hagen-Poiseuille law as described in Eq. 2.2.

$$\Delta p = \frac{8\eta L Q}{\pi r^4} \tag{2.2}$$

Where Δp is the pressure drop along a tube with length L and inner diameter 2r and Q is the volumetric flow rate of the fluid with dynamic viscosity η.

Proper selection of length and inner diameter for the waste line and capillary tubes balances the two back pressures and offers a way to tune the flow rates through the capillary. At steady state the flow through the capillary (Q_c) will be

$$Q_c = Q_w \frac{L_w r_c^4}{L_c r_w^4} \approx Q_m \frac{L_w r_c^4}{L_c r_w^4} \tag{2.3}$$

where Q_w and Q_m the flow of liquid sample at the waste and main line respectively. Due to the strong dependance of Q_c on the inner diameter α of the tubes, the latter serve as a first order control on the flow through the capillary. Typical values for α_c and α_w are 20 μm and 150 μm respectively. Considering a fixed value for the length of the capillary L_c ($L_{cap} = 15cm$), the linear dependance of Q_c on Q_m and L_w allows for fine tuning of the flow by varying the length of the tube at the waste line and the flow rate on the peristaltic pump. A detailed view on the liquid sample handling and the tubing sizes involved is presented in Figure 2.2.

The sample evaporation step is critical as 100% immediate evaporation is essential in order to avoid isotopic fractionation effects. The evaporation oven

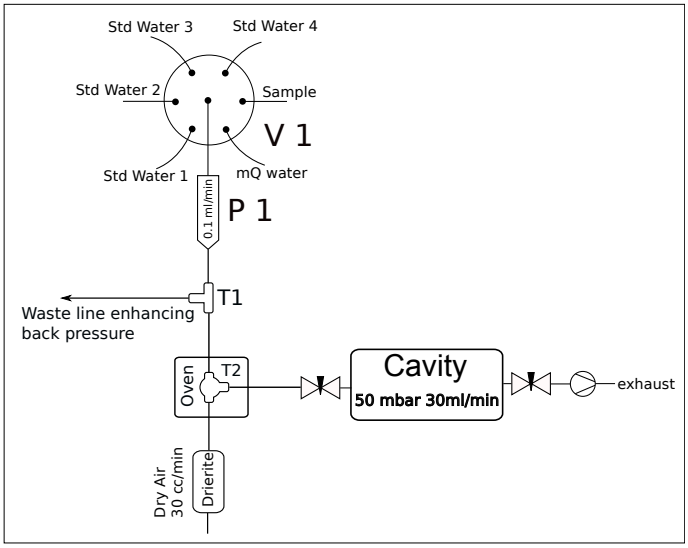

Figure 2.1: Block diagram of the CFA-CRDS system

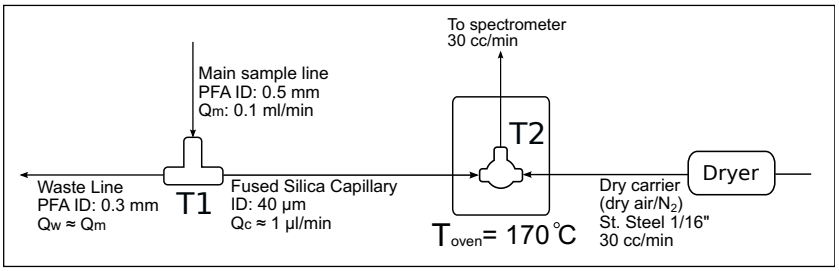

Figure 2.2: Detailed section of the sample split

consists of a a stainless steel Valco Tee-split (Valco ZT1M) (T2 in Figure 2.1), attached on top of an aluminum block measuring $40 \times 40 \times 30$ mm. The bore space in the Tee-split ($\varnothing$0.5 mm) serves as the evaporation chamber. We maintain a temperature of 170 ^{o}C by means of a PID controlled 200 W cartidge heater (Omega CSH-201200) fixed in the aluminum block. A temperature reading is obtained with a K type thermocouple. High temperature conductive paste is used in all of the connections of the evaporation chamber to ensure optimal heat distribution.

Upon evaporation of the liquid sample in the oven, mixing with dry air takes place, forming the gas sample with the desired water vapour levels. Atmospheric air is dried through a $^{\text{TM}}$Drierite canister ($CaSO_4$). Typical water levels for the dry gas are below 100 ppm water concentration. For the transfer of dry gas to the evaporation chamber we use stainless steel 1/16" diameter tube. The mixture of dry gas and water vapor is transfered to the spectrometer at the nominal flow rate of 30 cc/min via a 1/16" stainless steel tube that is heated to $\approx 90^o$C in order to avoid recondensation of water vapour on the walls of the tube.

Overall our approach is towards minimizing dead volume in the system, thus

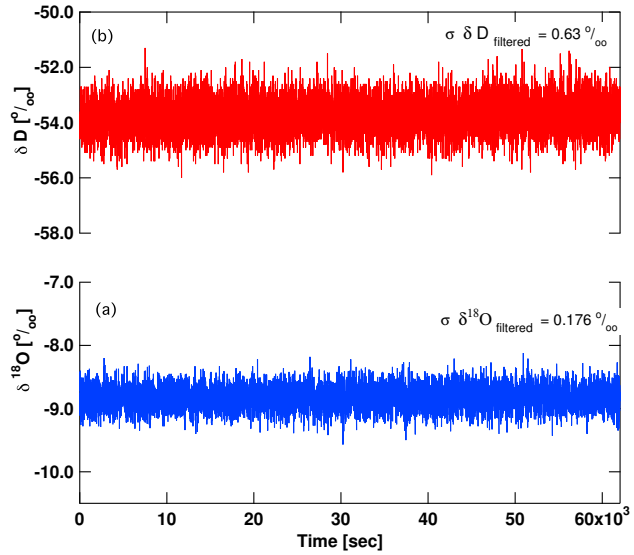

Figure 2.3: Injection of DI water over the period of 17 h. Results for δD (a) and δ^{18}O (b).

reducing sample dispersion and limiting memory effects, while at the same time we ensure efficient evaporation and negligible fractionation of the water sample.

2.3 Results and Discussion

2.3.1 System Stability - Allan Variance

We investigate the behavior of the spectrometer in combination with the sample preparation system, regarding possible instrumental drift during long operation. Injection of de-ionised water from a 5-liter bottle takes place for a period of ≈16 hours. The level of water vapour in the cavity during this period is 19510 ± 154 ppm [1σ]. Results of the test are presented in Figure 2.3. This test was performed with an acquisition rate of ≈1 data point every 6 sec. In a second stage we set the data on a fixed time step of 6 sec by means of linear interpolation.

We perform a "clean-up" of the raw data by removing outliers that deviate more than $\pm 3\sigma$ from the mean value of the run. For a total of 9551 points, we rejected 17 and 5 outliers for δ^{18}O and δD respectively. We observe that extreme outliers are likely to occur during sudden and short term interruption of the water sample delivery. Small bubbles or other impurities in the water stream are likely to cause such effects. Noisy and frequently interupted delivery of sample to the spectrometer can deteriorate the measuring performance of the system.

Assuming that data points are normally distributed then a mean and variance for this distribution are defined as:

$$\bar{\delta} = \frac{1}{N}\sum_{i=1}^{N}\delta_i \tag{2.4}$$

$$\sigma_{\delta}^2 = \frac{1}{N-1}\sum_{i=1}^{N}\left(\delta_i - \bar{\delta}\right)^2 \tag{2.5}$$

For sample size N the standard error of the mean can be calculated as:

$$\sigma_{\bar{\delta}}^2 = \left(\frac{\partial\bar{\delta}}{\partial\delta}\,\sigma_{\delta}\right)^2 = \frac{1}{N}\,\sigma_{\delta}^2 \tag{2.6}$$

Equation 2.6 implies that in the theoretical case of a zero drift system, one can progressively decrease the standard deviation of the mean by increasing the integration time of the measurement. However, apparent instrumental drifts are bound to limit the benefits of averaging a signal over long integration times.

In order to assess the stability of the system we follow an approach similar to Werle et al. (1993) and Czerwinski et al. (2009) by calculating the Allan variance Allan (1966) for the time series presented in Figure 2.3. A time series of sample size N can be devided in m subsets of sample size $k = \frac{N}{m}$. If the acquisition time per data point is t_i then the integration time for every subset is $\tau_m = kt_i$. The Allan variance can then be defined as:

$$\sigma_{Allan}^2(\tau_m) = \frac{1}{2m}\sum_{j=1}^{m}\left(\bar{\delta}_{j+1} - \bar{\delta}_j\right)^2 \tag{2.7}$$

where $\bar{\delta}_{j+1}$ and $\bar{\delta}_j$ are the mean values of neighboring intervals j and $j+1$.

In Figure 2.4 we plot the calculated Allan variance with different integration times for δ^{18}O and δD . For integration times up to about $\tau_{opt} = 5000$ sec the Allan variance decreases linearly for both isotopologues. This linear behavior suggests a white noise signal and further averaging can lead to an improvement in the detection level of the system. However for integration times longer than τ_{opt} averaging is not expected to improve the detection levels any further due to apparent instrumental drifts. Practically, for the purpose of calibration it is unlikeley that averaging times longer than ≈ 600 sec will be implemented. As a result the optimum performance of the system at τ_{opt} is not fully exploited. However the value of τ_{opt} for both δ^{18}O and δD indicates a stable performance for both the spectrometer and the sample preparation line with a precision comparable or better to mass spectrometry systems used for δ^{18}O and δD isotopic analysis. This behavior is due to the optimised control of the spectrometer's cavity temperature and pressure and the smooth and finely controlled evaporation and delivery of the water vapour sample.

2.3.2 Dependance on humidity levels

We investigate the response of the system to different levels of injected water sample. The pump rates of P1 are tuned in subsequent steps to 13 different humidity levels spanning a range between 3.5 - 25 kppm. We acquire data for $\approx$600 sec per humidity level and select sections of these intervals according to

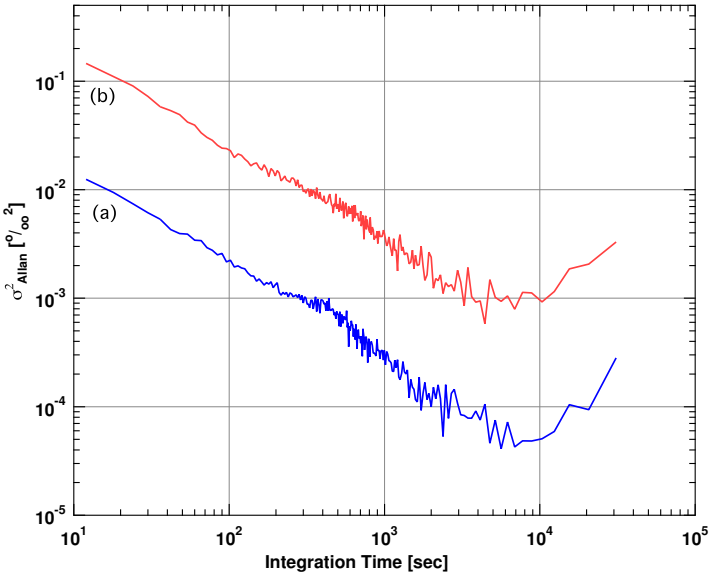

Figure 2.4: Allan variance plots for δD (a) and δ^{18}O (b) from the data in Figure 2.3

their quality. The mean δ values of these sections are plotted as red and blue circles for δD and δ^{18}O respectively at the bottom part of Figure 2.5. The points are fitted with a 3$^{\text{rd}}$ order polynomial plotted in black. Error bars refer to $\pm 1\sigma$ as calculated separately for every section. At the top of Figure 2.5 we present the water levels of a concatenated series of the different sections used.

From the fitted curves in Figure 2.5 we observe an overall linear response of δ^{18}O to different water levels. This is however not the case for δD which shows a strong non-linearity at the low humidity area. For both isotopologues, the uncertainty of the measurement shows a rapid increase below 5000 ppm. In order to correct our measurements for possible fluctuations of the injected water sample, we focus on the linear response area between 15 - 22 kppm. A linear fit on the data, is presented in Figure 2.6. For each data point the correction term $\Delta\delta_{hum}$ will be given by:

$$\Delta\delta_{hum} = \lambda \cdot (R_{20} - 1) \tag{2.8}$$

Where $R_{20} = \frac{[\mathrm{H_2O}]_{ppm}}{20000_{ppm}}$ and λ is estimated from the linear regression:

$$\lambda_{18} = 1.94 \text{ ‰} \qquad \lambda_D = 3.77 \text{ ‰}$$

So for a deviation of 1000 ppm

$$\Delta\delta^{18}\mathrm{O} = 0.097 \text{ ‰} \qquad \Delta\delta\mathrm{D} = 0.19 \text{ ‰}$$

Brand et al Brand et al. (2009) have performed a similar calibration using water samples injected in a discrete mode with a commercially available sample preparation line that consists of an autosampler and a liquid vaporizer Gupta et al. (2009). A comparison of the two data sets and the calibration lines shows a good agreement over the whole range of humidities.

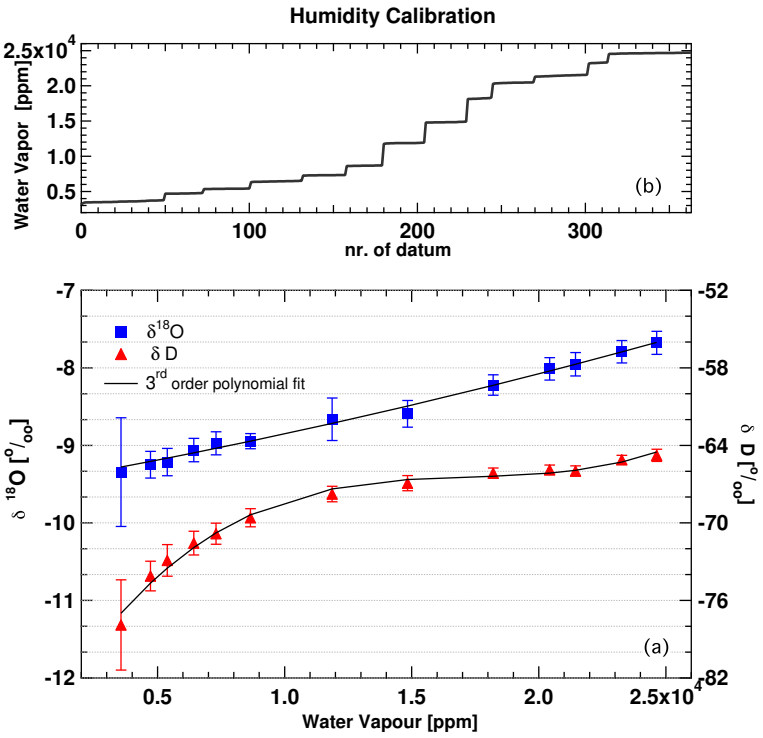

Figure 2.5: Humidity calibration. The averages of the isotopic values for each section are plotted as squares for δ^{18}O and triangles for δD in graph (a). Data are fitted with a third-order polynomial regression model (solid lines). The error bars represent $\pm$ 1σ of each processed section. In (b) we plot the humidity levels of each section.

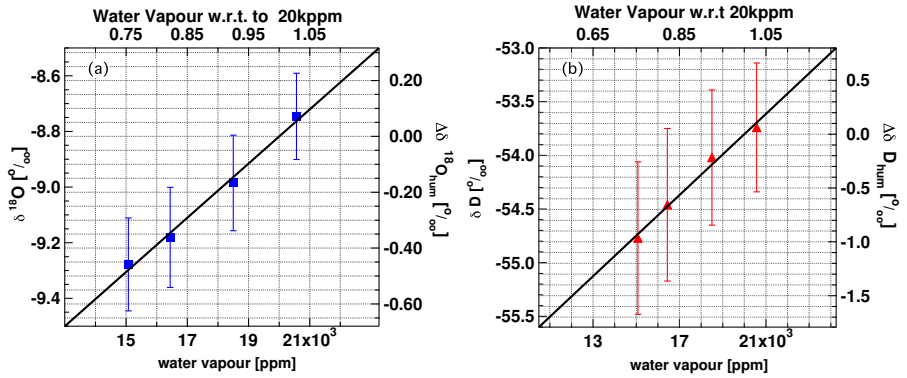

Figure 2.6: Linear section of humidity calibration. The averages of each humidity level section are plotted as squares (a) and triangles (b) for δ^{18}O and δD ,respectively. Error bars represent a $\pm$ 1σ of each section.

2.3.3 Memory effects

The continuous flow of liquid and gaseous sample in the transfer lines, the evaporation chamber and the optical cavity of the spectrometer result in apparent dispersion effects. These effects impose a cross talk between samples commonly refered to as "memory effects". In the case of isotopic analysis performed in a discrete mode the memory effect influencing the j$^{\text{th}}$ analysis of the run depends on the isotopic value of the n previous analyses weighted by a set of memory coefficients So, if the expected value for the j$^{\text{th}}$ analysis is δ_j^r and the measured equivalent is δ_j^m, then the memory effect M$_{\text{j}}$ is described as:

$$\begin{aligned} \delta_j^r &= \delta_j^m + M_j \\ M_j &= \sum_{k=1}^{n} \varphi_k (\delta_j - \delta_{j-k}) \end{aligned} \tag{2.9}$$

Determination of the memory coefficients is used to characterize the experimental system and to correct the measured isotopic values for observed memory effects.

In the case of continuous measurements we follow a slightly different approach. We generate an isotopic step by switching between two standard waters with different isotopic composition. This results in a smoothed sigmoid curve (Figure 2.7) .

Ideally, in the case of zero dispersion, a switch between two standards would be described by a scaled and shifted version of the the Heaviside unit step function as:

$$S(t) = \begin{cases} C_2 & t < 0 \\ C_1 H(t) + C_2 & t \geq 0 \end{cases} \tag{2.10}$$

where the valve switch takes place at $t = 0$, $H(t)$ is the Heaviside unit step function and C_1 and C_2 refer to the amplitude and base line level of the isotopic

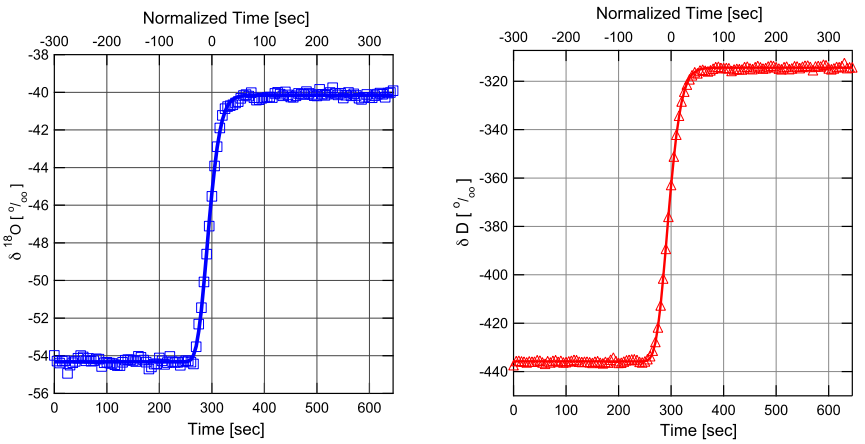

Figure 2.7: Raw δ^{18}O and δD data during the valve switch between standard water DC02and 40 are plotted with squares and triangles, respectively. We t a lognormal distribution model for δ^{18}O (a) and δD (b).

step. The effect of smoothing can be seen as the convolution of $S(t)$ with a smoothing function $\mathcal{G}$.

$$m(t) = [S * \mathcal{G}](t) \tag{2.11}$$

where $m(t)$ is the measured signal. The derivative of the signal $\frac{dm}{dt}$ yields the impulse response of the system as:

$$\frac{dm}{dt} = \frac{dS}{dt} * \mathcal{G} = C_1 \frac{dH}{dt} * \mathcal{G} = C_1 \delta_{Dirac} * \mathcal{G} \tag{2.12}$$

We fit the obtained data with a scaled version of the cumulative distribution function of a Log Normal distribution described as

$$\delta_{model}(t) = \frac{K_1}{2}\left[1 + \mathrm{erf}\left(\frac{\ln t - t_{valve}}{S\sqrt{2}}\right)\right] + K_2 \tag{2.13}$$

where we estimate values for K_1, K_2, t_0 and S by means of a least square optimization (Figure 2.7). The fit parameters are used to normalise the isotopic step. Based on the latter we then calculate the impulse response of the system as described in Eq. 2.12

As $t = t_{valve} = 0$ we consider the time at which the normalised step is equal to 0.5 and accordingly normalise the time scale (Figure 2.8). The impact of the memory effects on the impulse response is visualised as the ratio $\mathcal{R}(t)/\mathcal{R}(t=0)$, calculated for $t \geq 0$ (Figure 2.9). One can see that 40 sec after the introduction of the δ_{Dirac} pulse its effect on the measured signal is below 10%. Beyond that point the noise level of the measurement does not allow for any conclusions regarding the memory efects.

2.3.4 Runs with 4 standards - VSMOW Calibration

Reporting of water isotopic measurements requires a proper calibration of the results on the VSMOW scale. This, in combination with the observed instrumental drift, implies the necessity for a frequent VSMOW calibration. In the

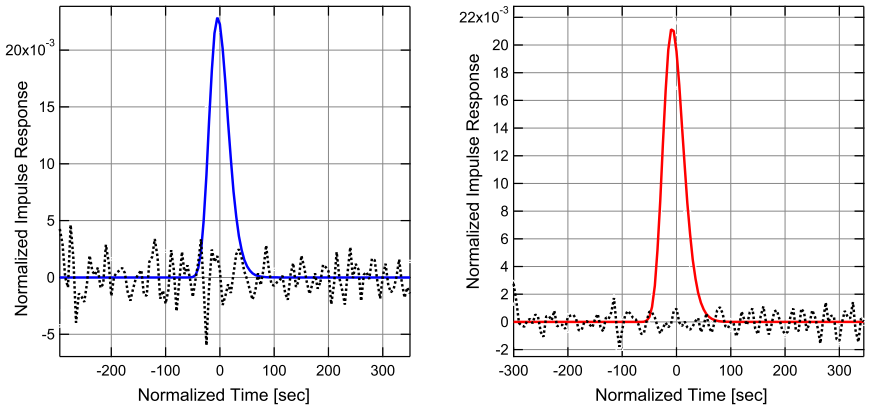

Figure 2.8: Response of the system on an isotopic δ_{Dirac} pulse for δ^{18}O (a) and δD (b) introduced at $t = 0$.The dotted lines represent the residuals of the t.

following experiment we inject 5 samples of different isotopic composition spanning a range from -9‰ to -54‰ for δ^{18}O (-60‰ to -428‰ for δD). The set of samples consists of Copenhagen de-ionised water (CPH-DI) and a selection of 4 local standards. The latters' isotopic composition has been precisely measured with respect to VSMOW and SLAP waters on an IRMS with a high temperature conversion system (HTC). The water delivery is tuned to 19000 ppm well within the linear response area. During the whole run ($\approx$ 2 h), humidity levels varied with a $\sigma_{[\text{H}_2\text{O}]} = 617$ ppm.

The raw data of the experiment are presented in Figure 2.10. Before any further processing, a humidity calibration of the data is performed by scaling all data points to the level of 20000 ppm in the same fashion as described in the previous section. We choose sections of 35 data points ($\approx$ 4 min) for every separate injection of a sample. Based on two of those sections and in combination with the values obtained by the HTC system we calculate the coefficients of a VSMOW calibration line as described by:

$$\delta_{\text{VSMOW}} = a_{\text{VSMOW}} \cdot \delta_{\text{measured}} + b_{\text{VSMOW}} \tag{2.14}$$

The sections are carefully selected in order to exclude data affected by memory effects occuring for some seconds after the valve switch between samples. The results of the measurements are presented in table 2.1. The final values are compared to the values of the samples as measured on the HTC mass spectrometer system. The overall precision of the system for δD and δ^{18}O is below 0.5 ‰ and 0.1 ‰ respectively. The average of the differences between the CFA - CRDS and the HTC system is -0.05 ‰ for δ^{18}O and -0.42 ‰ for δD .

Sample ID	δD [‰]	$\bar{\delta}$D Span	δD_{HTC} $\delta D_{HTC} - \bar{\delta}D$
CPH-DI	-60.33	-60.26	-
CPH-DI	-60.18	0.1	-
-22	-167.66	-168.03	-168.4
-22	-168.40	0.52	-0.37
Crete	-260.70	-260.94	-261.9
Crete	-261.19	0.34	-0.96
-40	-309.13	-309.57	-310
-40	-310.00	0.62	-0.44
DC02	-427.31	-427.58	-427.5
DC02	-427.85	0.38	0.08
Std. dev all			**0.39**
$\delta D_{HTC} - \bar{\delta}D$ all			**-0.42**
Sample ID	δ^{18}O [‰]	$\bar{\delta}^{18}$O Span	$\delta^{18}O_{HTC}$ $\delta^{18}O_{HTC} - \bar{\delta}^{18}O$
CPH-DI	-8.69	-8.70	-
CPH-DI	-8.70	0.01	-
-22	-21.9	-21.92	-21.9
-22	-21.93	0.02	0.02
Crete	-33.57	-33.54	-33.64
Crete	-33.52	0.04	-0.1
-40	-39.69	-39.83	-39.97
-40	-39.98	0.2	-0.14
DC02	-54.08	-54.11	-54.08
DC02	-54.14	0.04	0.03
Std. dev all			**0.06**
$\delta^{18}O_{HTC} - \bar{\delta}^{18}O$ all			**-0.05**

Table 2.1: Results of the 4 Standards Experiment

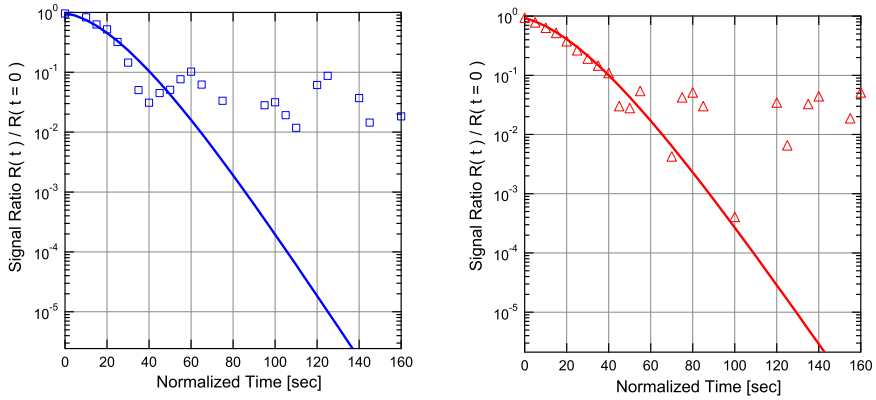

Figure 2.9: Quantication of the memory effect for δ^{18}O (a) and δD (b). R(t) refers to the amplitude of the impulse response of the system at time t for the model (solid lines) and the raw data (squares and triangles).

2.4 Conclusions and Outlook

We have demonstrated the feasibility of on-line liquid water isotopic measurements by interfacing a low volume continuous stream flash evaporator to a Cavity Ring Down Infra Red spectrometer. We have assesed the performance of the system regarding precision, accuracy, possible instrumental drifts, memory effects and dependancy on varrying humidity levels. The observed instrumental drifts are minimal, thus allowing for reasonable sampling times. Additionally, the humidity dependance of the system is easily corrected via a careful and repeatable calibration procedure.

We have also indicated a procedure to calibrate the measured isotopic ratios on the VSMOW scale using local standard waters. The system's precision is comparable to that of modern mass spectrometry measurement systems tailored for water isotope analysis.

The use of the system is oriented towards the area of high resolution on-line continuous isotopic analysis of ice cores. The low power consumption and portability, offer the possibility for field operation. The proposed calibration technique can be performed in $\approx$ 30 min, it requires a small amount of water ($\approx$ 2-3 ml per standard) and can in principle be automated. Dispersion and memory effects are expected to smooth the acquired signals thus reducing the resolution that can be obtained with this technique. Consequently a careful determination of the systems resolution is essential as a next step towards continuous ice core measurements. Further reduction of the volume of the transfer lines prior to the optical cavity can potentially improve the system to that end.

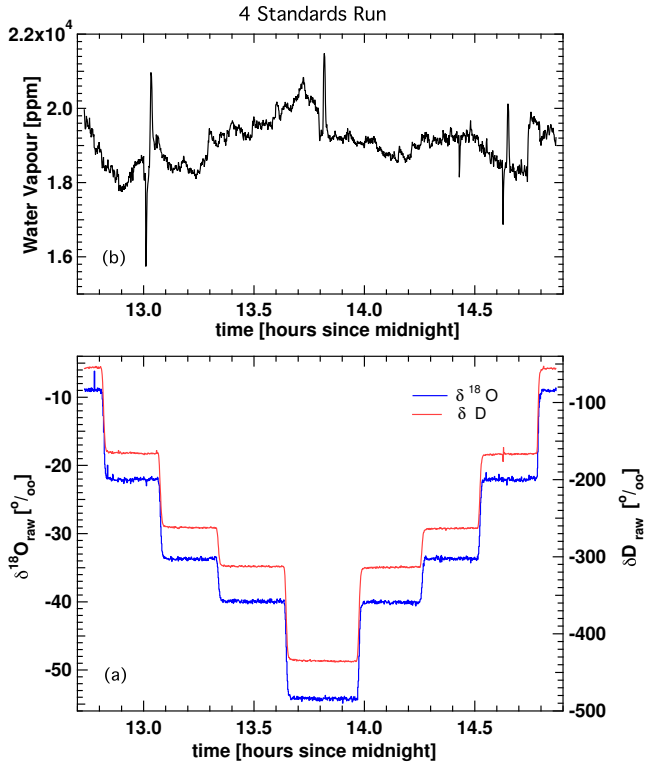

Figure 2.10: Raw measurements of δ^{18}O and δD for ve waters of different isotopic composition are plotted in graph (a) with blue and red lines, respectively. The raw data of the humidity levels in the cavity are plotted in(b).

Chapter 3

Water isotopic ratios from a continuously melted ice core sample

Abstract

A new technique for on-line high resolution isotopic analysis of liquid water, tailored for ice core studies is presented. We build an interface between an Infra Red Cavity Ring Down Spectrometer (IR - CRDS) and a Continuous Flow Analysis (CFA) system. The system offers the possibility to perform simultaneuous water isotopic analysis of δ^{18}O and δD on a continuous stream of liquid water as generated from a continuously melted ice rod. Injection of sub μl amounts of liquid water is achieved by pumping sample through a fused silica capillary and instantaneously vaporizing it with 100% efficiency in a home made oven at a temperature of 170^{o}C. A calibration procedure allows for proper reporting of the data on the VSMOW scale. We apply the necessary corrections based on the assessed performance of the system regarding instrumental drifts and dependance on humidity levels. The melt rates are monitored in order to assign a depth scale to the measured isotopic profiles. Application of spectral methods yields the combined uncertainty of the system at below 0.1‰ and 0.5‰ for δ^{18}O and δD respectively. This performance is comparable to that achieved with mass spectrometry. Dispersion of the sample in the transfer lines limits the resolution of the technique. In this work we investigate and assess these dispersion effects. By using an optimal filtering method we show how the measured profiles can be corrected for the smoothing effects resulting from the sample dispersion. Considering the significant advantages the technique offers, i.e. simultaneuous measurement of δ^{18}O and δD , potentially in combination with chemical components that are traditionally measured on CFA systems, notable reduction on analysis time and power consumption, we consider it as an alternative to traditional isotope ratio mass spectrometry with the possibility to be deployed for field ice core studies. We present data acquired in the framework of the NEEM deep ice core drilling project in Greenland, during the 2010 field

[1]Accepted to *Atmospheric Measurement Techniques*; Refer to Gkinis et al. (2011)

season.

3.1 Introduction

Polar ice core records provide some of the most detailed views of past environmental changes up to 800,000 years before present, in large part via proxy data such as the water isotopic composition and embedded chemical impurities. One of the most important features of ice cores as climate archives, is their continuity and the potential for high temporal resolution. Greenland ice cores are particularly well suited for high resolution paleoclimatic studies, because relatively high snow accumulation rates allow seasonal changes in proxy data to be identified more than 50,000 years in the past (Johnsen et al., 1992; members, 2004).

The isotopic signature of polar precipitation, commonly expressed through the δ notation (Epstein, 1953; Mook, 2000) is related to the temperature gradient between the evaporation and condensation site (Dansgaard, 1964) and has so far been used as a proxy for the temperature of the cloud at the time of condensation (Jouzel and Merlivat, 1984; Jouzel et al., 1997; Johnsen et al., 2001). One step further, the combined signal of δD and δ^{18}O commonly referred to as the deuterium excess (hereafter D_{xs}), constitutes a usefull paleothermometer tool. Via it's high correlation with the temperature of the evaporation source (Johnsen et al., 1989) , it has been used to resolve issues related to changes in the location of the evaporation site (Cuffey and Vimeux, 2001; Kavanaugh and Cuffey, 2002). A relatively recent advance in the use of water isotope ratios as a direct proxy of firn temperatures, is introduced by Johnsen et al. (2000) . Assessment of the diffusivity of the water isotopologues in the porous medium of the firn column can yield a temperature history, provided a dating model is available.

The measurement of water stable isotopic composition is typically performed off-line via discrete sampling with traditional isotope ratio mass spectrometry (hereafter IRMS). While high precision and accuracy can routinely be achieved with IRMS systems, water isotope analysis remains an elaborate process, which is demanding in terms of sample preparation, power consumption, sample size, consumables and standard and carrier gases. The analysis of a deep ice core at its full length in high resolution (typically 2.5 to 5 cm per sample) requires the process of a vast amount of water samples and can take years to complete. Additionally, these procedures often come at the expense of not fully exploiting the temporal resolution available in the ice core.

Laser spectroscopy in the near and mid infrared region has been demonstrated as a potential alternative for water isotope analysis, presenting numerous advantages over IRMS (Kerstel et al., 1999; Kerstel, 2005) . A major advantage of the technique is the ability to directly inject the sampled water vapour in the optical cavity of the spectrometer where both isotopic ratios $^{18}O/^{16}O$ and $^{2}H/^{1}H$ are measured simultaneuously. In contrast, in the most common IRMS techniques water is not measured as such, but has to be converted to a different gas prior to measurement. For δ^{18}O analysis, the CO_2 equilibration method (Epstein, 1953) has been widely used, whereas δD analysis commonly involves the reduction of water to hydrogen gas on hot uranium (Bigeleisen et al., 1952; Vaughn et al., 1998; Huber and Leuenberger, 2003). However, the combined use of these two

methods rules out simultaneous analysis of both water isotopologues on a given sample. More recently, in combination with the use of continuous flow mass spectrometers, conversion of water to CO and H_2 is performed in a pyrolysis furnice (Begley and Scrimgeour, 1997) and allows simultaneous δD and δ^{18}O measurement, but still on a single discrete sample. Nowadays, commercial IR spectrometers are available with a precision comparable to IRMS systems (Lis et al., 2008; Brand et al., 2009). These units typically receive a continuous stream of water vapor and offer ease of use and portability.

The analysis of another set of ice core proxies, that of chemical impurities, has similary been an elaborate process, traditionally performed with liquid chromatography techniques. With the advent of Continuous Flow Analysis (heareafter CFA) from continuously melted ice core segments, the measurement of chemical impurities has reached the point of largely exploiting the high resolution available in the core while it is often performed in the field (Sigg et al., 1994; Röthlisberger et al., 2000; Kaufmann et al., 2008). The continuous, online nature of the technique has resulted in a considerable reduction in sample preparation and processing times. Recently, Schüpbach et al. (2009) demonstrated the measurement of CH_4 mixing ratios in an on-line semi continuous mode with the use of a gas chromatograph combined with a pulsed discharge and a thermal conductivity detector.

Here, we demonstrate the ability to perform continuous measurements of water isotope ratios from a stream of water vapor derived from a continuously melting ice rod by coupling a commercial IR spectrometer to a CFA system via a passive, low volume flash evaporatotion module. In the following, we assess the system's precision, accuracy, and efficient calibration. We then comment on issues related to sample dispersion in the sample transfer lines, the evaporation module and the optical cavity of the spectrometer itself in order to determine the expected smoothing imposed on the acquired data sets. Finally, isotopic analysis of ice core samples from the NEEM deep ice core are presented and compared to measurements performed in discrete mode.

3.2 Experimental

3.2.1 Continuous Flow Analysis

In the system described here, (Figure 3.1) an ice rod measuring 3.2 $\times$ 3.2 $\times$ 110 cm (hereafter CFA run) is continuously melted on a copper, gold - nickel coated melter at a regulated temperature of 20 °C. A stainless steel weight sitting on top of the ice rod enhances the stability and continuity of the melting process. An optical encoder connected to the stainless steel weight, records the displacement of the rod. This information is used to accurately define the depth scale of the produced water isotope data. Breaks in the ice rod are logged prior to the melting process and accounted for, during the data analysis procedure.

In order to avoid contamination of the chemistry measurements, only the melt water from the inner part of the core is used for further analysis. The sample is pumped from the melter by means of a peristaltic pump (P1 in Figure 3.1) at a flow rate of 16 ml/min. Gases included in the water stream originating from the air bubbles in the ice core are extracted in a sealed debubbler, with a volume of $\approx$300 μl. The melt rate of the present system is approximately 3

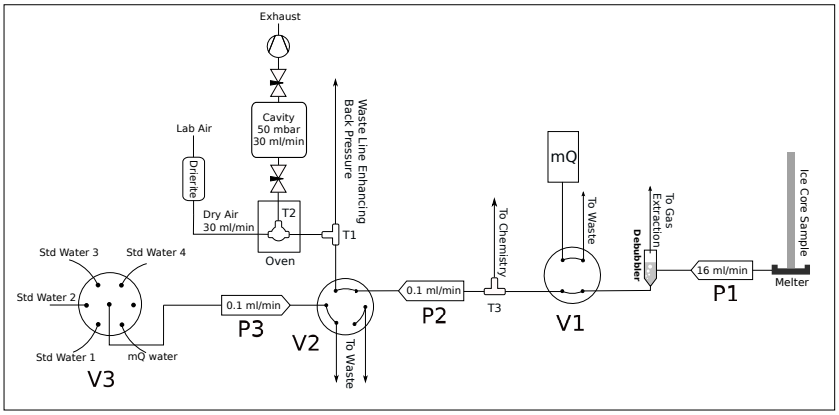

Figure 3.1: Block diagram of the CFA-CRDS system

cm/min, thus resulting in an analysis time of ≈35 min per CFA run. During the intervals between CFA runs, mQ water is pumped through the system. A 4-port injection valve (V1 in Figure 3.1) allows the selection between the mQ and sample water. For further details on the analysis of chemical components or the extraction of gases for greenhouse gas measurements the reader is refered to Kaufmann et al. (2008) and Schüpbach et al. (2009) .

3.2.2 The water isotope measurement

We follow the same approach as previously presented in Gkinis et al. (2010) by coupling a commercially available Cavity Ring Down IR spectrometer (hereafter IR-CRDS) purchasecd by Picarro Inc. (Picarro L1102 - i) (Crosson, 2008) . The spectrometer operates with a gas flow rate of 30 sml/min at a cavity pressure of 47 mbar maintained with two proportional valves in a feedback loop configuration up and down - stream of the optical cavity at a temperature of 80 °C. The high signal to noise ratio achieved with the Cavity Ring Down configuration in combination with fine control of the environmental parameters of the spectrometer, result in a performance comperable to modern mass spectrometry systems taylored for water stable isotope analysis.

A 6-port injection valve (V2 in Figure 3.1) selects sample from the CFA line or a set of local water standards. The isotopic composition of the local water standards is determined with conventional IRMS and reported with respect to VSMO water. A 6-port selection valve (V3 in Figure 3.1) is used for the switch between different water standards. A peristaltic pump (P3 in Figure 3.1) in this line with variable speeds, allows adjustment of the water vapor concentration in the spectrometer's optical cavity, by varying the pump speed. In that way, the system's sensitivity to different humidity levels can be investigated and a calibration procedure can be implemented. We use high purity Perfluoroalkoxy (PFA) tubing for all sample transfer lines.

Injection of water sample into the evaporation oven takes place via a $\varnothing 40\mu$m fused silica capillary where immediate and 100% evaporation takes place avoiding any fractionation affects. The setpoint of the evaporation temperature is set to 170 °C and is regulated with a PID controller. The amount of the injected

water to the oven can be adjusted by the pressure gradient maintained between the inlet and waste ports of the T1 tee-split (Figure 3.1). The latter depends on the ratio of the inner diameters of the tubes connected to the two ports as well as the length of the waste line. The total water sample consumption is ≈ 0.1 ml/min maintained by the peristaltic pump P2 (Figure 1). For a detailed description of the sample preparation and evaporation module the reader may reffer to Gkinis et al. (2010) . A smooth and undisturbed sample delivery to the spectrometer at the level of ≈ 20000 ppm results in optimum performance of the system. Fluctuations of the sample flow caused by air bubbles or impurities are likely to result in a deteriorated performance of the measurement and are occasionally observed as extreme outliers on both δ^{18}O and δD measurements. The processes that control the occurence of these events are still not well understood.

3.3 Results and Discussion - From raw data to isotope records

In this study we present data collected in the framework of the NEEM ice core drilling project. Measurements were carried out in the field during the 2010 field season and span 919.05 m of ice core (depth interval 1281.5 - 2200.55). Here we exemplify the performance of the system over a section of 16.5m of ice. The age of this section spans ≈ 411 years with a mean age of 10.9 ka b2k. The reported age is based on a preliminary time scale constructed by stratigraphic transfer of the GICC05 time scale (Rasmussen et al., 2006) from the NGRIP to the NEEM ice core.

In Figure 3.2 we present an example of raw data as acquired by the system. This data set covers 7 CFA runs (7.70 m of ice). A clear baseline of the isotopically heavier mQ water can be seen in between CFA runs. At $t = 1.9 \cdot 10^4$ sec one can observe a sudden drop in the signal of the water concentration due to a scheduled change of the mQ water tank. Adjacent to this, both δ^{18}O and δD signals present a clear spike, characteristic of the sensitivity of the system to the stability of the sample flow rates.

3.3.1 VSMOW - Water concentration calibrations

Before any further processing we correct the acquired data for fluctuations of the water concentration in the optical cavity. To a good approximation the system shows a linear response to differences in water levels around 20000 ppm (Brand et al., 2009; Gkinis et al., 2010). A correction is performed as:

$$\Delta\delta = a(R_{20} - 1) \tag{3.1}$$

Here $R_{20} = \frac{[\mathrm{H_2O}]}{20000}$, $a_{18} = 1.94‰$ and $a_D = 3.77‰$ as estimated in Gkinis et al. (2010)

Raw data are expressed in per mil values for both δ^{18}O and δD and ppm for the water vapour concentration. These values are based on the slope and intercept values of the instrument's stored internal calibration line. Due to apparent instrumental drifts though, the latter are expected to deviate with time. To overcome this problem we perform frequent VSMOW calibrations by

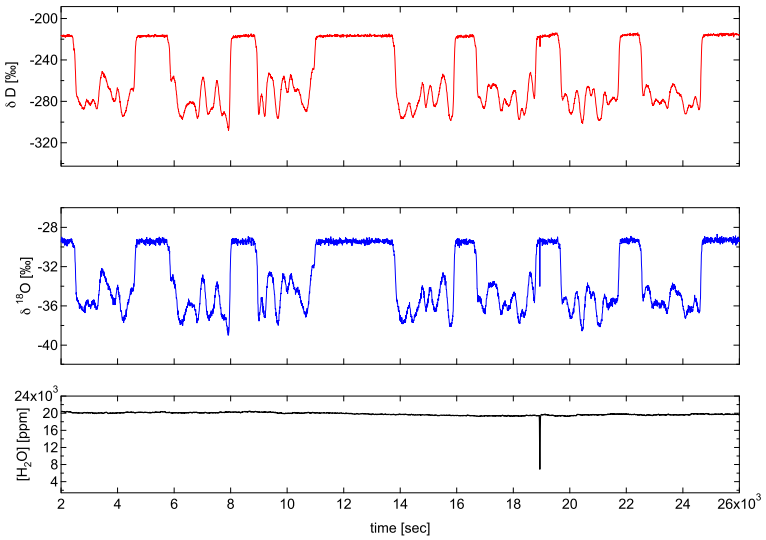

Figure 3.2: Raw signals spanning 7 CFA runs on 29/05/2010

using local water standards with well known δ^{18}O and δD values measured by conventional Isotope Ratio Mass Spectrometry combined with a pyrolysis glassy carbon reactor (Thermo DeltaV - TC/EA).

3.3.2 The depth scale

The melting process is recorded by an optical encoder connected to the top of the stainless steel weight that lies on top of the ice rod. The data acquired by the optical encoder allow for a conversion of the time scale to a depth scale. In order to locate the beginning and end of every run we take advantage of the isotopic step observed during the transition between mQ baseline and sample water. A smoothed version of the discrete derivative of the acquired isotope data for both δ^{18}O and δD reveals a local minimum (maximum) for the beginning (end) of the measurement (Figure 3.3). The logged depth of the top and the bottom of the CFA run is assigned to these points. Data that lie in the transition interval between mQ and sample water are manually removed from the series. Additional breaks within a CFA run that can possibly be created during the drilling or processing phase of the ice core, are taken into account at the last stage of the data analysis. If necessary and depending on their size, the gaps can be filled by means of some interpolation technique. Here, due to the small size of the gaps we use a linear interpolation sceme. The use of more advanced methods is also possible but is out of the scope of this work. The processed profiles presented in Figure 3.3 are reported with a nominal resolution of 5 mm. The interpolated sections are highlighted with gray bars. Their width indicates the length of the gaps.

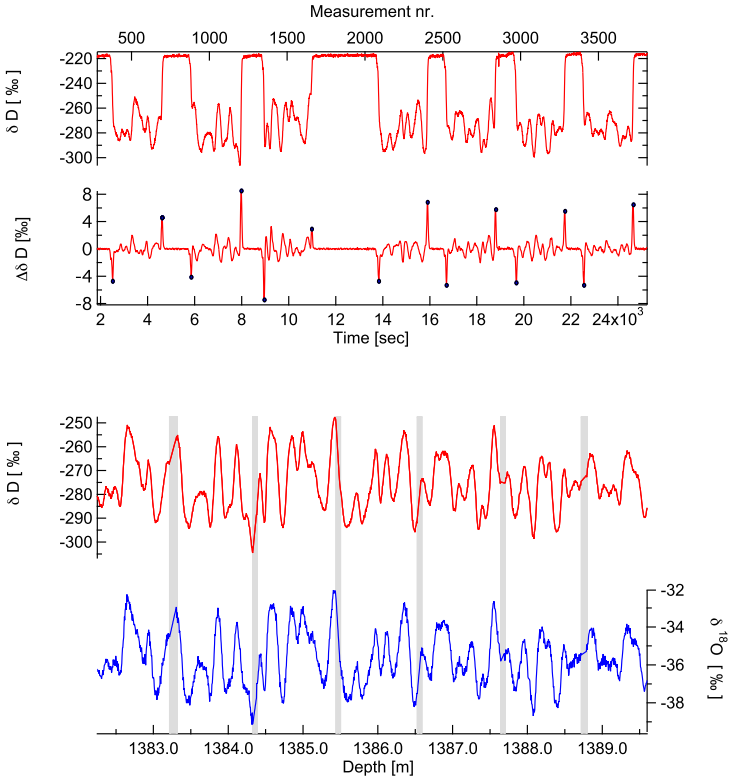

Figure 3.3: The beginning and end of each CFA run is determined by the extrema of the 1^{st} derivative of the isotopic signal, presented on the top graph; With gray bars we indicate the position and width of sections with data that are missing due to breaks in the ice, or removed in order to account for the transition from mQ water to sample and vice cersa.

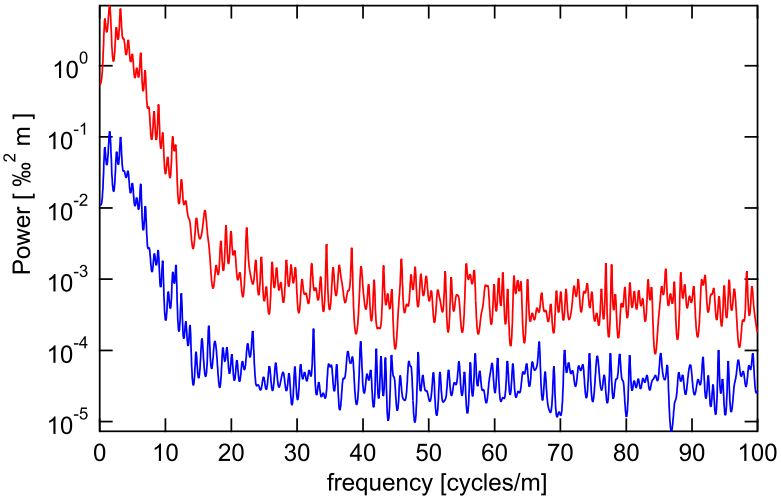

Figure 3.4: δ^{18}O and δD power spectral density.

3.3.3 Noise level - Accuracy

An estimate of the noise level of the measurements, can be obtained from the appropriately normalized power spectral density of the time series. Here we implement an autoregressive spectral estimation method developed by Burg (1975) by the use of the algorithm introduced by Andersen (1974) . The order of the autoregressive model is M = 300, though implementations with a lower number of autoregressive coefficients can perform equally well. The standard deviation of the time series will be defined as:

$$\sigma^2 = \int_{-f_c}^{f_c} |\hat{\eta}(f)|^2 df \tag{3.2}$$

where the Nyquist frequency is $f_c = 100$ cycles/m and $|\hat{\eta}(f)|^2$ can be obtained by a linear fit on the flat high frequency part of the spectrum (Figure **??**). By performing this analysis we obtain $\sigma_{18} = 0.055$‰ and $\sigma_D = 0.21$‰.

In order to validate the quality of the calibrations as well as the estimated depth scale we compare the CFA data with measurements performed in a discrete fashion using the same IR-CRDS spectrometer in combination with a sample preparation evaporator system (Gupta et al., 2009) and an autosampler. The discrete samples are cut in a resolution of 5 cm. The sample injection sequence takes into account apparent memory effects and results are reported on the VSMOW scale by appropriate calibration using local water standards. The results are illustrated in Figure 3.5 for δ^{18}O and δD . The comparison of the data sets demonstrates the accuracy of the CFA-CRDS measurement and therefore the validity of the followed calibration procedures. The benefits of the technique in terms of achieved resolution can be seen when one compares the two datasets over isotopic cycles with relatively small amplitude and higher frequency. Such an example can be seen at the depth of 1390.5 m where a sequence of 4 cycles is sampled relatively poorly with the discrete method when

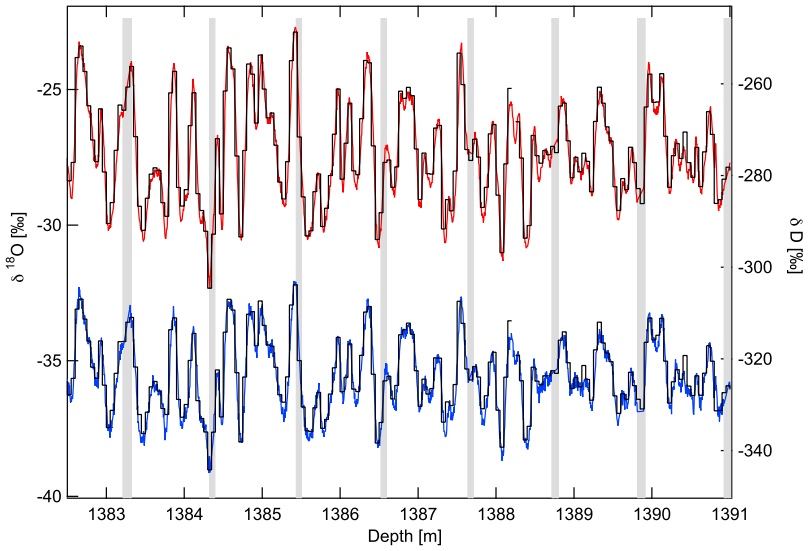

Figure 3.5: Comparison CRDS-CFA with 5 cm discrete samples for δD (top) and δ^{18}O (bottom); Bars indicate the position and width of sections with missing/removed data

compared to the on-line system. This performance can benefit studies that look into the spectral properties of the signals by providing better statistics for the obtained measurements.

3.3.4 Obtained resolution - Diffusive sample mixing

One of the advantages of the combined CFA - CRDS technique for water isotopic analysis of ice cores, lies in the potential for higher resolution measurements relative to discrete sampling. However, diffusion effects in both the liquid and the vapor phase, are expected to attenuate the obtained resolution.

Attenuation of the initial signal of the precipitation occurs also via a combination of in situ processes that take place after deposition. The porous medium of the firn column allows for an exchange of water molecules in the gas phase along the isotopic gradients of the profile. For the case of polar sites, this process has been studied extensively (Johnsen, 1977; Whillans and Grootes, 1985) and can be well described and quantified provided that a good estimate of the diffusivity coefficient and a strain rate history of the ice core site are available (Johnsen et al., 2000) . The process ceases when the porous medium is closed-off and the diffusivity of air reaches zero, at a density of $\approx$ 804 kgr/m. Deeper in the ice, diffusion within the ice crystals takes place via a process that is considerably slower when compared with the firn diffusion. At a temperature of -30 °C the diffusivity coefficients of these two processes differ by 4 orders of magnitude (Johnsen et al., 2000) .

Assuming an isotopic signal δ_{pr} for the precipitation, the total effect of the diffusive processes, insitu and experimental, can be seen as the convolution of

$\delta_{pr}(z)$ with a smoothing filter $\mathcal{G}_{tot}$.

$$\delta_m(z) = \int_{-\infty}^{\infty} \delta_{pr}(\tau)\,\mathcal{G}_{tot}(z-\tau)\,d\tau = [\delta_{pr} * \mathcal{G}_{tot}](z) \tag{3.3}$$

where $\delta_m(z)$ is the measured signal. Since instrumental and insitu firn-ice diffusion are statistically independent, the variance of the total smoothing filter is the sum of the variances of the insitu and experimental smoothing filters (hereafter $\mathcal{G}_{firn},\ \sigma_{firn},\ \mathcal{G}_{cfa},\ \sigma_{cfa}$).

$$\sigma_{tot}^2 = \sigma_{firn}^2 + \sigma_{cfa}^2 \tag{3.4}$$

It can be seen that any attempt to study firn and ice diffusion by means of ice core data obtained with an on-line method similar to the one we present here, requires a good assesment of the diffusive properties of the experimental system. The latter is possible if one is able to estimate the variance of the smoothing filter $\mathcal{G}_{cfa}$ expressed by the variance σ_{cfa}^2 (hereafter diffusion length).

One way to approach this problem is to measure the response of the system to a step function. Ideally, in the case of zero diffusion, a switch between two isotopic levels would be described by a scaled and shifted version of the the Heaviside unit step function as:

$$\delta_H(z) = \begin{cases} C_2 & z < 0 \\ C_1 H(z) + C_2 & z \geq 0 \end{cases} \tag{3.5}$$

where the isotopic shift takes place at $z = 0$, $H(z)$ is the Heaviside unit step function and C_1 and C_2 refer to the amplitude and base line level of the isotopic step. Convolution of the signal of equation 3.5 with $\mathcal{G}_{cfa}$ and subsequent calculation of the derivative yields,

$$\frac{d\delta_m}{dz} = \frac{d\delta_H}{dz} * \mathcal{G}_{cfa} = C_1 \frac{dH}{dt} * \mathcal{G}_{cfa} = C_1 \delta_{Dirac} * \mathcal{G}_{cfa} \tag{3.6}$$

Thus the derivative of the measured signal, properly normalized, equals the impulse respone of the system. Applying the Fourier transform, denoted by the overhead hat symbol, on equation 3.6, and by using the convolution theorem, we deduce the transfer function $\hat{\mathcal{G}}_{cfa}$ of the system:

$$\widehat{\frac{d\delta_m}{dz}} = C_1 \hat{\delta}_{Dirac} \cdot \hat{\mathcal{G}}_{cfa} = C_1 \cdot \hat{\mathcal{G}}_{cfa} \tag{3.7}$$

In the case of the system presented here, an isotopic transition can be observed when the main CFA valve (V1 in Figure 3.1) switches between mQ water and sample at the beginning and the end of each CFA run as shown in Figure 3.3. By using these transitions we are able to construct isotopic steps and estimate the impulse response of the system. Such an isotopic step is illustrated in Figure 3.6. We fit the data of Figure 3.6 with a scaled version of the cumulative distribution function of a normal distribution described as

$$\delta_{model}(z) = \frac{C_1'}{2}\left[1 + \mathrm{erf}\left(\frac{z - z_0}{\sigma_{step}\sqrt{2}}\right)\right] + C_2' \tag{3.8}$$

The values of $C_1',\ C_2',\ z_0$ and σ_{step} are estimated by means of a least square optimization and used accordingly to normalize the length scale and the isotopic

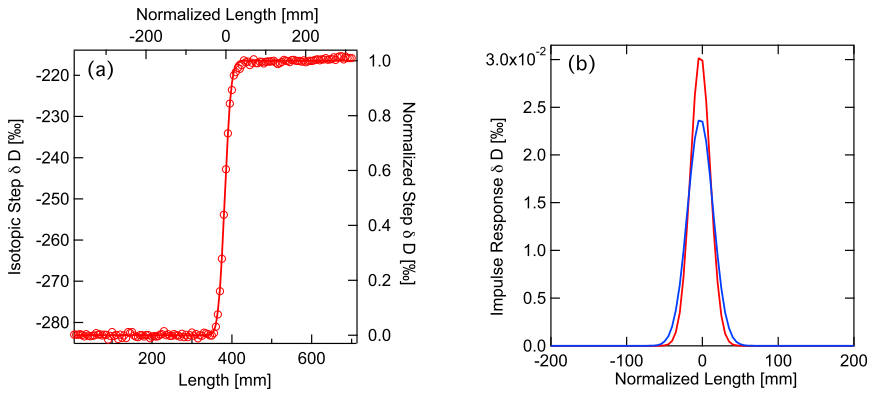

Figure 3.6: (a): Isotopic δD step. The length scale is normalized so normalized length = 0 when the normalized δD value equals 0.5‰. (b): Impulse Response of the system for δD based on the step response (red) and the spectral analysis (blue) with $\sigma_{cfa} = 13.4$ and 16.4 mm respectively

values of the step. A nominal melt rate of 3.2 cm/min is used for all the calculations presented here. We focus our analysis on the δD signal. The same approach can be followed for δ^{18}O . In Figure 3.6 we present the calculated impulse response of the system. The latter can be well approximated by a Gaussian type filter described as:

$$\mathcal{G}_{cfa}(z) = \frac{1}{\sigma_{cfa}\sqrt{2\pi}} e^{-\frac{z^2}{2\sigma_{cfa}^2}} \tag{3.9}$$

The diffusion length term σ_{cfa} is equal to 13.4 ± 0.17 mm $[1\sigma]$ as calculated with the least squares optimization. The transfer function for this filter will be given by its Fourier transform, which is itself a Gaussian and is equal to (Abramowitz and Stegun, 1964) :

$$\mathfrak{F}\left[\mathcal{G}_{cfa}(z)\right] = \hat{\mathcal{G}}_{cfa} = \int_{-\infty}^{\infty} \frac{1}{\sigma_{cfa}\sqrt{2\pi}} e^{-\frac{z^2}{2\sigma_{cfa}^2}} e^{-2\pi i f z} dz = e^{\frac{-k^2\sigma_{cfa}^2}{2}} \tag{3.10}$$

where $k = 2\pi f$. Harmonics with an initial amplitude A_0 and wavenumber k will be attenuated to a final amplitude equal to:

$$A = A_0 e^{\frac{-k^2\sigma_{cfa}^2}{2}} \tag{3.11}$$

An estimate of the transfer function based on the data and the cumulative distribution model is presented in Figure 3.8 (blue and pink curve respectively). As seen in this plot, cycles with wavelengths longer than 25 cm experience negligible attenuation, whereas cycles with a wavelength of 7 cm are attenuated by $\approx 50\%$.

The step response approach has been followed in the past for on-line chemistry data. In some studies such as Sigg et al. (1994) and Rasmussen et al. (2005) , the resolution of the experimental system was assessed via the estimation of the

transfer function. In other studies (Röthlisberger et al., 2000; Kaufmann et al., 2008) , the characteristic time in which a step reaches a certain level (typically 1/e) with respect to its final value, is used as a measure of the obtained resolution of the system. A common weakness of this approach as applied in the current, as well as previous studies, is that it is based on the analysis of a step that is introduced in the analytical system by switching a valve that is typically situated downstream of the melting and the debubbling system. Consequently, the impact of these last two elements on the smoothing of the obtained signals is neglected. In this study, this is the valve V1 in Figure 3.1.

To overcome this problem we will present here an alternative way, based on the comparison of the spectral properties of the on-line CFA data and the off-line discrete data in 5 cm sampling resolution, presented in section 3.2. In this approach the diffusion length of the total smothing filter for the off-line discrete analysis will be:

$$\sigma_{off}^2 = \sigma_{firn}^2 + \sigma_{5cm}^2 \tag{3.12}$$

where σ_{5cm}^2 is the diffusion length of the smoothing imposed by the sample cutting sceme on a 5 cm resolution. If one averages the on-line CFA data on a 5 cm resolution by means of a running mean filter, the diffusion length of the total smoothing filter for the on-line CFA measurements averaged on a 5 cm resolution will be:

$$\sigma_{on}^2 = \sigma_{firn}^2 + \sigma_{5cm}^2 + \sigma_{cfa}^2 \tag{3.13}$$

From equations (3.12) and (3.13) we get:

$$\sigma_{cfa}^2 = \sigma_{on}^2 - \sigma_{off}^2 \tag{3.14}$$

As a result, the term $\sigma_{on}^2 - \sigma_{off}^2$ is directly related to the diffusion length of the smoothing filter of the whole CFA-water isotope system including the melting and debubbling sections. Based on equation (3.11), the power spectral density of the signals will be:

$$P = P_0 e^{-k^2\sigma^2} \tag{3.15}$$

where σ^2 refers in this case to σ_{on}^2 or σ_{off}^2. Combining the power spectral densities of the on-line and off-line time series we finally get:

$$\ln\left(\frac{P_{off}}{P_{on}}\right) = \ln\left(\frac{P_{0off}}{P_{0on}}\right) + \sigma_{cfa}^2 k^2 \tag{3.16}$$

Hence, the logarithm of the ratio P_{off}/P_{on} is linearly related to k^2 with a slope equal to σ_{cfa}^2. In Figure 3.7 we perform this analysis for δD and by applying a linear fit we calculate the $\sigma_{cfa}[D]$ to be equal to 16.4 ± 2.4 mm. In a similar manner $\sigma_{cfa}[O18]$ is found to be equal to 16.8 ± 2.3 mm.

The higher value calculated with the spectral method points to the additional diffusion of the sample at the melter and debubbler system that could not be considered in the analysis based on the step response. The impulse response of the system based on the updated value of σ_{cfa}^2 is presented in Figure 3.6.

3.3.5 Optimal Filtering

In the ideal case of a noise-free measured signal ${\delta_m}'(z)$ and provided that the transfer function $\hat{\mathcal{G}}_{cfa}$ is known, one can reconstruct the initial isotopic signal

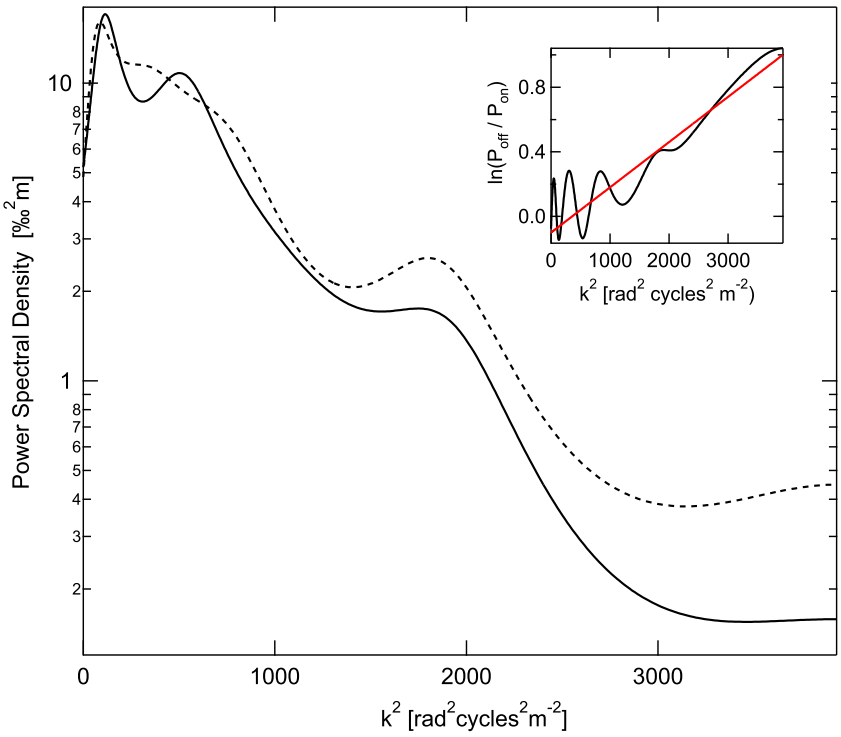

Figure 3.7: Calculation of the diffusion length for the transfer function of the CFA system. The dashed and solid lines represend respectively the power spectral density of the offline discrete data and the CFA data averaged on a 5 cm resolution.

$\delta_i(z)$ from equation 3.3 as:

$$\delta_i(z) = \frac{1}{2\pi}\int_{-\infty}^{\infty} \frac{\hat{\delta_m}'(\omega)}{\hat{\mathcal{G}}(\omega)} e^{-i\omega z} d\omega \tag{3.17}$$

where the integral operation denotes the inverse Fourier transform and $\omega = \frac{2\pi}{\lambda}$ with λ being the wavelength of the isotopic signals. In the presence of measurement noise $\eta(z)$, this approach will fail due to excess amplification of the high frequency noise channels in the spectrum of the signal.

Hereby we use the Wiener approach in deconvoluting the acquired isotopic signals for the diffusion that takes place during the measurement. Considering a measured isotopic signal

$$\delta_m(z) = \delta_m{}'(z) + \eta(z) \tag{3.18}$$

an optimal filter $\varphi(z)$ can be constructed that when used at the deconvolution step, it results in an estimate of the initial isotopic signal described as:

$$\tilde{\delta}_i(z) = \frac{1}{2\pi}\int_{-\infty}^{\infty} \frac{\hat{\delta}_m(\omega)}{\hat{\mathcal{G}}(\omega)} \hat{\varphi}(\omega) e^{-i\omega z} d\omega \tag{3.19}$$

Assuming that $\delta_m{}'(z)$ and $\eta(z)$ are uncorellated signals, the optimal filter is given by:

$$\hat{\varphi}(\omega) = \frac{|\hat{\delta}'_m(\omega)|^2}{|\hat{\delta}'_m(\omega)|^2 + |\hat{\eta}(\omega)|^2} \tag{3.20}$$

(Wiener, 1949) ; where $|\hat{\delta}'_m(\omega)|^2$ and $|\hat{\eta}(\omega)|^2$ are the power spectral densities of the signals $\delta'_m(\omega)$ and $\eta(\omega)$.

In the same fashion as in the previous section we assume that the spectrum of the noise free measured signal $|\hat{\delta}'_m(\omega)|^2$, is described by equation (3.15) where $\sigma^2 = \sigma^2_{tot}$. Regarding the noise, we assume red noise described by an AR1 process. The spectrum of the noise signal will then be described by (Kay and Marple, 1981) :

$$|\hat{\eta}(\omega)|^2 = \frac{\sigma^2_\eta \Delta z}{|1 + a_1 \exp(-2\pi i f \Delta z)|^2} \tag{3.21}$$

where σ^2_η is the variance of the noise and a_1 is the coefficient of the AR1 process. We vary the parameters σ^2_{tot}, P_0, σ^2_η and a_1 so that the sum $|\hat{\delta}_m(\omega)|^2 = |\hat{\delta}'_m(\omega)|^2 + |\hat{\eta}(\omega)|^2$ fits the spectrum of the measured signal. The set of parameters that results in the optimum fit is used to calculate the optimal filter.

The constructed filters together with the transfer functions that were calculated based on the two different techniques outlined in section 3.3.4 are illustrated in Figure 3.8. One can observe how the restoration filters work by amplifying cycles with wavelengths as low as 7 mm. Beyond that point, the shape of the optimal filter attenuates cycles with higher frequency, which lie in the area of noise. An example of deconvoluted δD data section is given in Figure 3.9. It can be seen that the effect of the optimal filtering results in both the amplification of the signals that are damped due to the instrumental diffusion, as well as in the filtering of the measurement noise.

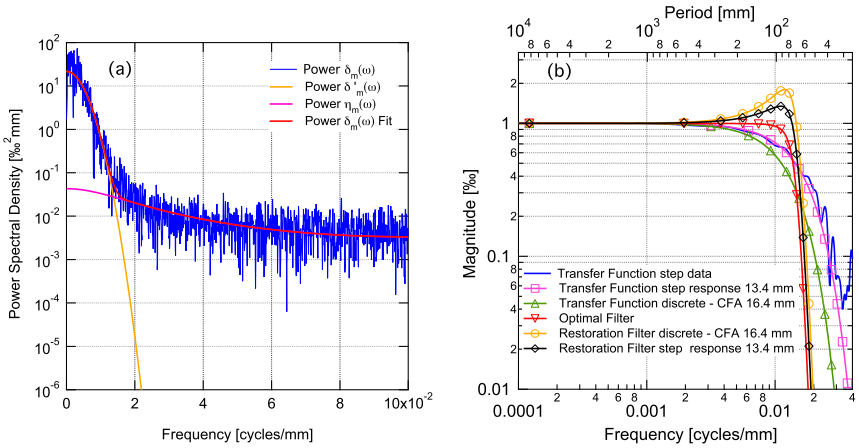

Figure 3.8: (a) Power Spectral Density of δD . (b) Transfer function calculated based on the step response with $\sigma_{cfa} = 13.4$ mm (pink - squares) and the comparison between discrete and CFA analysis with $\sigma_{cfa} = 16.4$ mm (green - triangles). Restoration filters built considering the two different transfer functions are illustrated with orange circes ($\sigma_{cfa} = 16.4$ mm) and black diamonds ($\sigma_{cfa} = 13.4$ mm).

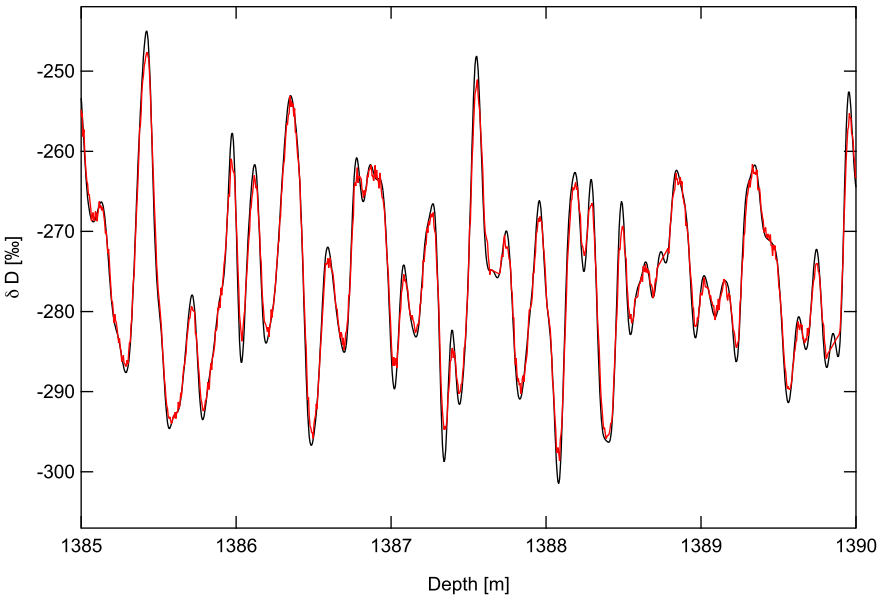

Figure 3.9: δD signal before and after optimal filtering

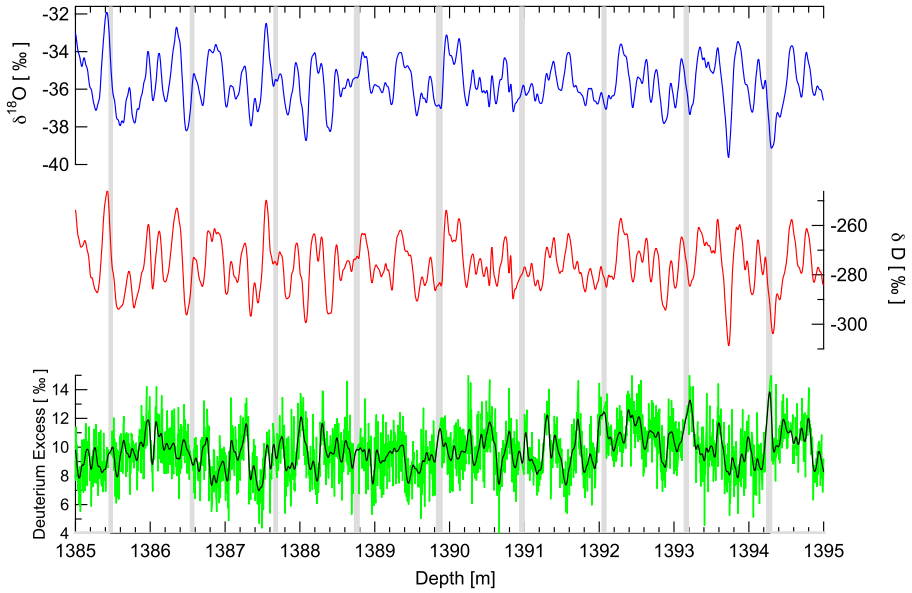

Figure 3.10: δ^{18}O , δD and D_{xs} signals after the optimal filtering. For the D_{xs} we present the signal before (light green) and after (black) the filtering; Gray bars indicate the position and width of sections with missing/removed data.

3.3.6 Information on Deuterium excess

Combining δ^{18}O and δD gives the deuterium excess as $D_{xs} = \delta D - 8\delta^{18}O$ (Craig et al., 1963; Mook, 2000). The noise level of the D_{xs} signal can be calculated by the estimated noise levels of δ^{18}O and δD as:

$$\sigma_{D_{xs}} = \sqrt{\sigma_D^2 + 64 \cdot \sigma_{18}^2} = 0.48‰ \tag{3.22}$$

As seen in Figure 3.10, the D_{xs} signal presents a low signal to noise ratio. In this case, the technique of optimal filtering can effectively attenuate unwanted high frequency noise components, thus reveiling a "clean" D_{xs} signal.

The latter offers the possibility for the study of abrubt transitions as they have previously been investigated in δ^{18}O , δD and D_{xs} time series from discrete high resolution samples. (Steffensen et al., 2008) . The on-line fashion in which these measurements are performed has the potential to yield not only higher temporal resolution but also better statistics for those climatic transitions.

3.4 Summary and Conclusions

We have succesfully demonstrated the possibility for on-line water isotopic analysis on a continuously melted ice core sample. We used an infra red laser spectrometer in a cavity ring down configuration in combination with a continuous flow melter system. A custom made continuous stream flash evaporator served as the sample preparation unit, interfacing the laser spectrometer to the melter system.

Local water standards have been used in order to calibrate the measurements to the VSMOW scale. Additionally, dependencies related to the sample size in the optical cavity have been accounted for. The melting procedure is recorded by an optical encoder that provides the necessary information for assigning a depth scale to the isotope measurements. We verified the validity of the applied calibrations and the calculated depth scale by comparing the CFA measurements with measurements performed on discrete samples in 5 cm resolution.

By means of spectral methods we provide an estimate of the noise level of the measurements. The combined uncertainty of the measurement is estimated at $\approx$ 0.06, 0.2, and 0.5 ‰ for δ^{18}O , δD and D_{xs} respectively. This performance is comparable to, or better than the performance typically achieved with conventioanl IRMS systems in a discrete mode.

Based on the isotopic step at the beginning of each CFA run, the impulse response, as well as the transfer function of the system can be estimated. We show how this method does not take into account the whole CFA system, thus underestimating the sample diffusion that takes the place from the melter until the optical cavity of the spectrometer. We proposed a different method that considers the power spectrum of the CFA data in combination with the spectrum of a data set over the same depth interval measured in a discrete off-line fashion. With the use of the optimal filtering deconvolution technique, provides a way to deconvolute the measured isotopic profiles.

The combination of infra red spectroscopy on gaseuous samples with continuous flow melter systems provides new possibilities for ice core science. The non destructive, continuous and on-line technique, offers the possibility for analysis of multiple species on the same sample, in high resolution and precision and pottentially performed in the field.

Chapter 4

Diffusion of water isotopologues in polar firn and ice

Abstract

Water isotope ratios as measured from ice core samples have been used as a proxy for past temperatures. Based on a Rayleigh fractionation process they record the cloud temperature during snow formation. However, changes in the temperature and humidity of the vapour source can also affect the isotopic signal of the polar precipitation, thus inducing isotopic artifacts. This has been the case for the temperature reconstruction based on the isotopic profiles of the GRIP core. A constant isotope sensitivity underestimates the temperature difference between glacial and interglacial periods. Based on gas fractionation and borehole inversion studies it has been shown that the isotopic slope varies during the glacial times. For the case of the Antarctic cores gas fractionation studies show a discrepancy between models and data. One of the possible scenarios responsible for this is that the temperature history used for driving the gas fractionation models is not accurate. Here we present a possible alternative temperature reconstruction method based on the study of the water isotope diffusion in firn. This diffusive process occurs in the pore space of the firn pack, mixing water vapor from different layers and smoothing the isotopic profiles. It is temperature dependent and it presents a slightly different rate between the two isotopic species of water $^{1}H_{2}\,^{18}O$ and $^{1}H\,^{2}H\,^{16}O$. Here we describe the mechanisms that control the diffusion process and derive expressions for the diffusivity and the diffusion length. We also decribe the process of self ice diffusion that takes place within the ice lattice. This process is signifficant towards the bottom of the core where the temperature of the ice becomes higher, eventually reaching the pressure metling point. We generate different temperature histories for the Dome C site by using different values of the isotope slope and with these we drive a model for the estimation of the diffusion length. Using spectral estimation techniques it is possible to estimate the value of the diffusion length based on high resolution data. We apply this estimation procedure on water

isotope data sets of two different resolutions (11 cm and 2.5 cm) and compare with the outcome of the model. The deffusion length results indicate that the value of the isotope slope varies during the last 90 kyr. Based on the values we calculate for the isotope slope we infer a temperature history scenario that shows a glacial – interglacial step of approximately 9°K but temperatures that are warmer compared to what is currently believed for Marine Isotope Stages 3 and 4. We conclude that the outcome of this study is not solid but propose further tests and samples analysis in order to refine the temperature reconstruction for Dome C.

4.1 Introduction

Ratios of water's stable isotopologues have been extensively used in the field of ice cores. Water isotope profiles of ice cores are typically used for the reconstruction of the past temperatures (Dansgaard et al., 1982; Johnsen et al., 2001; Jouzel et al., 2007) and accumulation rates (Schwander et al., 2001). Subsequently, models for dating, borehole temperature, as well as gas/ice age differences, make use of the temperature histories inferred by those profiles (Schwander et al., 1997; Dahl Jensen and Johnsen, 1986; Cuffey et al., 1992). It is thus understandable that the validity of the isotopic signal for past temperature and accumulation reconstructions plays a key role in a wide range of ice core data and modelling applications.

4.1.1 The spatial isotope slope

Previous studies (Johnsen et al., 1989; Lorius et al., 1969) have reported a linear relationship between the isotopic signal of polar precipitation and the local temperature. For Greenland sites and present conditions, Johnsen et al. (2001) used a linear relationship between the mean annual surface temperature and the mean annual isotopic value of snow described as:

$$\delta^{18}\mathrm{O} = 0.67 \cdot T(^{\circ}\mathrm{C}) - 13.7\ ‰. \tag{4.1}$$

Assuming that this relatioship (hereafter "spatial slope") holds for different climatic regimes (glacial conditions and inter-stadial events) one can reconstruct the temperature history of an ice core site based on the measured δ^{18}O profile. In figure 4.1 we present such a reconstruction based on the δ^{18}O profile from NGRIP corrected for the mean ocean water changes as reported by Waelbroeck et al. (2002). The main climatic features observed in this plot, consist of the glacial - interglacial transition and a number of rapid warming inter-stadial events during the glacial period, commonly referred to as Dansgaard - Oeschger events. Based on the reconstruction of figure 4.1, one can infer the magnitude of these temperature shifts.

4.1.2 On the validity of the spatial slope

The validity of the temperature reconstruction based on the spatial isotope slope was questioned when studies based on borehole temperature inversion (Dahl Jensen et al., 1998; Cuffey et al., 1994) and thermal fractionation of the $^{15}\mathrm{N}/^{14}\mathrm{N}$ and $^{40}\mathrm{Ar}/^{36}\mathrm{Ar}$ pairs (Severinghaus et al., 1998; Severinghaus and

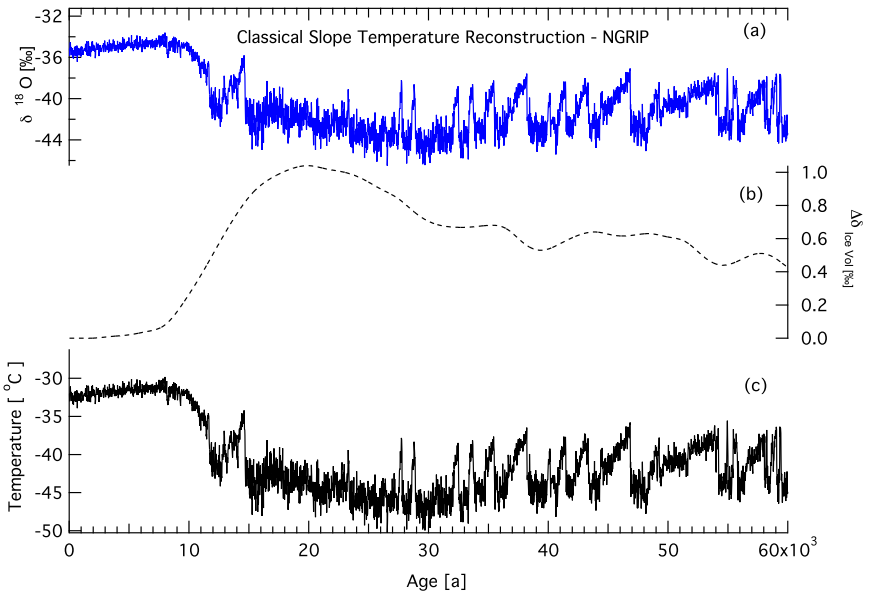

Figure 4.1: NGRIP isotopic record (a)converted to a temperature history (c) using the spatial slope after correcting for Mean Ocean Water changes in δ^{18}O (b)

Brook, 1999; Lang et al., 1999; Schwander et al., 1997; Landais et al., 2004) were developed and applied. The fore mentioned studies drew the following basic conclusions regarding the isotopic thermometer. First, the isotopic slope is not constant with time. Second, during glacial conditions the spatial slope presents an isotopic sensitivity higher than the sensitivity reconstructed by the borehole inversion and gas isotopic studies. As a result, in order to reconstruct past temperatures based on the water isotope signal, one should assess the sensitivity of the δ^{18}O to temperature for different climatic regimes, thus inferring the "temporal slope" α_t.

Based on the borehole inversion method Dahl Jensen et al. (1998) estimated that the temperature of the GRIP site 25 kaBP was more than 20°C colder than present, deducing a value of $\alpha_t \approx 0.5$. The borehole inversion technique can assess long term temperature features. However rapid climatic events cannot be considered with this method. To that end, gas isotope studies have been utilized to study the magnitude of the Younger Dryas and the Bølling – Allerød climatic transitions as well as several interstadial events. Based on δ^{15}N and δ^{40}Ar measurements, of GISP2 samples, Severinghaus et al. (1998) calculated the temperature of the Younger Dryas stadial to be ≈ 46°C, a result that points to a value for α_t equal to approximately 0.35. In a similar way the temperature shift over the Bølling transition was estimated to be 9 ± 3°C. Considering the δ^{18}O shift to be 3.4‰, in the GISP2 record, Severinghaus and Brook (1999) conclude that the value of α_t is 0.38 ‰K^{-1} for this climatic period. Applied for interstadial 19, the δ^{15}N thermal fractionation method yields a temperature variation of 16°C equivalent to a slope $\alpha_t \approx 0.42$ ‰K^{-1} (Lang et al., 1999). This

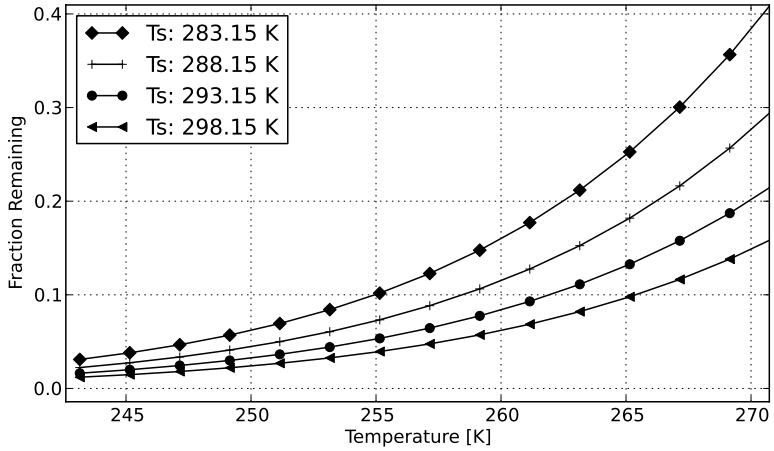

Figure 4.2: Rayleigh scheme with varying source temperature - fraction removed for a combination of source and site temperatures

result is consistent with the observations of Schwander et al. (1997). Based on the match between the measured CH_4 and $\delta^{18}O$ the calculated Δage infers a temperature history that is compatible with a slope value $\alpha_t < 0.5$ for the end of the glacial.

The picture we describe above indicates that one should be cautious when using the $\delta^{18}O$ signal for past temperature reconstructions. The spatial slope as described in eq. 4.1, seems to underestimate temperature variations for certain climatic periods by almost a factor of 2 . The physical mechanisms that are responsible for this occurrence are yet not well understood. However certain assumptions can be made. The isotopic signal is mainly controlled by the amount of depletion a water vapor mass undergoes after a sequence of precipitation events. This cumulative effect results in progressively isotopically lighter snow and it depends on the difference of the temperature at the source site and the precipitation site. Here we illustrate this effect by using a simple Rayleigh transport–fractionation model. We make the assumption that the relative change in the amount of vapour in the air parcel is equal to the relative change of the vapour pressure. We illustrate this in figure 4.2. The effect of the varying source temperature results in different amounts of depletion and thus fractionation. A more detailed description of the model is given in the Appendix A.

Changes in the atmospheric or/and ocean circulation are likely to shift the position of the water vapour source especially at times of rapid climatic transitions. Steffensen et al. (2008) have reported abrupt changes in the D_{xs} signal preceding the Bølling transition and the Younger Dryas termination as recorded in the $\delta^{18}O$ and δD record of the NGRIP core. In combination with the signal of the Ca^{2+} concentrations in the ice, the authors indicate a redistribution of the atmospheric and oceanic circulation. Such a condition has vey likely caused a redistribution of the sources of water vapor of the polar precipitation. It is thus reasonable to assume that during these non steady state conditions the

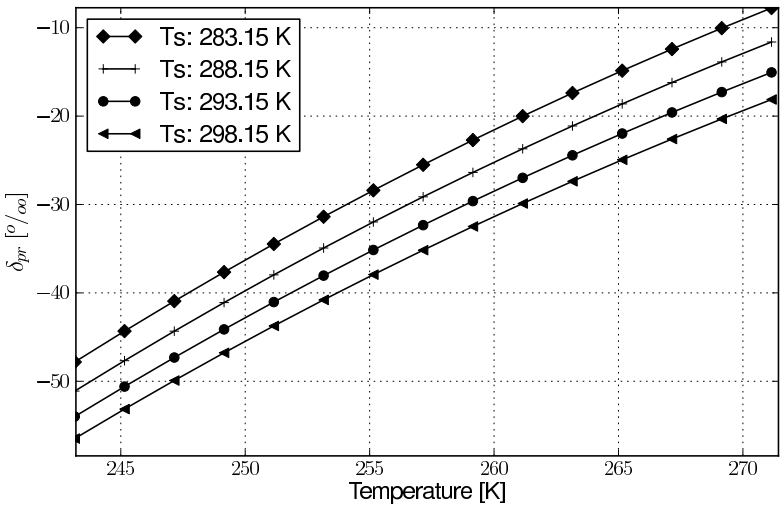

Figure 4.3: Rayleigh scheme with varying source temperature - δ^{18}O of precipitation for a combination of source and site temperatures

sensitivity of the isotopic signal is changed. In fact the rapidity of such climatic transitions had been reported earlier by Johnsen et al. (1989). Detailed sampling of the Dye-3 core combined with high presicion δD and δ^{18}O analysis reveals rapid changes in the D_{xs} signal accompanied by subsequent anticorralated changes in δD and δ^{18}O . Additionally, the wariming phase of these events apears to be more rapid than the cooling phase.

Combined use of the δ^{18}O and D_{xs} measured signals and Rayleigh type models, has been utilized (Cuffey and Vimeux, 2001; Kavanaugh and Cuffey, 2002; Masson-Delmotte et al., 2005)to resolve the issues related to the possible shift of the evaporation source. Assuming that for a sampling site there exists a function

$$\delta_s^i = \delta_s^i \left(T_s, T_o, \delta_o^i \right) \tag{4.2}$$

that maps the isotopic composition δ_s^i of the precipitate at the sampling site ($i = 2$ or 18) to the temperature of the site and the vapor source T_s, T_o as well as to the isotopic composition of the mean ocean water δ_o^i. A first order perturbation can be applied, provided that changes in T_s, T_o and δ_o^i are small. That results in:

$$d\delta_s^i = \gamma_1 dT_s + \gamma_2 dTo + \gamma_3 d\delta_o^i \tag{4.3}$$

Similarly for the D_{xs} signal:

$$d\mathrm{D}_{xs} = \beta_1 dT_s + \beta_2 dTo + \beta_3 d\delta_o^i \tag{4.4}$$

Determination of the parameters $\gamma_{1,2,3}$ and $\beta_{1,2,3}$ can yield the temperature histories T_s and T_o.

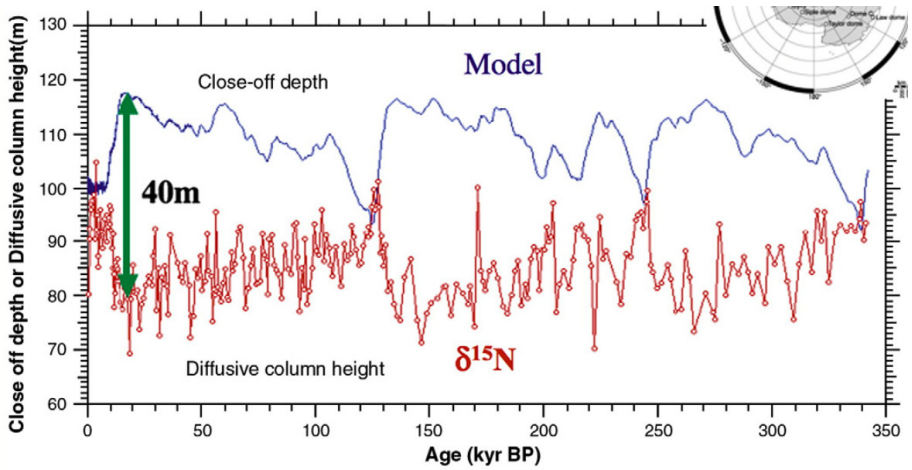

Figure 4.4: Modelled and measured diffusive column length for the Dome Fuji core. Figure from Kawamura (2000).

4.1.3 The case of Antarctica. An apparent mismatch between models and data

The D_{xs} correction approach described in the previous section has been used to infer past temperatures at sites of low accmulation on the east Antarctic plateau (Jouzel et al., 2007; Cuffey and Vimeux, 2001). However, validation of the results for this area is difficult. Due to the low accumulation borehole profiles do not reveal a profound glacial signal. As a result, inversion of the temperature profile does not deliver robust solutions for the temperature history of the site.

Measurements of δ^{40}Ar and δ^{15}N performed on samples from Antarctic sites as Vostok, Dome C and EDML can possibly provide an insight on past conditions of densification and thus temperature and accumulation. Apparently, there seems to be a discrepancy between the δ^{40}Ar and δ^{15}N measured profiles and the profiles predicted from densification and gas thermal fractionation models. This discrepancy has been reported in a variety of published works (Kawamura, 2000; Caillon et al., 2003; Landais et al., 2006; Severinghaus et al., 2010). It applies for a variety of sites and mainly low accumulation, non coastal sites.

Based on a temperature and an accumulation history, densification models predict that across the glacial termination the length of the diffusive column in the firn shows a clear decrease. This is due to the combined increase in temperature and accumulation. It has to be noted that in most modelling exercises the accumulation is based on the δ^{18}O and thus shows a strong correlation with temperature. We present here two of those exercises as reported by Kawamura (2000) and Dreyfus et al. (2010) in figures 4.4 and 4.5. These studies refer to Dome Fuji and Epica Dome C respectively. The discrepancy between data and model is clear across the glacial terminations.

Mechanisms responsible for this discrepancy have been proposed. Landais et al. (2006) outline the possible scenarios, which briefly are:

1. The thickness of the convective and non diffusive zones is different in glacial and interglacial conditions. A possible redistribution of the firn

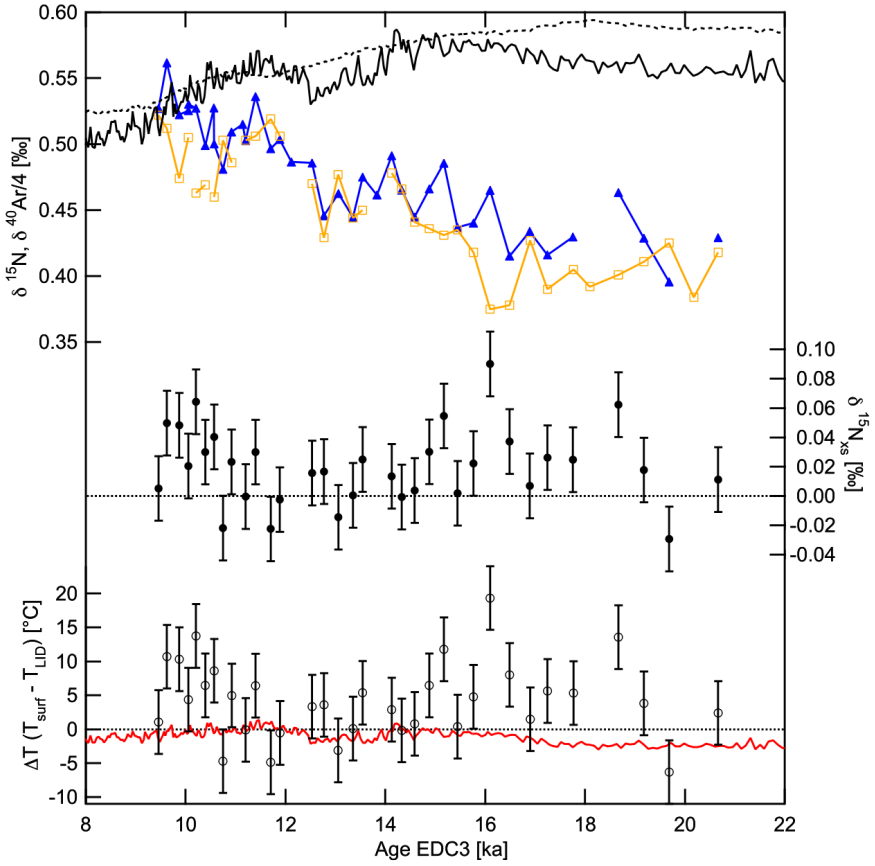

Figure 4.5: Modelled (black line) and measured (blue triangles) δ^{15}N profile for Epica Dome C. Figure from Dreyfus et al. (2010)

structure can possibly alter the thickness of the diffusive zone without affecting the total thickness of the firn column. As a result the δ^{15}N signal cannot be used to reconstruct past densification conditions unless the structure of the firn column is reassessed. However for sites like Dome C and Vostok the necessary thickness of the convective zone during glacial conditions would need to be $\approx$ 40m. (Caillon et al., 2003; Landais et al., 2006)

2. The densification mechanisms as described by the existing models do not perform adequately for glacial conditions

3. Due to the reduced accumulation expected for glacial conditions, the advection of heat from the surface to the bottom of the firn column decreases. Consequently, the temperature gradient apparent in firn is altered, possibly changing the balance between gravitational and thermal fractionation. This would eventually cause changes in th δ^{15}N signal accordingly (Caillon et al., 2003; Goujon et al., 2003).

4. The accumulation and temperature histories that are used to drive the δ^{15}N models can possibly be inaccurate for some sections of the ice core.

It is the opinion of the author that based on the available literature, scenarios 1 - 3 have been considered and tested. However scenario 4 has neither been considered as a possibility nor tested by use of borehole temperature or gas fractionation models using a modified tamperature and accumulation history inputs. The idea that the structure of the firn column is redistributed during glacial terminations seems to be somewhat supported by modern day data from Antarctic sites with extremely low accumulation rates and deep convective zones of the order of 30-40 m (Severinghaus et al., 2010). However, similar discrepancies in δ^{15}N have been observed in sites with relatively higher accumulation. EDML is one of those examples as illustrated in figure 4.6. Based on the preceding arguments one can argue that might be useful to look into the possibility of a wrong temperature and accumulation history for those sites, as an additional mechanism that contributes to the model-data discrepancy observed. To that end one could also propose alternative paleothermometry tools.

4.2 Molecular diffusion of water isotopes in firn and ice

We hereby investigate the possibility of estimating past temperatures via the assessment of the diffusion rates of the water isotopologues in firn and ice. We use an ensemble of data collected from different ice core sites. The data used here are collected in a discrete fashion and measured with conventional mass spectrometry. We would like to point out that the work presented in chapters 2 and 3 on the online water isotope measurements was motivated by the theory of diffusion and the possibility to use the online high resolution data in order to infer past temperatures based on the firn isotope diffusion studies.

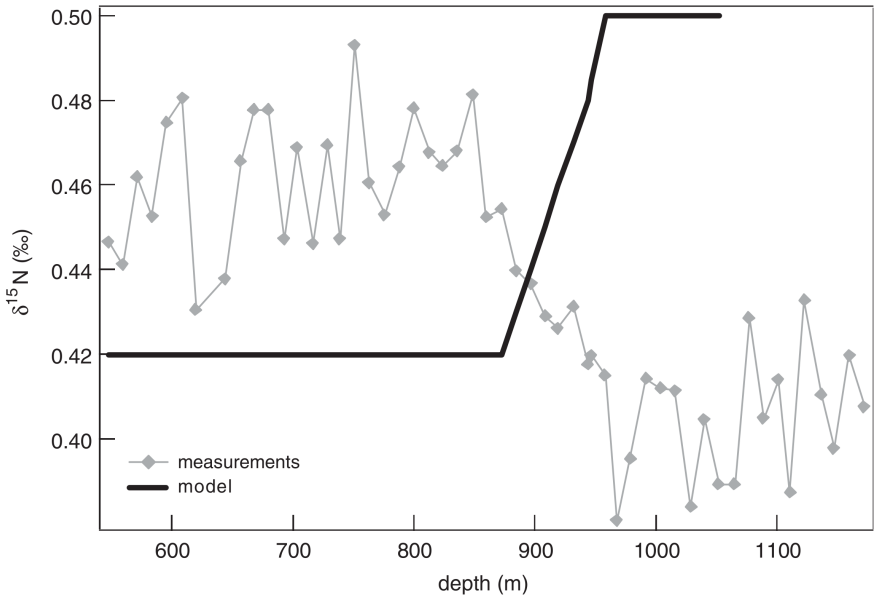

Figure 4.6: Steady state model (Arnaud et al., 2000) and measurements of δ^{15}N for the EDML site. Figure from Landais et al. (2006)

4.2.1 Diffusion in firn - the diffusion length and a simple numerical approach

We will outline here the theory of water isotope diffusion in firn and ice. Almost exclusively, the formulations used here are based on the work presented in Johnsen (1977) and Johnsen et al. (2000) and the experimental works of Jean-Baptiste et al. (1998) and Van der Wel et al. (2011).

The diffusion of water isotopes in firn is a process that occurs after the deposition of the precipitation. It is a molecular exchange process taking place in the vapor phase and it is driven by isotopic gradients apparent along the firn stack. As the densification of firn continues the diffusion process slows down until it ceases at pore close off. Assuming a coordinate system fixed on a sinking layer of firn, Fick's second law accounting for layer thinning describes the process mathematically as:

$$\frac{\partial \delta}{\partial t} = D\left(t\right) \frac{\partial^2 \delta}{\partial z^2} - \dot{\varepsilon}_z\left(t\right) z \, \frac{\partial \delta}{\partial z} \tag{4.5}$$

Where $D\left(t\right)$ is the diffusivity coefficient and $\dot{\varepsilon}_z\left(t\right)$ a uniform vertical strain rate. Use of Fourier integrals yields the solution to equation 4.5 as the convolution of the initial isotopic signal $\delta\left(z,0\right)$ with a Gaussian filter:

$$\mathcal{G} = \frac{1}{\sigma\sqrt{2\pi}} \cdot e^{\frac{-z^2}{2\sigma^2}} \tag{4.6}$$

The isotopic signal at time $\delta\left(z,t\right)$ will then be given by:

$$\delta\left(z',t\right)=\mathcal{S}\left(t\right)\frac{1}{\sigma\sqrt{2\pi}}\int_{-\infty}^{+\infty}\delta\left(z,0\right)\exp\left\{\frac{-\left(z-u\right)^{2}}{2\sigma^{2}}\right\}\mathrm{d}u \tag{4.7}$$

Where $\mathcal{S}\left(t\right)$ the total thinning the layer has experienced during the time interval $t=0\rightarrow t=\tau$ due to compression and equal to:

$$\mathcal{S}\left(t\right)=e^{\int_{0}^{\tau}\dot{\varepsilon}_{z}(t)\mathrm{d}t} \tag{4.8}$$

The standard deviation term σ of the Gaussian filter represents the mean displacement of a water molecule in the z-axis. Johnsen (1977) proposes equation 4.9 for the calculation of the diffusion length.

$$\frac{\mathrm{d}\sigma^{2}}{\mathrm{d}t}-2\,\dot{\varepsilon}_{z}(t)\,\sigma^{2}=2D(t) \tag{4.9}$$

For the case of firn we will assume a simple strain rate as:

$$\dot{\varepsilon}_{z}\left(t\right)=\frac{-\partial\rho}{\partial t}\,\frac{1}{\rho} \tag{4.10}$$

This yields to an expression for the diffusion length as described in equation 4.11. The latter can be integrated numerically when a density profile and its adjoint age is known. We can also see that an expression for the diffusivity D(t) is necessary.

$$\sigma^{2}(t)=\frac{1}{\rho^{2}(t)}\int_{0}^{t}2\,D(\tau)\,\rho^{2}(\tau)\,\mathrm{d}\tau \tag{4.11}$$

In a slightly different approach, equation 4.9 can be expressed with the density ρ as the independent variable. Use of the integrating factor $F\left(\rho\right)=e^{\int\frac{2}{\rho}\,\mathrm{d}\rho}$ yields.

$$\sigma^{2}\left(\rho\right)=\frac{1}{\rho^{2}}\int_{\rho_{o}}^{\rho}2\rho^{2}\left(\frac{\mathrm{d}\rho}{\mathrm{d}t}\right)^{-1}D(\rho)\;\mathrm{d}\rho \tag{4.12}$$

In the following sections we will introduce such a function by using an empirical steady state model of densification by Herron and Langway (1980). First we outline the parametrization for the diffusivity $D(t)$ as presented in Johnsen et al. (2000).

4.2.2 The diffusivity

We express the diffusivity as a function of firn density ρ and we use:

$$D_{fi}(\rho)=\frac{m\,p\,D_{ai}}{R\,T\,\alpha_{i}\,\tau}\left(\frac{1}{\rho}-\frac{1}{\rho_{ice}}\right) \tag{4.13}$$

The terms used in equation 4.13 and the parametrization used for them are described below:

- m: molar weight (kg)

- p: saturation vapor pressure over ice (Pa). We use (Murphy and Koop, 2005):

$$p = \exp\left(9.5504 - \frac{5723.265}{T} + 3.530\,\ln(T) - 0.0073\,T\right) \tag{4.14}$$

- D_a: diffusivity of water vapor in air ($m^2 sec^{-1}$). We use (Hall and Pruppacher, 1976):

$$2.1 \cdot 10^{-5}\left(\frac{T}{T_o}\right)^{1.94}\left(\frac{P_o}{P}\right) \tag{4.15}$$

  with $P_o = 1$ Atm, $T_o = 273.15$ K and P, T the ambient pressure (Atm) and temperature (K). Additionally from Merlivat and Jouzel (1979) $D_{a^2\mathrm{H}} = \frac{D_a}{1.0285}$ and $D_{a^{18}\mathrm{O}} = \frac{D_a}{1.0251}$

- R: molar gas constant $R = 8.314478$ $(m^3 PaK^{-1}mol^{-1})$

- T: Ambient temperature (K)

- α_i: Ice – Vapor fractionation factor. we use the formulations by Majoube (1971) and Melivat and Nief (1967) for $\alpha^2_{s/v}$ and $\alpha^{18}_{s/v}$ respectively.

$$\ln \alpha_{Ice/Vapor}\left({}^2\mathrm{H}/{}^1\mathrm{H}\right) = 16288/T^2 - 9.34 \times 10^{-2} \tag{4.16}$$

$$\ln \alpha_{Ice/Vapor}\left({}^{18}\mathrm{O}/{}^{16}\mathrm{O}\right) = 11.839/T - 28.224 \times 10^{-3} \tag{4.17}$$

- τ: The firn tortuosity. We use (Schwander et al., 1988):

$$\frac{1}{\tau} = 1 - b \cdot \left(\frac{\rho}{\rho_{ice}}\right)^2 \quad \rho \leq \frac{\rho_{ice}}{\sqrt{b}},\ b = 1.3 \tag{4.18}$$

  Based on equation 4.18, $\tau \to \infty$ for $\rho > 804.3\,kgrm^{-3}$

4.2.3 Parametrization of the densification rates with a semi empirical model

We will use the semi–empirical densification model by Herron and Langway (1980), in order to produce analytical expressions for the diffusion length as indicated in equation 4.12. According to this model the densification process is divided in two stages. The densification rates are then described as:

$$\frac{\mathrm{d}\rho}{\mathrm{d}t} = k_o A^{\alpha}\left(\rho_{ice} - \rho\right) \qquad \rho < 550\ kgr\,m^{-3} \tag{4.19}$$

$$\frac{\mathrm{d}\rho}{\mathrm{d}t} = k_1 A^{b}\left(\rho_{ice} - \rho\right) \qquad 550\ kgr\,m^{-3} < \rho < 800\ kgr\,m^{-3} \tag{4.20}$$

Where:

$$k_o = 0.011 \exp\left\{-\frac{10160}{RT}\right\} \tag{4.21}$$

$$k_1 = 0.575 \exp\left\{\frac{21400}{RT}\right\} \tag{4.22}$$

and $\alpha = 1.1$ and $b = 0.5$. So now we can write:

$$D(\rho) = \overbrace{\frac{mpD_{ai}}{RT\alpha_i}}^{\mathrm{Z}} \left(1 - \frac{1.3\rho^2}{\rho_{ice}^2}\right)\left(\frac{1}{\rho} - \frac{1}{\rho_{ice}}\right) \tag{4.23}$$

and thus for densities lower than $\rho_c = 550\, kgr\, m^{-3}$

$$\sigma^2(\rho) = \frac{1}{\rho^2} Z \int 2\varrho^2 \frac{1}{k_o A^\alpha (\rho_{ice} - \varrho)} \left(1 - \frac{1.3\varrho^2}{\rho_{ice}^2}\right)\left(\frac{1}{\varrho} - \frac{1}{\rho_{ice}}\right) \mathrm{d}\varrho \tag{4.24}$$

that yields:

$$\sigma^2(\rho) = \frac{Z}{\rho^2 k_o A^\alpha \rho_{ice}} \left(\rho^2 - \frac{1.3\rho^4}{2\rho_{ice}^2} + C_1\right) \tag{4.25}$$

using the initial conditions $\rho = \rho_o$ (surface density) $\rightarrow \sigma^2 = 0$ we get:

$$C_1 = \frac{1.3\rho_o^4}{2\rho_{ice}^2} - \rho_o^2 \tag{4.26}$$

$$\sigma^2(\rho < \rho_c) = \frac{Z}{\rho^2 k_o A^\alpha \rho_{ice}} \left[\rho^2 - \rho_o^2 - \frac{1.3}{2\rho_{ice}^2}\left(\rho^4 - \rho_o^4\right)\right] \tag{4.27}$$

For densities higher than the critical $\rho_c = 550\, kgr\, m^{-3}$.

$$\sigma^2(\rho) = \frac{Z}{\rho^2 k_1 A^b \rho_{ice}} \left(\rho^2 - \frac{1.3\rho^4}{2\rho_{ice}^2} + C_2\right) \tag{4.28}$$

for the integration constant C_2 we use the result of 4.27 for $\sigma(\rho = \rho_c)$:

$$\sigma^2(\rho = \rho_c) = \frac{Z}{\rho_c^2 k_o A^\alpha \rho_{ice}} \left[\rho_c^2 - \rho_o^2 - \frac{1.3}{2\rho_{ice}^2}\left(\rho_c^4 - \rho_o^4\right)\right] \tag{4.29}$$

we require:

$$\underbrace{\frac{\overbrace{Z}^{Z_1}}{\rho_c^2 k_1 A^b \rho_{ice}} \left(\rho_c^2 - \frac{1.3\rho^4}{2\rho_{ice}^2} + C_2\right) = \frac{Z}{\rho_c^2 k_o A^\alpha \rho_{ice}} \left[\rho_c^2 - \rho_o^2 - \frac{1.3}{2\rho_{ice}^2}\left(\rho_c^4 - \rho_o^4\right)\right]}_{\mathcal{H}} \tag{4.30}$$

So then we conclude for C_2:

$$C_2 = \frac{\mathcal{H}}{Z_1} - \left(\rho_c^2 + \frac{1.3\rho_c^2}{2\rho_{ice}^2}\right) \tag{4.31}$$

$$\sigma^2\left(\rho > \rho_c\right) = Z_1\left(\rho^2 - \frac{1.3\rho^4}{2\rho_{ice}^2} + \frac{\mathcal{H}}{Z_1} - \rho_c^2 + \frac{1.3\rho_c^4}{2\rho_{ice}^2}\right) \tag{4.32}$$

Rearrangement and substitution of $\mathcal{H}$ and Z_1 finally yields:

$$\begin{aligned}\sigma^2\left(\rho > \rho_c\right) = &\frac{Z}{\rho^2 k_1 A^b \rho_{ice}}\left[\rho^2 - \rho_c^2 - \frac{1.3}{2\rho_{ice}^2}\left(\rho^4 - \rho_c^4\right)\right] + \\ &\frac{Z}{\rho^2 k_o A^\alpha \rho_{ice}}\left[\rho_c^2 - \rho_o^2 - \frac{1.3}{2\rho_{ice}^2}\left(\rho_c^2 - \rho_o^2\right)\right]\end{aligned} \tag{4.33}$$

4.3 Calculations on different sites and scenarios

4.3.1 Densification

Here we present implementations of the Herron and Langway model for two sites, Dome C and NGRIP. Dome C is a example of a low accumulation site on the east Antarctic plateau, while NGRIP is representative of the conditions at sites with high elevation and close to the ice divide of the Greenland ice sheet. We tune the model based on modern day density data by introducing the fudge factors f_o and f_1 on k_o and k_1 in equations 4.21 and 4.22 respectively. The parameters f_o and f_1 are tuned to fit the Holocene measured density profiles. The density calculations are presented in figures 4.7 and 4.8.

In figure 4.9 we calculate close off depths for a number of accumulation–temperature combinations. As seen colder temperatures result in deeper close – off depths as do lower accumulation rates. From the isotope diffusion point of view this allows for exchange of water molecules for longer times. However this does not necessarily result in higher diffusion rates due to the temperature sensitivity of the diffusivity.

4.3.2 Diffusion length profiles for different ice core sites

One can evaluate equations 4.27 and 4.33 and in combination with the density calculations performed in the previous section estimate the value of the diffusion length for δ^{18}O and δD at different depths. By varying the parameters of the model one can simulate different conditions. Here we present calculated diffusion length profiles for Epica Dome C and NGRIP. The parameters used are mentioned on the plots.

One of the assumptions of the model of Johnsen et al. (2000) is that the process of firn diffusion ceases after the pore close–off depth. As a result, the value of the diffusion length "locks" at this depth. This can be seen in figures 4.10 and 4.11. After this point, ice thinning and ice diffusion are the two processes affecting the value of the diffusion length. These two processes are not described by the model we present in this section and thus not visible in the illustrated results. However certain assumptions can be made about these two processes and thus they can be accounted for as we will describe later.

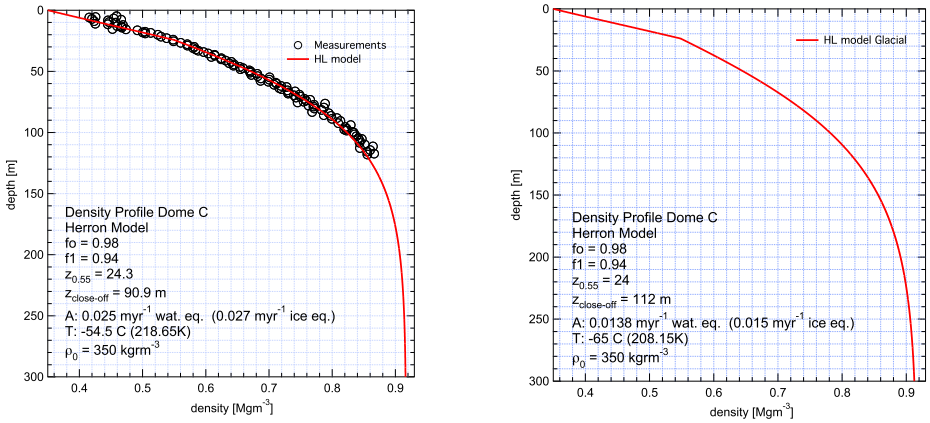

Figure 4.7: Measured and modelled density profiles for Dome C Antarctica. Left: Present conditions Right: Glacial conditions

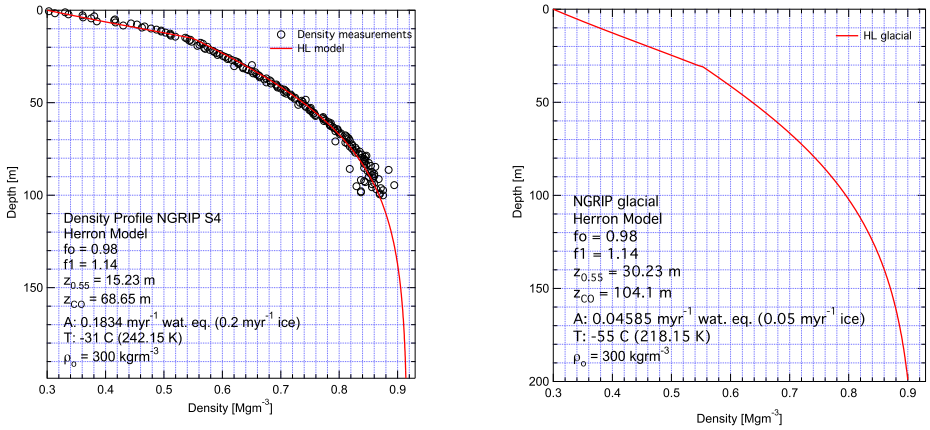

Figure 4.8: Measured and modelled density profiles for NGRIP Greenland. Left: Present conditions Right: Glacial conditions

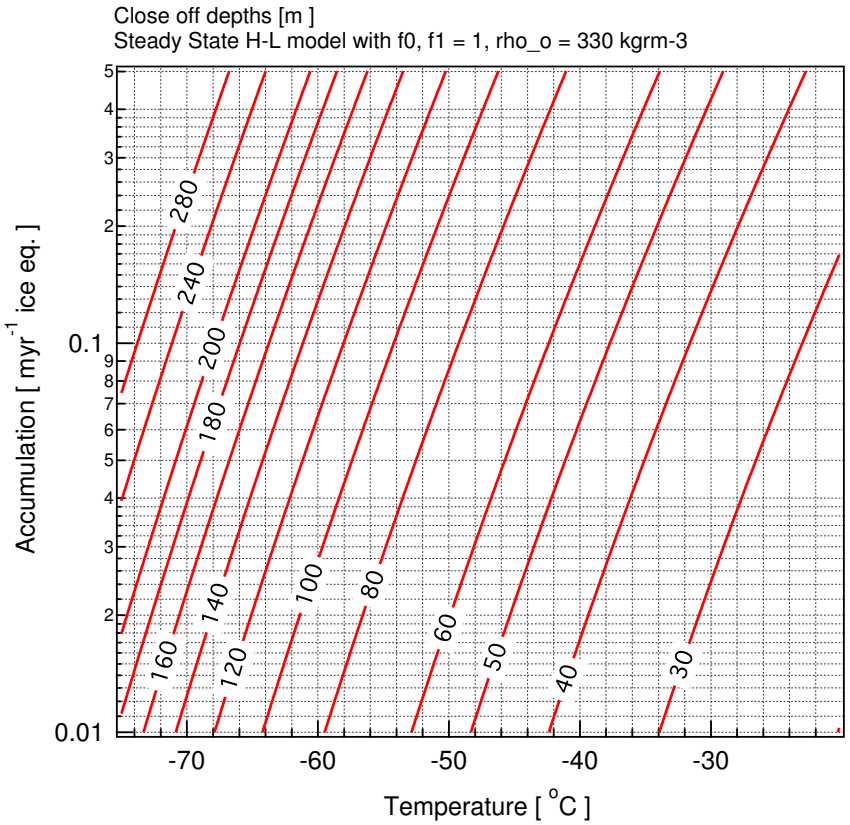

Figure 4.9: Modelled close off depths. Used the Herron and Langway model with $f_0 = f_1 = 1$, $\rho_0 = 330 kg\, m^{-3}$

4.3.3 Smoothing of cycles with different wavelengths

In order to estimate the smoothing of cycles with different wavelengths we refer back to equation 4.6 that describes the Gaussian filter of the diffusion process from deposition until close–off. The Fourier transform of $\mathcal{G}$ yields the transfer function of the system. This is itself a Gaussian and equal to (Abramowitz and Stegun, 1964):

$$\mathfrak{F}\left[\mathcal{G}\left(z\right)\right] = \hat{\mathcal{G}} = \int_{-\infty}^{\infty} \frac{1}{\sigma\sqrt{2\pi}} e^{-\frac{z^2}{2\sigma^2}} e^{-2\pi i f z} dz = e^{\frac{-k^2\sigma^2}{2}} \tag{4.34}$$

where $k = 2\pi f$, $\mathfrak{F}$ and the hat symbol, denotes the Fourier transform. Harmonics with an initial amplitude A_0 and wavenumber k will then be attenuated to a final amplitude that is equal to:

$$A = A_0 e^{\frac{-k^2\sigma^2}{2}} \tag{4.35}$$

In figure 4.12 we illustrate the relative smoothing imposed on cycles of different wavelengths for four different values of the diffusion length. It can be seen

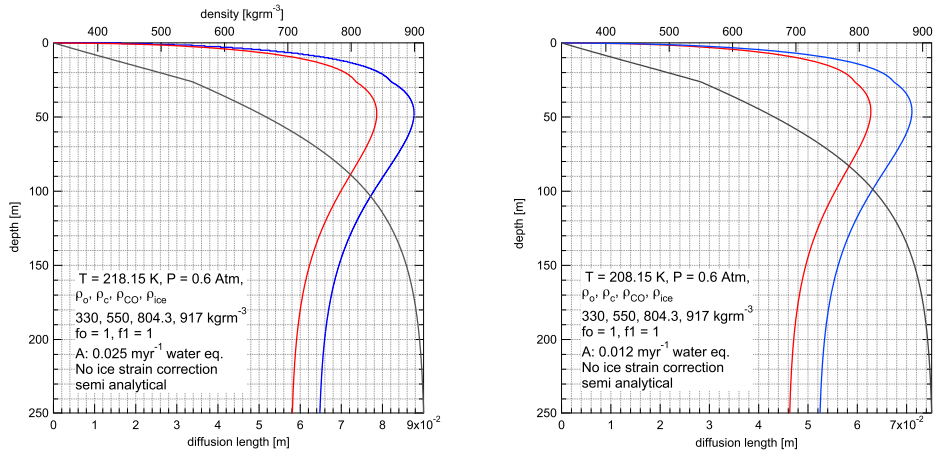

Figure 4.10: Modelled diffusion length profiles for Dome C Antarctica. Left: Present conditions Right: Glacial conditions. Blue (red) represents the diffusion length for δ^{18}O (δD)

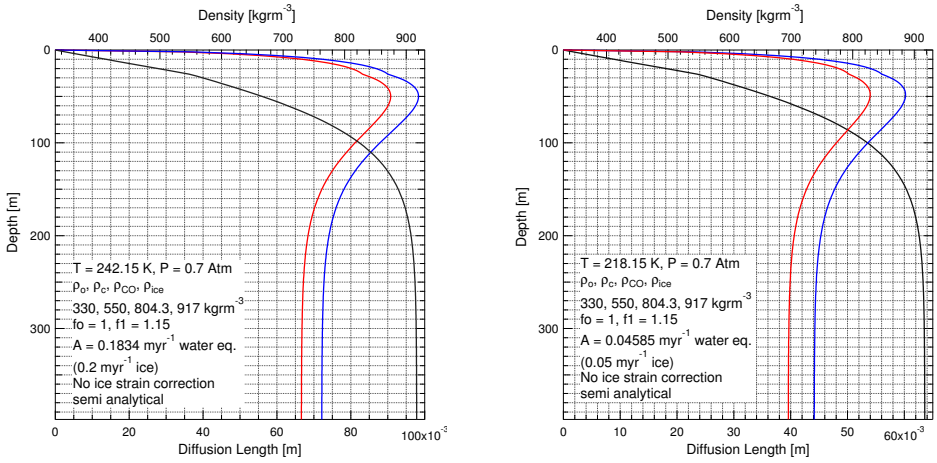

Figure 4.11: Modelled diffusion length profiles for NGRIP Greenland. Left: Present conditions Right: Last Glacial Maximum conditions. Blue (red) represents the diffusion length for δ^{18}O (δD)

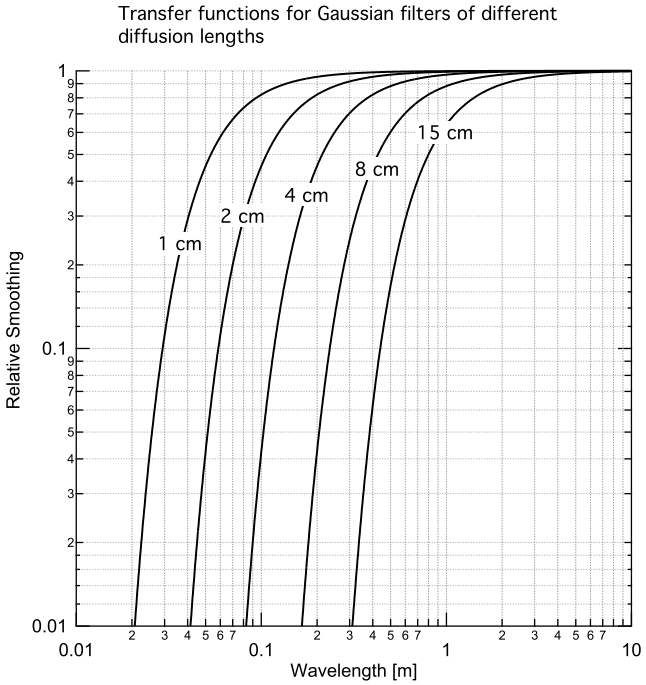

Figure 4.12: Transfer functions for various values of diffusion length σ

how the process of diffusion strongly attenuates signals with relatively high frequencies.

4.3.4 Self diffusion in the solid phase

At the close–off depth, the process of diffusion in the vapor phase ceases. After this point self diffusion takes place in the solid phase. It is believed that this diffusive process occurs via a vacancy mechanism with transport of molecules in the ice lattice. The diffusivity coefficient has been previously measured and found to be the same for $H_2^{18}O$, D_2O and T_2O (Brown and George, 1996). We are not aware of experimental data for HDO. Thus we make the assumption that the same diffusivity values apply for the latter too. The temperature dependence of the diffusivity is also assumed to be described by an Arrhenius type equation as:

$$D_{ice} = D_o \cdot e^{\left(-\frac{E_{act}}{kT}\right)} \tag{4.36}$$

Based on the results reported by Ramseier (1967) we use $E_{act} = 16.89\,\mathrm{kcal\,mol^{-1}}$ and $D_o = 9.13\,\mathrm{cm^2\,sec^{-1}}$.

In order to calculate the quantity σ_{ice} we start from equation 4.9 and use D_{ice} as the diffusivity parameter.

$$\frac{\mathrm{d}\sigma_{ice}^2}{\mathrm{d}t} - 2\,\dot{\varepsilon}_z(t)\,\sigma_{ice}^2 = 2D_{ice}(t) \tag{4.37}$$

Using the integrating factor $F = \exp\left(\int -2\dot{\varepsilon}_z\,(t)\;\mathrm{d}t\right)$ we get:

$$\frac{\mathrm{d}}{\mathrm{d}t}\left(\sigma^2_{ice}\, e^{\int -2\dot{\varepsilon}_z(t)\,\mathrm{d}t}\right) = 2D_{ice}(t)\; e^{\int -2\dot{\varepsilon}_z(t)\,\mathrm{d}t} \tag{4.38}$$

That finally yields

$$\sigma^2_{ice}(\tau) = S(\tau) \int_0^{\tau} 2D(t)\, S(t)^{-1}\;\mathrm{d}t \tag{4.39}$$

Where $S(\tau)$ is the total thinning of the ice layers with age τ. A first order approximation for the calculation of the self diffusion lengths from equation 4.39 is to assume isothermal ice and thus a fixed value for the diffusivity $D(t)$. However by doing this we underestimate the diffusion rates close to the bedrock, where the warmer temperatures (typically close to the pressure melting point) enhance the diffusion rates significantly. Here we follow a slightly more precise approach by using temperature measurements of the borehole and accordingly calculate the diffusivity for every depth. This approach implicitly assumes a steady state condition for the ice sheet at the location of the drilled ice core.

In figure 4.13 we present a calculated profile for the NGRIP core using borehole temperature data and a dating model by Sigfus J. Johnsen (personal communication). As seen the cold temperatures at the top of the core result in very slow diffusion rates expressed by the low values of σ^2_{ice}. At the deeper parts of the core the increasing temperatures enhance the diffusion resulting in high values of the diffusion length parameter.

4.3.5 The diffusion length signal - scenarios

Now that we have described the two main processes of water isotope diffusion we can calculate a diffusion length profile for different environmental conditions and ice flow parameters, thus simulating different ice core drilling sites. The two smoothing filters are going to add up and yield a total diffusion length that in the convolution fashion will be equal to:

$$\sigma^2_{total} = \sigma^2_{firn} + \sigma^2_{ice} \tag{4.40}$$

In the following example we focus on the NGRIP profile, demonstrating how the input parameters affect the outcome of the model. For the temperature history we follow a simplified approach. We convert the δ^{18}O profile to temperature using a fixed isotope slope $\alpha = 0.5\,‰\,K^{-1}$. In order to do that we need one fixed point and for that we use present day conditions. With $\delta^{18}O_{pres}$ we refer to the mean δ^{18}O value measured in the depth interval 20–50 m (55–170 years). We set $\delta^{18}O_{pres} = -34.98\,‰$. For the modern temperature at NGRIP we use $T_{pres} = 242.15\,K$. Parameters involved with the densification like f_o, f_1 and pressure are assumed to be constant with time. In order to account for the thinning of the ice layers we use a dating model by Sigfus Johnsen (personal communication). We also use the output of this model for the accumulation rates. In figures 4.14 and 4.15 we present the temperature, thinning and accumulation inputs we used to feed the diffusion calculations. The final result for the diffusion length of the δ^{18}O signal combined with the effect of ice diffusion is presented in figure 4.16.

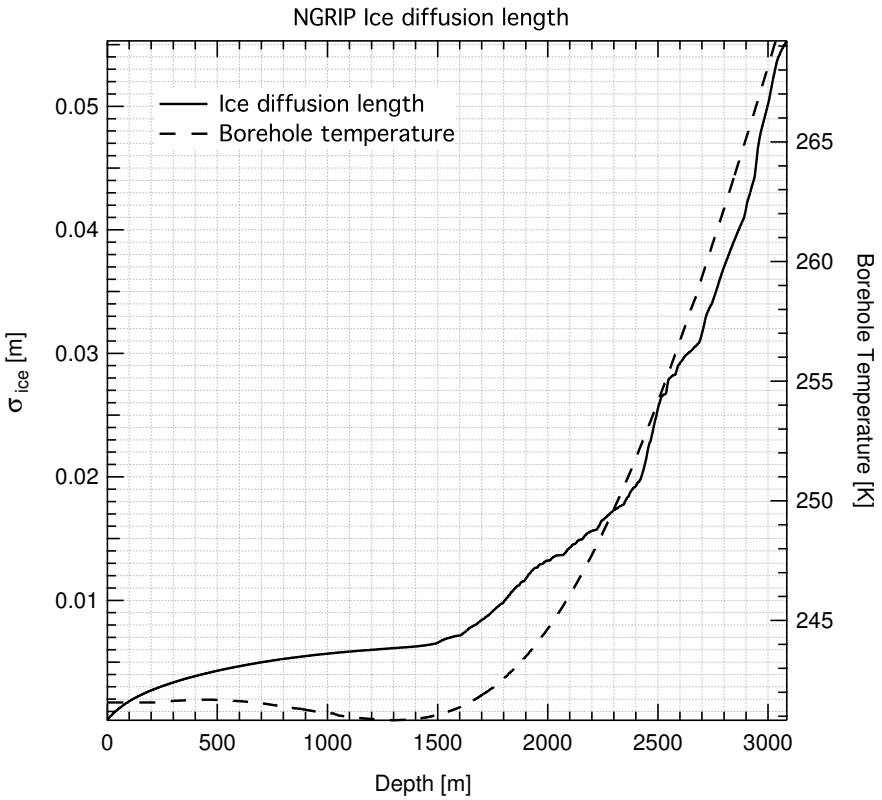

Figure 4.13: Self ice diffusion for NGRIP

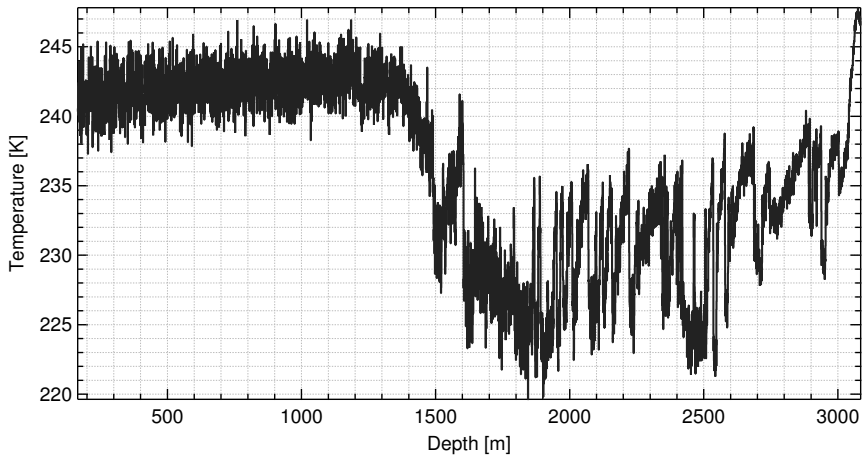

Figure 4.14: Temperature history based on the δ^{18}O profile and a slope of $0.5\,‰K^{-1}$

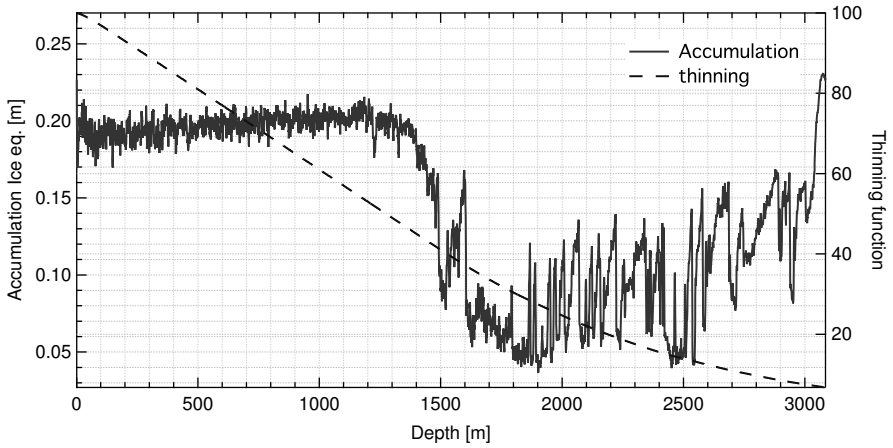

Figure 4.15: Accumulation and thinning used for the NGRIP diffusion profile calculation

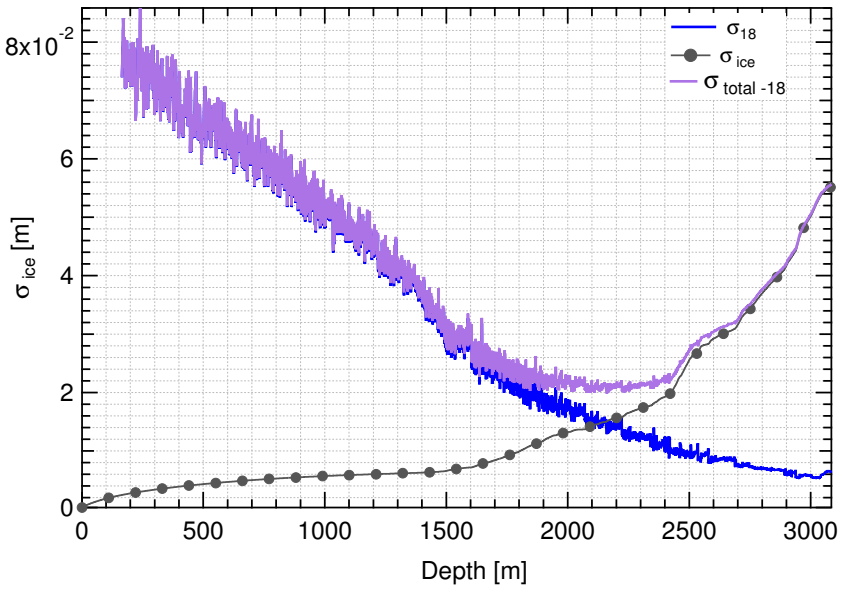

Figure 4.16: δ^{18}O Diffusion lengths for NGRIP based on an isotope slope equal to $0.5\,‰K^{-1}$

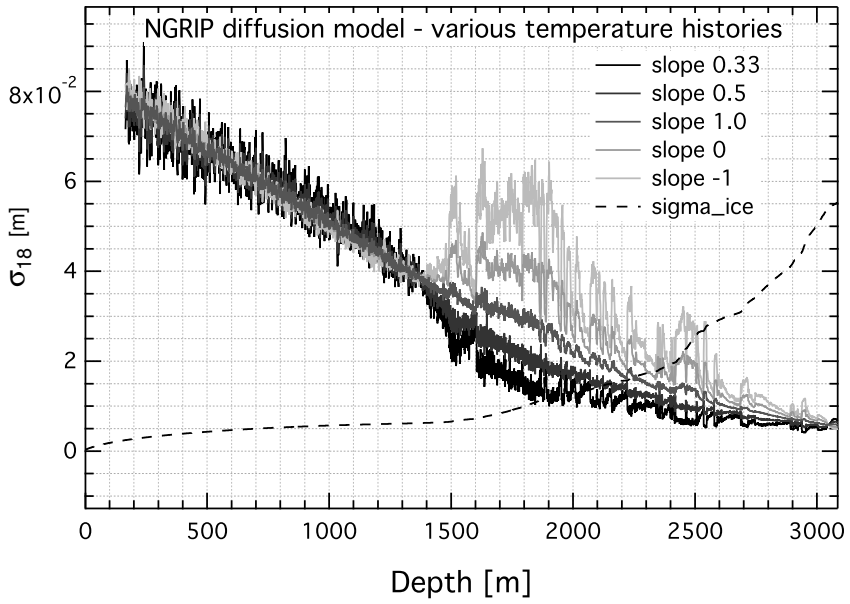

Figure 4.17: δ^{18}O Diffusion scenarios for δ^{18}O for NGRIP; the effect of self ice diffusion is illustrated separately

The result presented in figure 4.16 is only a demonstration of how the input parameters of the model affect the calculated diffusion length values. As described in previous sections we know that the isotope slope value is not constant with time. As a next step we "drive" our model with a number of various temperature histories by tuning the isotope slope to a set of different values. We choose to include scenarios with slopes equal to $0.33\,‰K^{-1}$ and $0.5\,‰K^{-1}$ typical for glacial conditions and interstadial events. We also include in our calculations the extreme scenarios of zero sensitivity and negative sensitivity of the δ^{18}O signal to temperature. It is interesting to point out that based on the results of figure 4.17, in the case of zero temperature change the diffusion signal is still affected by the changes in the accumulation signal used to "drive" the model.

In a similar way we present a set of diffusion scenarios for Dome C Antarctica (figure 4.18. For the past accumulation rates and the thinning function we use the EDC 3 timescale (Parrenin et al., 2007a). We do not use negative isotope sensitivities in this case but we include a scenario with almost zero temperature change during the last glacial termination. Again one can point out in this scenario (slope 5) the inversion of the direction of the signal with diffusion length values decreasing over the termination.

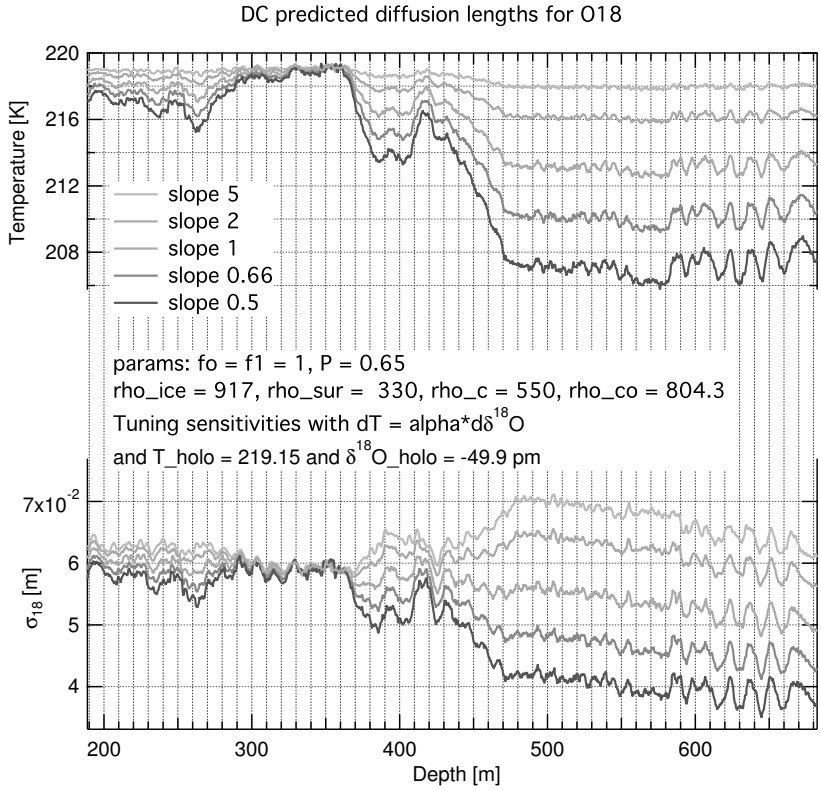

Figure 4.18: δ^{18}O Diffusion scenarios for Dome C Antarctica over the last glacial termination

4.4 Diffusion length based on high resolution data

It is possible to estimate the value of the diffusion length based on δ^{18}O and δD data of sufficiently high resolution. Based on equation 4.35 the power spectral density of an isotopic signal that has undergone a diffusive process and is sampled with a resolution equal to Δx will be:

$$P_s = P_0\, e^{-k^2\sigma^2} \text{ where } k = 2\pi f \text{ and } f \in \left[0,\, \frac{1}{2\Delta x}\right] \tag{4.41}$$

Any attempt to measure the isotopic signal will result in measurement noise $\eta(f)$. This noise signal will also affect the power spectral density. Through observations of real water isotope time series, we find appropriate to use a 1st order autoregressive order model (AR–1), thus assuming "red noise". Such a signal with variance σ_η^2 and φ_1 being the value of the autoregressive parameter will present a power spectral density that can be described by equation 4.42.

$$|\eta(f)|^2 = \frac{\sigma_\eta^2 \Delta x}{|1 + \varphi_1 \exp(-2\pi \jmath f \Delta x)|^2} \tag{4.42}$$

Summing up equations 4.41 and 4.42 we can get an estimate of the power spectral density expected for different values of the diffusion length. In this way it is also possible to estimate prior to a measurement what is the appropriate noise level and resolution of the analytical system to be used. Here we assume different analytical settings in terms of precision and resolution and estimate the obtained power spectrum for a signal with diffusion length equal to 5 cm. It can be seen how the lower resolution ($\Delta x = 5$ cm) results in spectra where the noise level is poorly estimated compared to the higher resolution of $\Delta x = 2$ cm. The effect of the higher noise level is also an important parameter because it affects the quality of the low frequency signal estimation. In any case for this particular scenario, a minimum resolution of 5 cm would be necessary, else the estimation of the spectrum would not see the "noise tail" thus resulting in a poor estimate of the diffusion length parameter.

4.4.1 The spectral estimation

In this study we will be using an all-pole method for the estimation of the spectrum. Assuming a p–order autoregressive process the estimate of the power spectrum will be given by $\hat{P}_{AR}$ (Kay and Marple, 1981; Hayes, 1996):

$$\hat{P}_{AR}(k) = \frac{\sigma_{AR}^2\, \Delta t}{\left|1 + \sum_{m=1}^{p} \hat{\alpha}_m e^{-\jmath k m \Delta t}\right|^2} \tag{4.43}$$

where σ_{AR}^2 is the variance of the autoregressive process and α_m the coefficients of the autoregressive filter. In order to solve equation 4.43 one needs an estimate the terms $\left\{\sigma_{AR}^2, \alpha_1, \alpha_2, \ldots. \alpha_{p-1}, \alpha_p\right\}$. To do that we use the algorithm introduced by Burg (1975) and implement a procedure outlined by Andersen (1974).

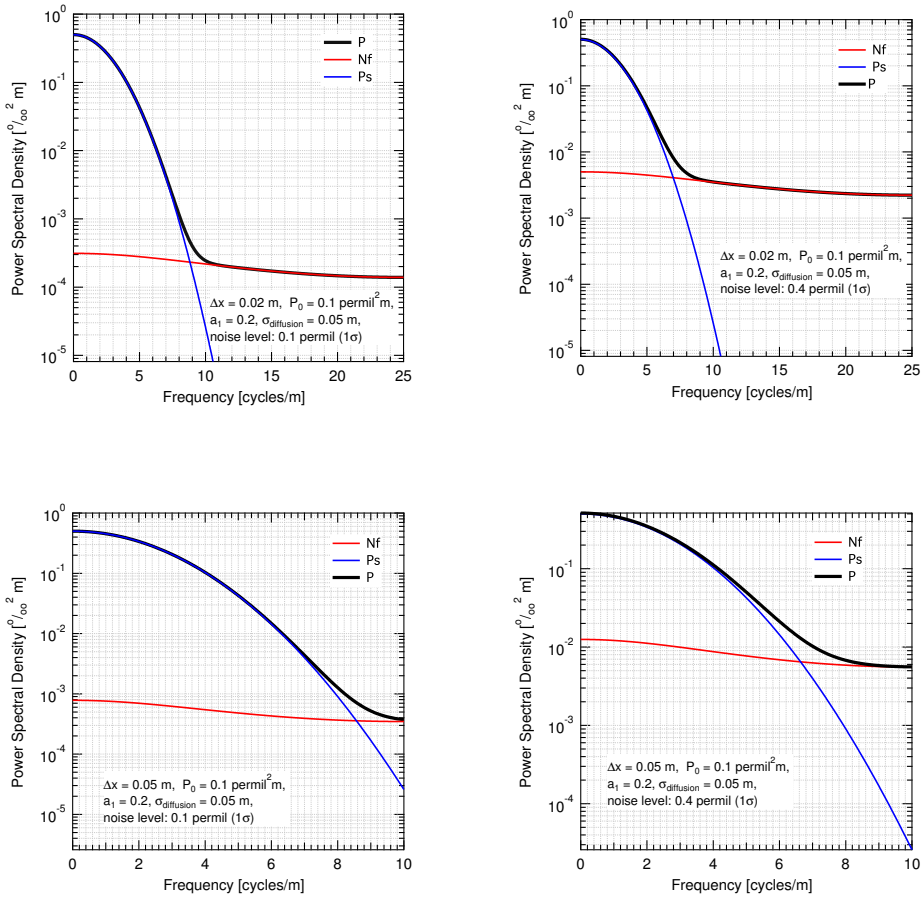

Figure 4.19: Estimated power spectra for different settings of the analytical system's precision and resolution. Diffusion length is set to 5 cm

The selection of the order of the model is a matter of discussion in relevant textbooks and there exist techniques for the selection of the appropriate order of the AR model. In general the higher the order of the model used, the better the spectral resolution and thus two neighboring spectral peaks can be better resolved. However, increasing the order of the AR filter can result in "artificial" peaks in the spectrum. In our case, the intention is to describe the general structure of the power spectrum, focusing on the level of the noise signal $|\eta(f)|^2$ and the behavior of P_s that contains information on the diffusion length. Thus we choose not to apply any of the criteria for model order selection and restrict the modelling to relatively small order values, such that no obvious spectral peaks appear in the estimated spectrum. We also note that at the ice depths we focus our work in, the annual signal is expected to be undetectable due to the small annual layer thickness and the attenuation imposed by the firn and ice diffusion we have estimated.

An example of a power spectrum estimation is given here. A set of high resolution δ^{18}O data (figure 4.20) from the early holocene part of the Dome C core, at a resolution of 2.5 cm is processed with Burg's spectral estimation method. The spectrum is estimated with an AR filter of order p = 20. The size of the dataset is 350 points. The diffusion length in this case is estimated by minimizing the spectrum - model residuals following a least squares approcch. As a model we use:

$$\mathbb{P}(f) = P_s(f) + P_\eta(f) = P_0\, e^{-(2\pi f)^2 \sigma_{18}^2} + \frac{\sigma_\eta^2 \Delta x}{\left|1 + \varphi_1 \exp(-2\pi \jmath f \Delta x)\right|^2} \quad (4.44)$$

where we tune the parameters P_0, σ_η, φ_1, σ_{18} to obtain the best fit between $\mathbb{P}(f)$ and $\hat{P}_{AR}$.

The estimated value of σ_{18} needs to be corrected for the effects of ice diffusion and sampling smoothing. In the case of an online analytical system as the one presented in chapter 3 a correction can be applied using the diffusion length σ_{cfa}^2 of the analytical system. In the case of discrete sampling one can calculate the diffusion length σ_{dis} of a Gaussian filter that results in equal attenuation when compared to the effect of a rectangular window of width Δ. In this case the responses are (Abramowitz and Stegun, 1964; Oppenheim, 1997):

$$e^{\left(-4\pi^2 f^2 \sigma_{dis}^2\right)} = \widehat{\Pi}(f) = \int_{-\Delta/2}^{\Delta/2} e^{-\jmath 2\pi f t}\, \mathrm{d}t \quad (4.45)$$

where Δ is the resolution of the discrete sampling that determines the Nyquist frequency as $f_{Nyq} = \frac{1}{2\Delta}$ and $\widehat{\Pi}(f)$ is the Fourier transform of the rectangular function. Equation 4.45 yields:

$$\sigma_{dis} = \frac{\Delta^2}{\pi^2} \ln\left(\frac{\pi}{2}\right) \quad (4.46)$$

As a result the corrected firn diffusion length σ_{18cor} is given by (use σ_{dis} or σ_{cfa} accordingly):

$$\sigma_{18cor} = \sqrt{\sigma_{18}^2 - \sigma_{ice}^2 - \sigma_{dis}^2} \quad (4.47)$$

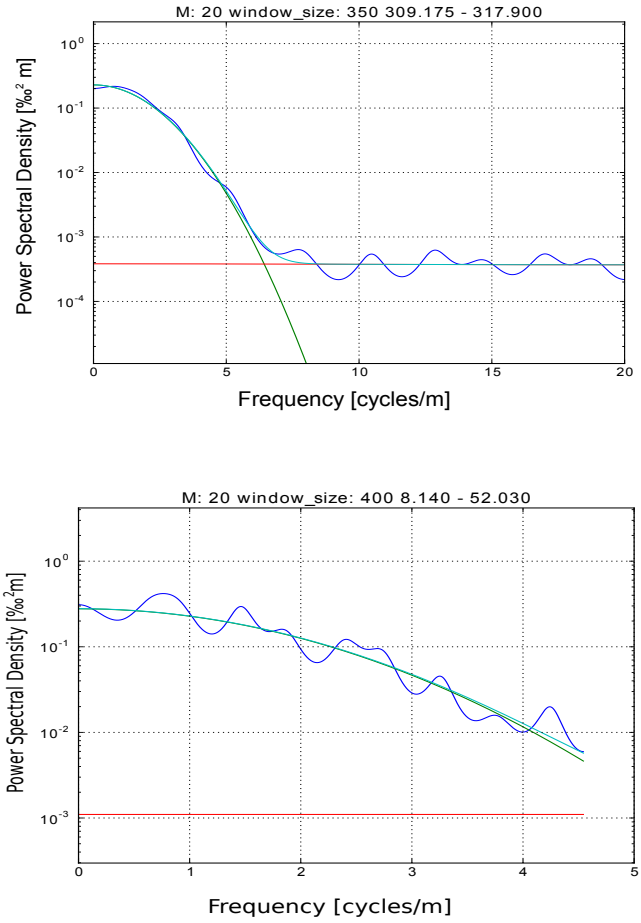

Figure 4.20: A model for the spectrum of the diffusion process P_s and the measurement noise spectrum P_η is applied to describe the estimated spectrum $\hat{P}_{AR}$. The spectrum presented is estimated based on 2.5 cm (top) and 11 cm (bottom) resolution δ^{18}O data from Dome C, Antarctica

Name	Resolution [m]	Depth [m]	Bottom Age [ka]
Holo22pbag	0.025	308.025 - 317.925	10.3
LGM22pbag	0.025	618.225 - 628.1	31.5
DC5pbag	0.11	7.81 - 1487.64	109

Table 4.1: The 3 sets of samples from Dome C used in this study

It can be seen that the combined effect of ice diffusion and sampling determines the point at which the firn diffusion information cannot be restored anymore. This happens when:

$$\sigma_{18}^2 \leq \sigma_{ice}^2 + \sigma_{dis}^2 \tag{4.48}$$

4.5 The Dome C example

In this section we will exemplify the use of the models and data analysis tools we described in the previous sections by using isotope data from Dome C, Antarctica. Two data sets at different resolutions will be compared with the results of the diffusion model driven with different temperature scenarios. We look into how the temperature affects the diffusion length signal but assume that the accumulation as given by the ice flow/dating models is correct. The results presented here constitute work that is under developement. We believe that further analysis and tests will be required before we draw any conclusions that can be considered as solid and potentially ready for a peer-reviewed process.

We utilize two different types of isotope samples (table 4.1) The first set consists of discrete samples cut at a resolution of 11 cm and measured on a mass spectrometry system. The current dataset (figure 4.21) extends to a depth of 1500 m ($\approx$ 109 ka BP). Over the transition at a depth of approximately 450 m each sample contains roughly 7 years. The dataset has been inspected and cleaned up from outliers that were most likely caused by excessive sample evaporation. Simple linear interpolation was used to fill single sample gaps present in the dataset. The second dataset we use consists of two sets of samples cut at a resolution of 2.5 cm (figure 4.5). These sets are representative of early Holocene and Last Glacial Maximum conditions respectively. Both sets span $\approx$10m of ice.

For the 11 cm resolution set we perform the spectral analysis procedure by sliding a window over the δ^{18}O dataset. Based on the calculated power spectral density we estimate a value for the diffusion length. The size of the window in this case is 400 points long (44 m) and is shifted by 10 points (1.1 m) on every iteration. The order of the autoregressive filter used for the spectral estimation is $p = 20$. For the case of the 2.5 cm resolution datasets, the window used is 350 points long (8.75 m) and is shifted by 1 point at a time. The purpose of using a sliding window over a small dataset like this is to obtain an estimate of the stability of the spectral estimation. The order of the autoregressive filter used for the 2.5 cm resolution data is also $p = 20$.

We can report an overall good fit of the obtained spectrum estimates using the procedure outlined in section 4.4.1. This is particularly the case for the 2.5

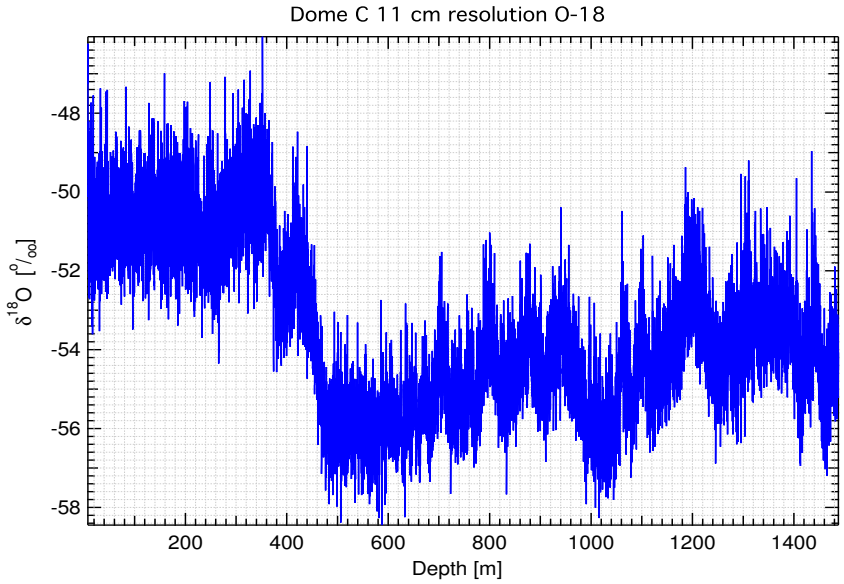

Figure 4.21: Dome C 11 cm resolution δ^{18}O data

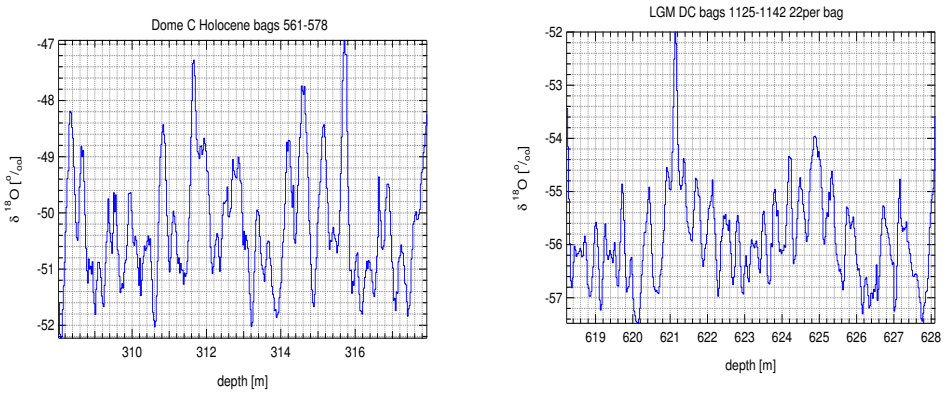

Figure 4.22: Dome C 2.5 cm resolution δ^{18}O data

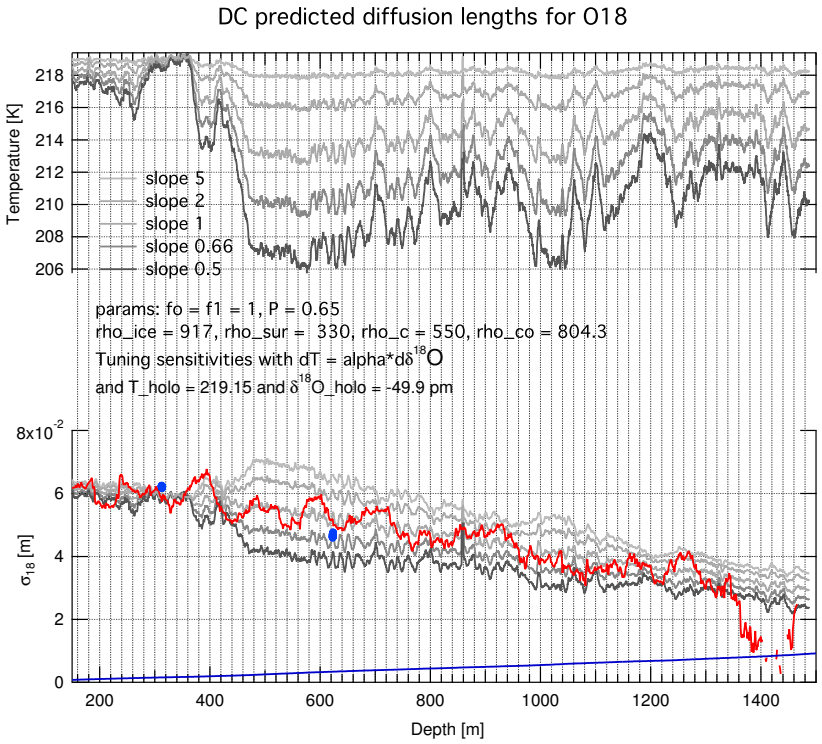

Figure 4.23: A model - data comparison for Dome C δ^{18}O diffusion length. With gray different temperature/ diffusion length history scenarios. Blue line: modeled ice diffusion length. Red line: Estimated δ^{18}O diffusion lengths from 11cm resolution δ^{18}O data. Blue dots: Estimated δ^{18}O diffusion lengths from 2.5 cm resolution data

cm resolution data. A typical spectrum as presented in figure 4.20 contains both the low frequency diffusion signature as well as noise a clear "tail". In this way the parameters used to describe the signals $P_s(f)$ and $P_\eta(f)$ are constrained in a better way. On the other hand the resolution obtained with the 11 cm data is not sufficient to characterize the noise level. The Nyquist frequency is equal to 4.54 cycles/m. At this frequency we can see (figure 4.20) that the diffusion signal has still not reached the level of the noise. As a result, we can expect that the estimation of the fit parameters is likely of lower quality, compared to the estimates obtained from the 2.5 cm resolution data. This example reveals the importance of the sampling resolution for the purpose of isotope diffusion studies.

We present the results of the spectral estimation in figure 4.23. Some general remarks can be made concerning these results. First we observe a general agreement between the predictions of the diffusion model and the diffusion length estimation based on the spectral analysis of the 11 cm and 2.5 cm resolution data corrected for ice and sampling diffusion. Additionally, we observe a good agreement between the spectral estimates from 2.5 cm and 11 cm data, some-

thing that points to a fairly robust spectral estimation procedure. Considering the different sampling resolution this agreement also indicates the validity of the correction applied for the diffusive effects caused by the discrete sampling as described in equation 4.46.

A closer look at the top 300 m of the reconstruction reveals a good model–data agreement for the Holocene part of the core. This is the part of the core that one can expect the diffusion model to be more accurate. The dating markers used to constrain the ice flow model parameters, are characterized by a relatively low error, well below 1 ka (Parrenin et al., 2007a). It is also very likely that the ice sheet thickness did not undergo significant changes during this period (Parrenin et al., 2007b). As a result, the calculation of the thinning function and the past accumulation rates should be relatively accurate. The five isotope slope scenarios we outline in figure 4.23 follow each other very closely during the Holocene mainly due the fact that the δ^{18}O signal is relatively stable. The agreement between model and data for this part of the core indicates that the spectral estimation, the optimization routine for the spectrum parameters as well as the post corrections for sampling diffusion and ice diffusion can deliver reasonable results for the value of the diffusion length, based on actual ice core data.

Deeper in the core, the estimated diffusion lengths seem to satisfy a combination of temperature histories for different depths. This is to some extent expected, considering the time dependency of the isotope slope observed in Greenland. We can observe that generally the diffusion length profile points to a slope that varies between 0.65 and 1 and in some parts to a value as high as 2. Further down, at a depth of about 1360 m we observe a sudden decrease in the value of the diffusion length and some meters deeper we see that our calculations fall in the condition described by equation 4.48. We can also report that the general shape of the estimated spectra does not allow for a good fit and thus results deeper than this depth should be considered with caution. Sections of the core deeper that 1500 m have not been analyzed but it is likely that the combined effect of the strain and the ice and sampling diffusion results in complete loss of information. One cannot exclude the possibility that ice from the previous interglacial (stage 5.5) probably contains diffusion information. This is an educated guess based on the assumption that temperatures during that period, generally assumed to be warmer than today, resulted in relatively high diffusion length values at the base of the firn.

In figure 4.24 we present the temperature history inferred by the estimated diffusion length profile and the temperature history reported by Jouzel et al. (2007) using the combined δD and D_{xs} signal. An overall agreement over the Holocene can be observed. Additionally the glacial - interglacial temperature difference is comparable between the two estimates and approximately equal to 8 K. We see a strong discrepancy between the two estimates after 90 kyr. We believe that this discrepancy is due to a poor spectral estimate and subsequently a poor estimate of the diffusion length for this section. Between 20 and 60 kyr the diffusion derived temperatures indicate an isotope slope that is higher than the one assumed by Jouzel et al. (2007). This is expressed as a rather large temperature change through the series of the D/O equivalent warming events, commonly referred to as "Antarctic Isotope Maxima" (hereafter AIM events). In fact, the maxima of the warming events appear to be almost as warm as the Holocene temperatures at approximately $-55°$C.

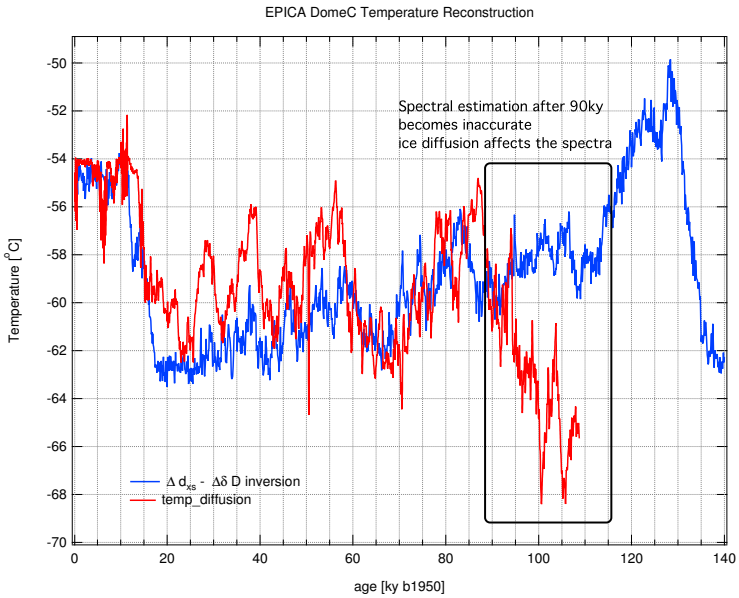

Figure 4.24: Temperature history for Dome C inferred by firn diffusion (red) and the combined δD –D_{xs} signal. Results below 90kyr for the red curve suffer from poor spectral estimation and should not be considered.

4.5.1 The differential diffusion signal

In an attempt to overcome the uncertainty of the ice diffusion length estimate, one can use the differential diffusion signal. The differential signal is mainly driven by the different dependence of the fractionation factors for δ^{18}O and δD on temperature. Different accumulation rates affect the densification rates and subsequently the length of the firn column in which the diffusion process occurs Based on the fact that the ice diffusion length is the same for both the δ^{18}O and δD signal, and considering equation 4.47, the differential diffusion length $\Delta\sigma^2$ can be estimated directly from the data without the need to correct for ice and sampling diffusion (equation 4.49).

$$\Delta\sigma^2 = \sigma^2_{18cor} - \sigma^2_{Dcor} = \sigma^2_{18} - \sigma^2_D \tag{4.49}$$

In a similar way as with the σ_{18} signal, different combinations of past accumulation and temperature can be used in order to infer the value of $\Delta\sigma^2$, assuming certain values for the parameters involved in the densification process. We illustrate this in the contour plot of figure 4.25. In this case we do not consider the thinning of the ice layers in the calculation and all values reported refer to ice equivalent diffusion lengths at the close off depth, expressed in cm^2. As a result a value for $\Delta\sigma^2$ estimated from ice core data has to be corrected for ice thinning in order to be compared to the values at the close – off depth as presented in figure 4.25. Assuming a value $\Delta\sigma^2_i$ estimated from ice core samples at depth z_i and the thinning function at this depth being equal to $S(z_i)$ then the close–off equivalent differential diffusion length value $\Delta\sigma^2_{co}$ will be given by:

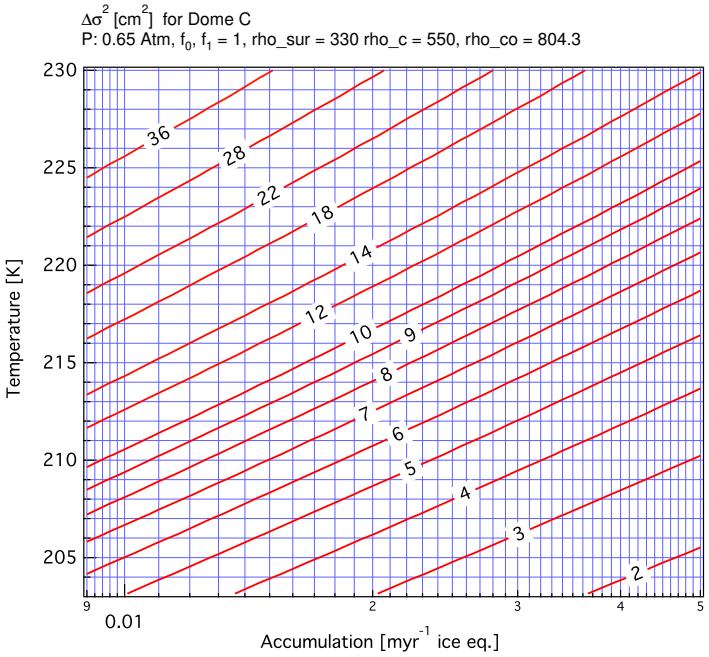

Figure 4.25: Differential diffusion length values for various combinations of temperature and accumulation rate. $\Delta\sigma^2$ is expressed in cm^2 (ice equivalnent) at the close – off depth.

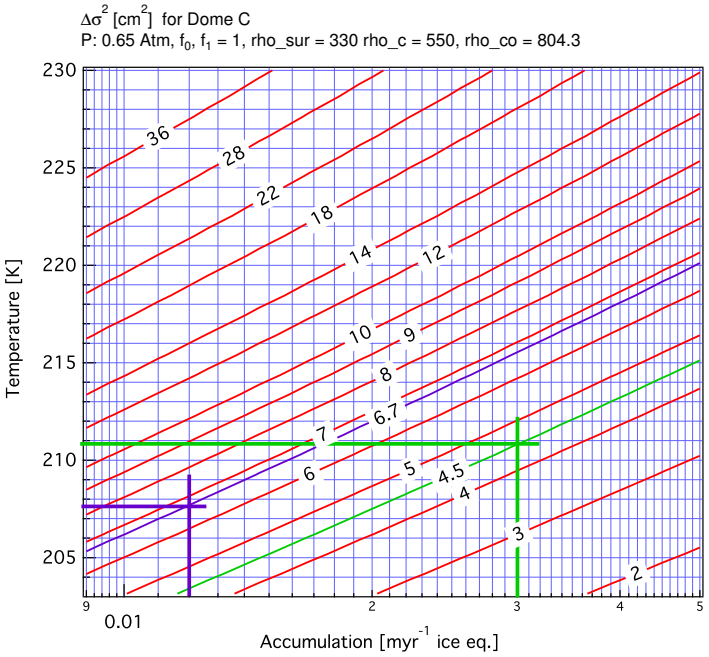

Figure 4.26: $\Delta\sigma^2$ estimates for the 2.5 cm resolution sets Holo22pbag (green) and LGM22pbag (violet)

$$\Delta\sigma^2_{co} = \frac{\Delta\sigma^2_i}{S^2(z_i)} \tag{4.50}$$

It is obvious that to perform this type of analysis, measurements of δ^{18}O and δD on the same ice core sample are necessary. The sets Holo22pbag and LGM22pbag are the only ones that have been measured for both isotopes. The $\Delta\sigma^2$ estimates for Holo22pbag and LGM22pbag are shown in figure 4.26 with green and violet color respectively. These estimates are corrected for ice thinning, so they refer to diffusion lengths at the close-off depth.

As seen in figure 4.26, based on the expected accumulation rates the temperature estimates we obtain, suggest temperatures lower than what reported by Jouzel et al. (2007) and what we estimate based only on the δ^{18}O signal with ice diffusion correction. For the Holocene set, the $\Delta\sigma^2$ estimate points to considerably lower temperatures at approximately 211 K as opposed to the 218 K as calculated in the two fore mentioned studies. For the Last Glacial Maximum the $\Delta\sigma^2$ estimate seems to be closer to the other two studies, yet the inferred temperature is still lower at approximately 208 K (210 K in Jouzel et al. (2007) and 211 K in the current study based on σ_{18}). Based on these two temperatures the glacial interglacial temperature step is only 3 K.

4.6 Discussion and conclusions

In this chapter we described the use of the classical isotope slope and the potential complications that can arise when the latter is applied for climatic conditions different than present. We outlined cases in which the extrapolation of the isotope slope has led to wrong conclusions about the temperature history of ice core sites and described some paleothermometry techniques that have been used to infer temperature histories in a more reliable way.

Based on the current knowledge and the available data we propose that for the specific case of Dome C, a site typical for the conditions over the east Antarctic plateau, the temperature history may need to be reconsidered and possibly revised. With this goal in mind we show that the water isotope diffusion process that occurs during the densification of firn can yield valuable information about past temperatures. With the combined use of densification and diffusion models we describe the diffusion process and derive expressions for the diffusion length. Based on a diffusivity parametrization, the values of the diffusion length can then be modelled. We also show how the self diffusion in ice can be described and present an estimate based on the measured borehole temperature profile for two sites, NGRIP and Dome C.

Following a signal analysis approach we calculate the transfer function of the firn diffusion process and show how isotopic cycles with different wavelengths are attenuated. Using δ^{18}O data from ice core samples we show that an estimate of the diffusion length can be obtained from the power spectral density of the dataset. We use Burg's spectral estimation method assuming an autoregressive model for the δ^{18}O time series. We also assume that the noise is of red type and we use a Markov model to describe it. We obtain a good agreement for the diffusion length estimates based on 11 cm samples spanning the first 1500 m of the Dome C core and 2 short sets of 2.5 cm resolution samples. This agreement points to a satisfactory spectral estimate. Comparing the diffusion length values obtained from the δ^{18}O data with those obtained by feeding the diffusion model with different temperature scenarios, we propose a diffusion length history that suggests a variable value for the isotope slope along the record. The temperature history inferred by these isotope slope values suggests a glacial– interglacial temperature step comparable to what the existing studies suggest. Nevertheless the temperature inferred for the AIM events is considerably higher.

We also introduce the use of the differential diffusion signal. The main advantage of this approach is that parameters as the ice diffusion and the sampling diffusion fall out of the analysis. Regarding the ice diffusion, one needs to know the ice self diffusion coefficient as a function of temperature. Published experimental works seem to conclude that the self diffusion of different isotopologues can be described by the same diffusivity coefficients. However, the spread of the reported values for the activation energy and the pre exponential factors in the Arrhenius–type diffusivity parametrization is quite large. On the other hand the diffusion imposed by the discrete sampling procedure is well characterized. The analysis we perform using the differential diffusion signal suggests temperatures considerably lower than the existing paleotemperature estimates and the estimates inferred by the single isotope diffusion model. The glacial–interglacial temperature step is in this case much lower.

With these results in mind, we can draw some conclusions. Based on the agreement regarding the diffusion length value for δ^{18}O , between datasets of

different resolution, we can assume that the procedures we followed for spectral estimation, as well as for post corrections for ice self diffusion and sampling are satisfactory. Regarding the ice diffusion we can also comment that in the particular case of Dome C and the depth at which we perform our analysis, the influence of the ice diffusion is marginal due to the cold temperatures at the top part of the ice column.

We can verify that the firn diffusion process imprints a measurable temperature signal that can be extracted from ice core data. Isotopic measurements with high resolution and precision are essential for good spectral estimation. The temperatures inferred from the analysis we performed using both the single and the dual/differential diffusion signal, are within a reasonable range and that points to the applicability of the method for paleothermometry studies. Based on the 11 cm data that span a longer part of the Dome C ice core we were able to get temperature estimates that showed a good correlation to the isotope profile and thus the up to date temperature history estimate. Groups of AIM events can also be identified. We faced a problem getting a reasonable spectral and subsequently temperature estimate after 90 kyr BP. We believe that this failure is due to the ice diffusion length being comparable to the firn diffusion at these depths. The systematically warmer temperatures estimated for the section between the last glacial termination and about 70 kyr BP, imply that the firn column has been receiving more heat during this period, than what is currently believed. If this is indeed the case then one can foresee implications for gas fractionation studies as well as studies modelling the Dome C borehole temperature profile. It would certainly be an interesting experiment to use the temperature history we have estimated here and with this drive a gas fractionation model, and see how the model–data discrepancy described in section 4.1.3 is affected.

Regarding the differential diffusion signal, it is apparent that the outcome of our estimations is inaccurate. Considering that the outcome of the single δ^{18}O diffusion infers Holocene temperatures accurately and the differential signal shows a discrepancy of about 7 K, it would be a reasonable next step to investigate the single diffusion of the δD signal for possible inaccuracies. Unfortunately this is not possible as δD measurements exist only at a resolution of 55 cm for the Dome C core. This resolution is very low for the purpose of such a study. Thus it still remains an open question why the differential diffusion approach fails to reproduce modern temperatures and further studies that also need to involve δD high resolution measurements are necessary.

Chapter 5

Outlook

Several ideas have emerged during this project as part of individual or collaborative work that have not been developed further but they constitute possible starting points for further future research. Based on the extensive experience gathered from the development of the online water isotope system as well as through the collaborative work performed on gas concentration measurements, some new possible improvements can be proposed. In the framework of the NEEM ice core drilling project, our work has yielded water isotope data of high resolution and precision. The data set covers some very interesting sections of the core as the Younger Dryas and the Bølling Alerød transitions as well as what seems to be an undisturbed section of the Eemian interglacial. The work on the Dome C paleotemperature reconstruction should also be considered in more depth and several ideas that combine more data and modelling approaches could possibly yield results that are more conclusive and solid.

5.1 Next steps in experimentation

The measurement platform we have created can further be developed and improved. Laser spectroscopy can be applied for ice core measurements focused in other species in the gaseous phase. Measurements of gas concentrations and isotopic ratios are obviously within the scope of interest and some first steps have been undertaken to this direction during the NEEM ice core project with the measurement of CH_4 concentrations in an online fashion. One step further, certain advances in laser spectroscopy that are currently under way, can possibly be applicable in the field of ice core online measurements and here we outline some of them.

5.1.1 Enhancing resolution

For both the water isotopes and gas concentrations measurements, one of the main gains of the online measurement approach is the potential for high resolution measurements. Certain steps towards increasing the resolution of the current measurement systems can be taken. They concern both the sample preparation system as well as the laser spectrometer itself.

To that end, the volume of all gaseous sample transfer lines can be thus

further reduced. That implies, tubing of smaller diameters as well as elimination of any "dead volume" parts in the sample transfer lines. An extra measure that can possibly be tested is to adjust the diffusivity coefficients of the transfered gases by decreasing the temperature of the tubing system and subsequently the transferred molecules.

Looking at the Picarro laser spectrometer itself one can see that the shape of the optical cavity and the optical configuration of the high reflectivity mirrors allows for the V-shaped optical path. However the total volume of the cavity at its current form (approximately $30\,\mathrm{scm}^3$) is essentially not used by the laser beam. This is one of the main advantages of this optical configuration when compared to different approaches as the ICOS spectroscopy (O'Keefe et al., 1999) or implemetations of multipass Herriot cells (McManus and Kebabian, 1990). In these techniques the optical path of the laser beam forms a pattern that requires mirror surface substantially larger than the size of the beam itself. As a result mirrors of large diameter and eventually optical cavities of large volume are required. It becomes then apparent that it is possible to reduce the volume of the optical cavity of the Picarro analyzer to the very necessary volume used only by the laser beam. This approach has already been followed by Romanini et al. (2006) in an optical feedback cavity–enhanced absorption spectrometer tailored for CH_4 atmospheric measurements.

In a similar way, Stowasser et al (personal communication) have proposed a modified version of the original Picarro cavity with a lower volume and an optimized flow path that minimizes dead volume (figure 5.1. The first results, evaluated in a manner similar to the one we propose in chapter 2, indicate an improvement in the obtained resolution. It remains to be seen how this change affects the performance of the analyzer in terms of precision and accuracy, although there is good indication that it should remain unaltered. Further work in this direction is already on the way and we also foresee the possibility of adapting these ideas for the water isotope measurement.

5.1.2 $\Delta^{17}O$

The measurement of $\delta^{17}O$ has been an experimental challenge for the IRMS community over the last years. In the "classical" CO_2 equilibration approach the fingerprint of the much more abundant $^{13}C^{16}O_2$ does not allow for a precise measurement of $^{17}O^{1}H_2$ on mass 45. The solution to this problem has been to convert H_2O to O_2. Different methods exist with Meijer and Li (1998) using electrolysis, while other studies like Barkan and Luz (2005) make use of CoF_3 for the conversion to O_2. The analytical procedure is typically time consuming and labor intensive.

Of particular interest for ice core science is the oxygen excess signal $\Delta^{17}O$ (Landais et al., 2008). Considering the isotope ratios ^{17}R and ^{18}R, one expects according to theory that

$$\frac{^{17}R_s}{^{17}R_r} = \left(\frac{^{18}R_s}{^{18}R_r}\right)^{\lambda} \tag{5.1}$$

where the indexes r and s denote reference and sample respectively and $\lambda = 0.5$. Measurements of meteoric waters result in $\lambda = 0.5279$ (Barkan and Luz, 2005). Using δ notations for equation 5.1 we get:

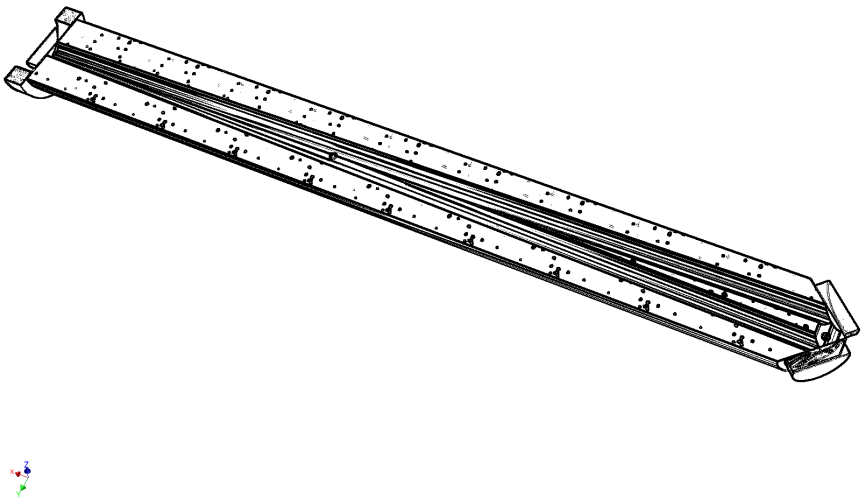

Figure 5.1: Low volume / high resolution version of the picarro optical cavity

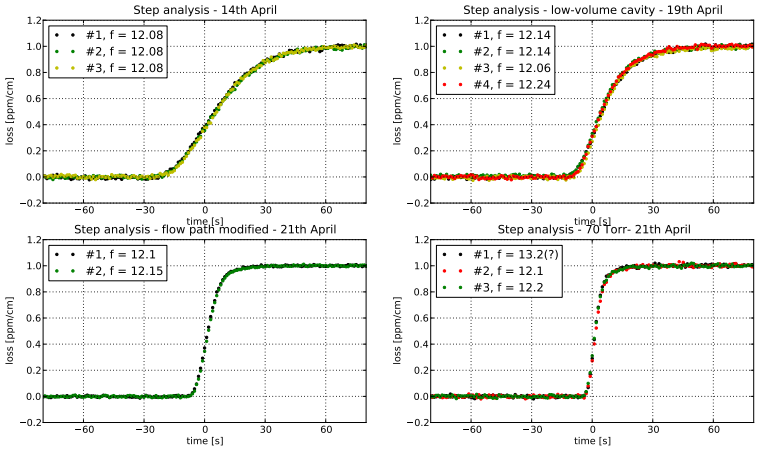

Figure 5.2: Step response of the CH_4 system with different optical cavity / inlet configurations. Top left: Unmodified Picarro cavity and inlet configuration; Top right: Low volume cavity - unmodified inlet section at 140 Torr; Bottom left: Low volume cavity, optimized inlet configuration at 140 Torr; Bottom right: Low volume cavity, optimized inlet configuration at 70 Torr

$$\ln\left(\delta^{17}\mathrm{O}-1\right)=\lambda\,\ln\left(\delta^{18}\mathrm{O}-1\right) \tag{5.2}$$

In a log plot equation 5.2 is a straight line and the deviations from this line determine $\Delta^{17}\mathrm{O}$.

Natural variations of ice core samples and present meteoric waters as measured by Landais et al. (2008) and Luz and Barkan (2010) lie in the permeg scale. In order to achieve this level of precision both studies follow an approach of long averaging for every sample. The 1σ combined uncertainties reported by Barkan and Luz (2005) are at the level of 0.01‰ and 0.02‰ for $\delta^{17}\mathrm{O}$ and $\delta^{18}\mathrm{O}$ respectively. Measuring the same sample 90 times they can achieve an improvement in precision. After this averaging is accounted for, Barkan and Luz (2005) report a 95% confidence interval equal to 0.003‰ and 0.006‰ for $\delta^{18}\mathrm{O}$ and $\delta^{17}\mathrm{O}$ respectively. The measurement of every sample requires a total of ≈ 2 hours.

It is clear that the key to this measurement is a precise system with minimum instrumental drift, allowing for long averaging and thus increasing precision with time. Based on the results we reported in section 2.3.1, we can see that we can achieve this precision levels for $\delta^{18}\mathrm{O}$ with the laser spectrometer system attached to the home build flash evaporator if we average for about 20 min for every individual sample.

As far as the measurement of $\delta^{17}\mathrm{O}$ is concerned, the laser spectrometer does not have such measuring capability yet. However absorption lines for $^{1}\mathrm{H}_2\,^{17}\mathrm{O}$ exist in the spectral region around $1.39\,\mu m$. Here we present a laser scan at the spectral region around $7183\,\mathrm{cm}^{-1}$ as reported in Iannone et al. (2009a) (figure 5.3. An absorption line for $^{1}\mathrm{H}_2\,^{17}\mathrm{O}$ can be found at 7183.73 cm^{-1}. Certain steps have been taken in collaboration with Picarro and the isotope labs in the University of Colorado in Boulder and the University of Washington, in order to investigate the feasibility of this measurement.

5.1.3 Multi–component analysis in the mid–IR

Based on the experience from the measuring campaigns at the NEEM ice core camp in Greenland during the years 2009-2011 we have concluded that sample preparation systems are prone to failures and their performance can significantly affect the quality of the produced datasets in terms of precision and accuracy. Another conclusion concerns the sample dispersion effects occurring either in the sample transfer lines and the optical cavities of the laser spectrometers. When the measurement of multiple species is desired, a common practice is to "pigtail" laser spectrometers tuned for different gaseous species. This approach is however prone to leaks and pressure and flow instabilities that can significantly affect the quality of the measurement. As expected it also results in excess gas diffusion that decreases the obtained resolution.

Hereby we propose that the next step in online ice core measurements is the implementation of measurement platforms that can perform multicomponent analysis thus reducing the number of optical cavities and the total volume of sample transfer lines. The use of laser sources in the mid – IR especially using a Difference Frequency Generation (hereafter DFG) scheme allows for a wide range of tunabillity and can perform spectroscopic analysis in a region where fundamental ro-vibrational transitions are found. These transitions are

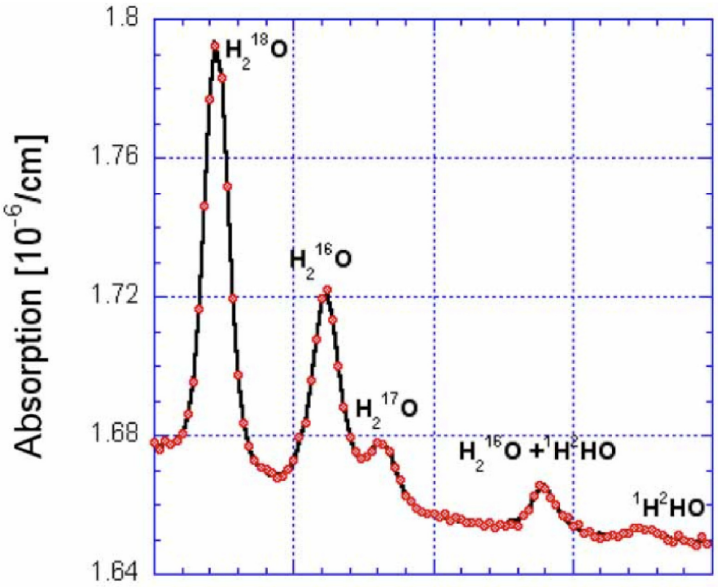

Figure 5.3: Laser scan with δ^{17}O line (Iannone et al., 2009a)

typically orders of magnitude stronger than the overtone transitions currently used for near-IR spectroscopy. These transitions could possibly yield useful measurements of gas isotopic species relevant for ice core science as $^{14}N^{15}N^{16}O$ and $^{13}C^{16}O_2$. In an ideal case several gas species including different isotopologues can be measured on the same sample in one optical cavity simplifying the whole measurement procedure and very likely allowing for a more reliable analytical system. The technologies required for this implementation are currently available and spectrometers implementing multi–component analysis in the mid – IR using DFG lasers have already been developed (Richter et al., 2009, 2000) but not seen commercial production yet. Possible implementation of these techniques must take into account the sample limitations apparent. With the current CFA system, the ice sample size and melt rates the avaiable sample is in the order of 1.5 scm^3 sec^{-1}. A multicomponent continuous flow analysis approach possibly replaces discrete measurements performed with conventional techniques that are demanding in terms of sample size. As a result, if we increase the ice sample size currently dedicated to CFA measurements, we can possibly achieve satisfactory sensitivity levels for more components and eventually contribute in preserving more ice from the core.

5.2 Set of high resolution data available

As a result of the measurement campaigns at the NEEM ice core drilling site, we now have several sections of the core measured in high resolution and precision for both δD and δ^{18}O . Data of methane concentrations are also available. Among the sections that we have measured we present here the water isotope

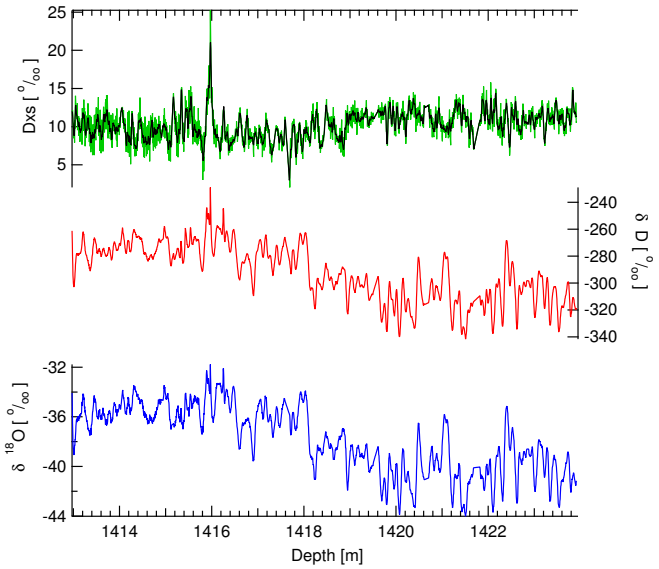

Figure 5.4: Younger Dryas Transition NEEM

record of the Younger Dryas and Bøllig Allerød transitions as well as the interstadial 19 (figures 5.4, 5.5, 5.6, 5.7 and 5.8). Apart from interesting data sets for studying climatic transitions based on the δ^{18}O , δD and D_{xs} signals, these data can be used in order to drive gas fractionation water isotope diffusion models over those transitions. Efforts on variability studies can also be foreseen.

In the depth range of approximately 2365 m to 2445 m one can observe a section where water isotope ratios and methane concentrations reach interglacial levels (figure 5.7). It is still not clear if the integrity of this section has been disturbed by folds in the ice. From the online high resolution measurements though there is some indication that there is no age difference between the water isotopes and the methane concentrations record. This points to ice folding at the sharp transitions located at approximately 2364.5 m and 2442.3 m respectively. In figure 5.8 we present a detailed section of this part and point out the increased isotope variability combined with adjacent very high values of methane concentrations. We can foresee that more work will be carried out in the future on this particular section of the NEEM core making use of the online measurements we present here.

5.3 Future diffusion plans

5.3.1 Dome C project - Dual high resolution measurements over the transition

Based on the work presented in chapter 4 we were not able to draw solid conclusions regarding the temperature evolution over the Dome C site. The available 2.5 cm resolution data sets allow for the determination of the diffusion lengths

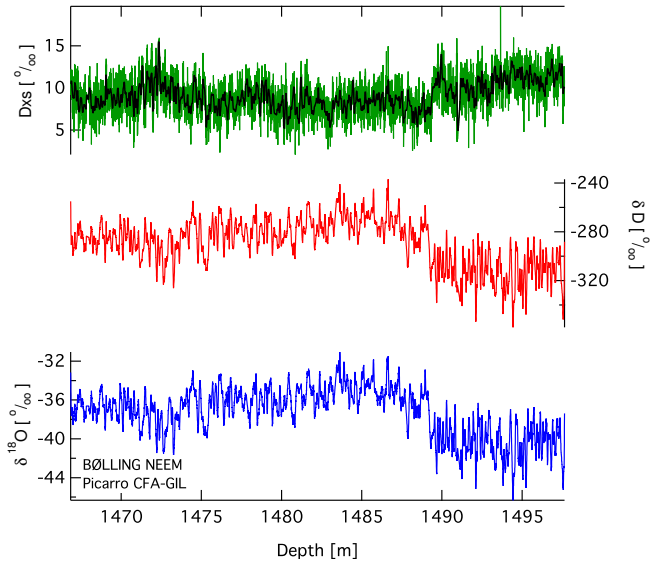

Figure 5.5: Bølling Transition NEEM

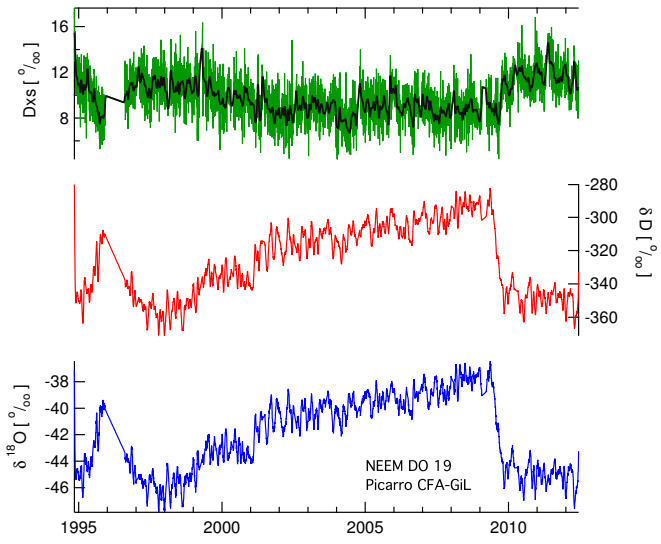

Figure 5.6: Interstadial 19 NEEM

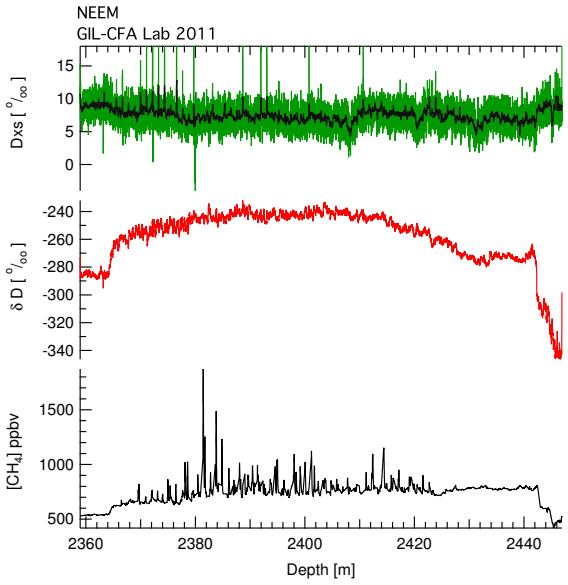

Figure 5.7: Super-Eemian NEEM

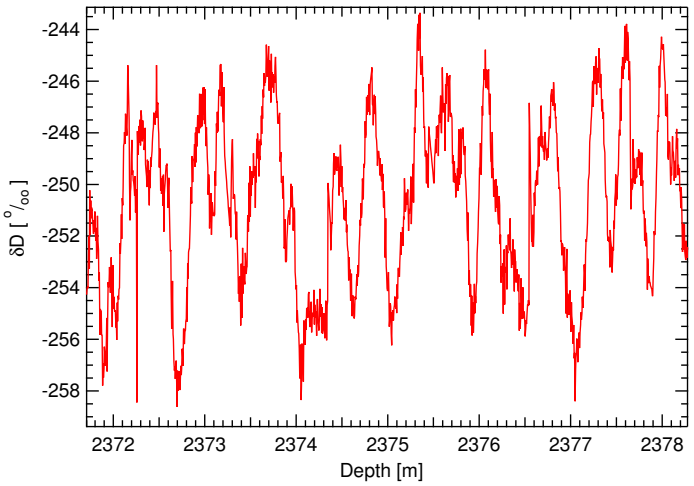

Figure 5.8: Detail Super-Eemian NEEM

for δ^{18}O and δD for only two points, before and after the last glacial termination. Additionally the 11 cm resolution dataset has only been analyzed for δ^{18}O and as a result the differential diffusion signal cannot be assessed. The resolution of 11 cm is also not high enough to allow for a good characterization of the spectral density. Thus the estimation of the noise level is not robust.

For those reasons sampling of the Dome C core for isotopes in a resolution higher than 5 cm will allow for better spectral estimation of the isotopic signal. Considering that combined δ^{18}O and δD measurements are nowadays easier to perform with laser spectroscopy such a dataset can be used to compare modeled and data based values of the diffusion lengths for both δ^{18}O and δD . In this way one can investigate the rather large data-model discrepancy observed for the differential diffusion signal (section 4.5.1).

We are currently working towards the direction of requesting additional samples from the Dome C core for discrete as well as continuous online measurements covering the glacial termination. By accessing both the δ^{18}O and δD diffusion signal we hope we can get a more precise estimate of the diffusion length values and thus a better insight on the evolution of the isotope slope from stage 5 until present.

5.3.2 The NEEM ice core data set

Upon completion, the NEEM water isotope data set will present combined δ^{18}O and δD measurements on a 2.5 cm and 5 cm resolution from the surface to the bottom of the ice core. This constitutes an ideal "workbench" for the application of diffusion models and data analysis methods. Parameters as the strain rates and the past accumulation will hopefully be better constrained due to the layer counted time scale that is under development for the core. The downside is that climatic events of particular interest as the Younger Dryas and the Bølling Allerød transitions, as well as a number of interstadial events, are found at a depth where based on the available borehole temperature profiles the ice diffusion is expected to smooth away any firn diffusion information.

In figure 5.9 we present an estimate of the firn diffusion lengths for δ^{18}O based on an assumed isotope slope of 0.5 and the borehole temperature profile measured at the end of the 2010 field season. Obviously the temperature profile we use is disturbed due to the preceded drilling activities, thus the ice diffusion estimates we present should be accordingly affected. However based on this current estimate we predict that the firn diffusion information below 1500 m will be lost due to ice diffusion. That indicates that single isotope diffusion based reconstructions are not possible for the Bølling – Allerød transition and most likely feasible for the Younger – Dryas transition. At this point and considering the availability of dual high resolution measurements from NEEM it would be very interesting to investigate the applicability of the differential diffusion signal as it can possibly overcome the problem of ice diffusion.

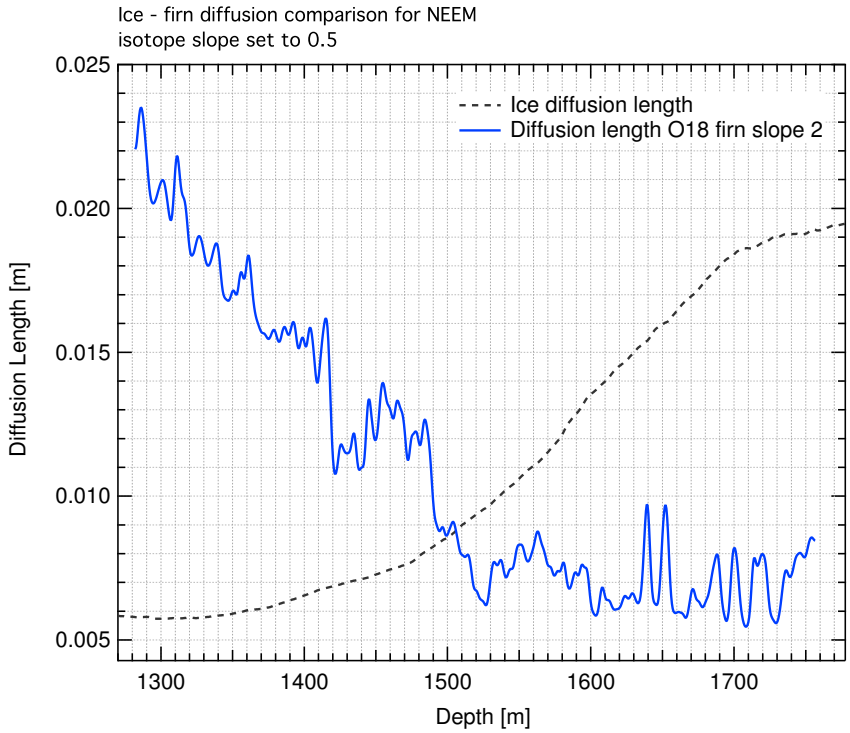

Figure 5.9: Expected ice and firn (δ^{18}O) diffusion lengths for the NEEM ice core. We use a fixed isotope slope of 0.5 and the borehole temperature profile measured at the end of the 2010 field season.

Appendix A

A simple Rayleigh fractionation model

A.1 A simple Rayleigh fractionation model

In this section we will describe a simple Rayleigh distillation model. Fractionation factors used here are all refer to the transition from liquid to vapour phase, thus $\alpha = \frac{R_L}{R_V}$. We assume a liquid water reservoir of isotopic composition $R_o = R_{smow}$ and an evaporation process with fractionation factor α_o at temperature T_o resulting in a vapor mass with isotopic composition

$$R_{vo} = \frac{R_{smow}}{\alpha_o} \tag{A.1}$$

A precipitation event as illustrated in figure A.1 will fractionate the remaining vapor mass. Assuming a slow process with immediate removal of dN molecules with isotopic composition αR_{vo} the number of abundant isotopologues and the isotopic composition for all three compounds will be:

- Initial vapor: $N_{vo},\ R_{vo}$
- Remaining vapor: $N - dN,\ R - dR$
- Formed compound: $dN,\ \alpha R$

Assuming mass balance for the rare isotopologues we get:

$$RN = (R - dR)(N - dN) + \alpha R dN \tag{A.2}$$

Which can be approximated to:

$$N dR = (\alpha - 1) R dN \tag{A.3}$$

$$\frac{dR}{R} = (\alpha - 1)\,\frac{dN}{N} \tag{A.4}$$

Assuming that α is independent of the variable N and by using the initial conditions $R_v = R_{vo},\ N = N_o$ the result of the integration is:

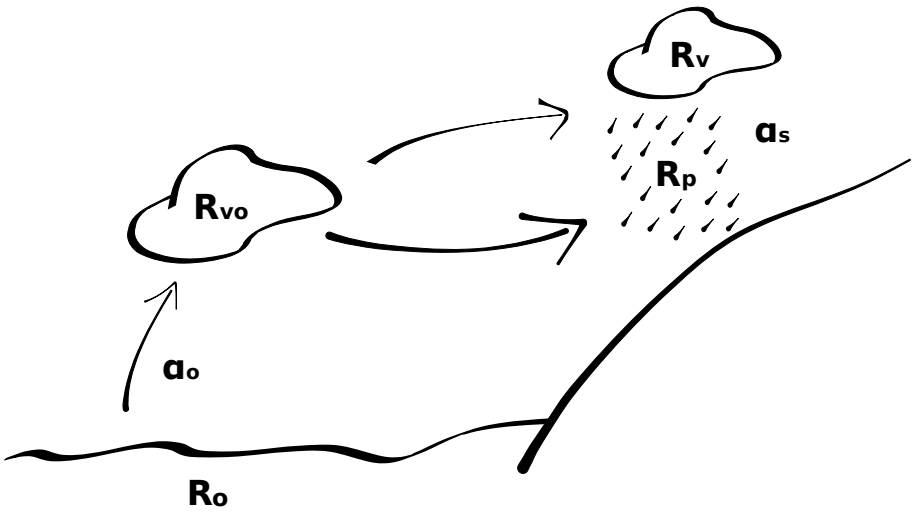

Figure A.1: Rayleigh scheme with varying source temperature

$$\frac{R_v}{R_{vo}} = \left(\frac{N}{N_{vo}}\right)^{\alpha-1} \tag{A.5}$$

The ratio N_v/N_{vo} is the remaining fraction f of the water vapor mass. When the water vapor mass is transported from the source site with temperature T_{source} to a sampling station with temperature T_{site} then following a simplified approach we can assume that adiabatic cooling by dT would relate relative changes of vapor pressure to relative changes in the amount of the abundant isotopologues (approximately equal to total number of water molecules) as:

$$\frac{dp}{p} = \frac{dN}{N} \Leftrightarrow \frac{p_v}{p_{vo}} = \frac{N_v}{N_{vo}} \tag{A.6}$$

We evaluate the vapor pressure at temperatures T_{source} and T_{site} using expressions from the excellent review of Murphy and Koop (2005). For temperatures above zero we use the vapor pressure over liquid water expression by Goff (1957).

$$\begin{aligned}\log\left(p_{liq}\right) = &-7.90298\left((373.16/T)-1\right) + 5.02808\log\left(373.16/T\right) \\ &- 1.3816\cdot 10^{-7}\left(10^{11.344(1-T/373.16)}-1\right) \\ &+ 8.1328\cdot 10^{-3}\left(10^{-3.49149(373.16/T-1)}-1\right) + \log(101325)\end{aligned} \tag{A.7}$$

$$p_{ice} = \exp\left(9.550426 - 5723.265/T + 3.53068\ln(T) - 0.00728332\ T\right) \tag{A.8}$$

For temperatures below zero we use a Clausius – Clapeyron expression that takes into account the temperature dependence of the latent heat of sublimation (Murphy and Koop, 2005). Both expressions A.7 and A.8 refer to pressure in

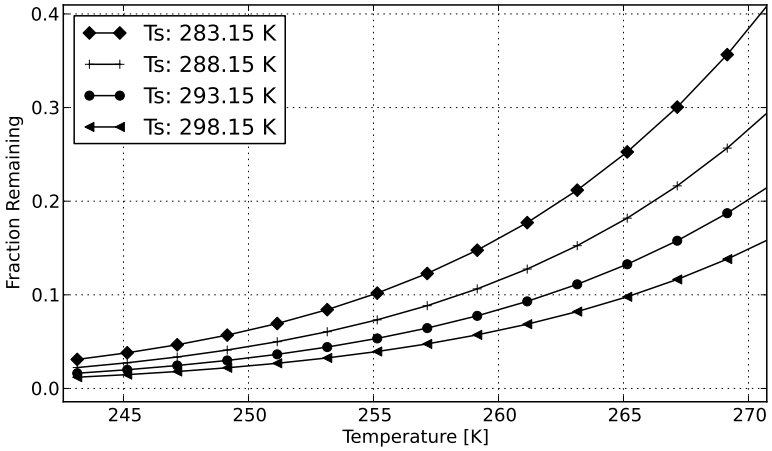

Figure A.2: Remaining fraction in a vapor mass for different source and site temperatures based on a Rayleigh scheme.

Pa. Considering the equations A.6, A.7, A.8 we calculate the remaining fraction based on various combinations of T_{source} and T_{site} as illustrated in figure A.2.

For the isotopic composition of the remaining vapor δ_v and the formed precipitation we consider the fractionation factors for evaporation (α_o) and condensation at the site (α_s) evaluated at the relevant temperatures T_{source} and T_{site}. We use the expressions of Majoube (1971) for the liquid to vapor transitions. For the solid to vapor transitions we use the formulations reported by Majoube (1971) and Melivat and Nief (1967) for $\alpha^2_{s/v}$ and $\alpha^{18}_{s/v}$ respectively. The work of Horita et al. (2008) constitutes a useful collective study of the available results on the determination of equilibrium and kinetic fractionation factors. The expressions we used are:

$$10^3 \ln \alpha_{L/V} \left({}^2\mathrm{H}/{}^1\mathrm{H}\right) = 52.612 - 76.248 \left(10^3/T\right) + 24.844 \left(10^6/T^2\right) \quad \text{(A.9)}$$

$$10^3 \ln \alpha_{L/V} \left({}^{18}\mathrm{O}/{}^{16}\mathrm{O}\right) = -2.0667 - 0.4156 \left(10^3/T\right) + 1.137 \left(10^6/T^2\right) \quad \text{(A.10)}$$

$$\ln \alpha_{Ice/Vapor} \left({}^2\mathrm{H}/{}^1\mathrm{H}\right) = 16288/T^2 - 9.34 \times 10^{-2} \quad \text{(A.11)}$$

$$\ln \alpha_{Ice/Vapor} \left({}^{18}\mathrm{O}/{}^{16}\mathrm{O}\right) = 11.839/T - 28.224 \times 10^{-3} \quad \text{(A.12)}$$

In order to use the analytical solution of eq. A.4 we consider a fixed value for α_m corresponding to a temperature $T_m = \left(T_{source} + T_{site}\right)/2$. Numerical integration of eq. A.4 with appropriate calculation of α_m would result to a more

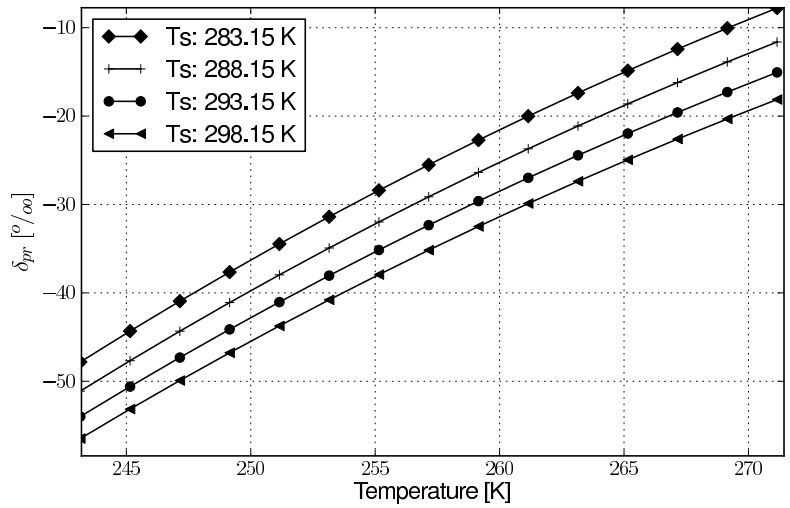

Figure A.3: Isotopic content of precipitation expressed in ‰values

realistic result. Hereby we calculate the isotopic composition of the remaining vapor and the formed precipitate as:

$$\delta_v = \frac{R_v}{R_{smow}} - 1 = \frac{R_{vo}}{R_{smow}} f^{(\alpha_m - 1)} \tag{A.13}$$

Considering $R_{vo} = \alpha_o^{-1} R_{smow}$ and $R_p = \alpha_s R_v$ we then write:

$$\delta_v = \alpha_o^{-1} f^{(\alpha_m - 1)} - 1 \quad \text{and} \quad \delta_{pr} = \frac{a_s}{a_o} f^{(\alpha_m - 1)} - 1 \tag{A.14}$$

In figures A.3 we illustrate the results of the Rayleigh model for δ^{18}O . The effect of the source temperature is clear on the isotopic composition of the precipitate. One can also observe the non linear response of the isotopic signal to changes in temperature of the precipitation site. We would like to point out again that this model assumes only equilibrium conditions. Diffusive effects are not considered and thus the δ^{18}O values calculated here represent only an approximation to reality. Though for illustrational purposes only the model qualitatively describes the process of evaporation - transport and precipitation.

For meteoric waters, a linear relationship between δ^{18}O and δD is observed described by eq. A.15 (Dansgaard, 1964; Craig, 1965; Mook, 2000) commonly known as the “meteoric water line”. Deviations from the 10‰ translated meteoric water line are reffered to as the deuterium excess quantity and described in eq. A.16.

$$\delta\mathrm{D} = 8 \times \delta^{18}\mathrm{O} + 10 \tag{A.15}$$

$$\mathrm{D_{xs}} = \delta\mathrm{D} - 8 \times \delta^{18}\mathrm{O} \tag{A.16}$$

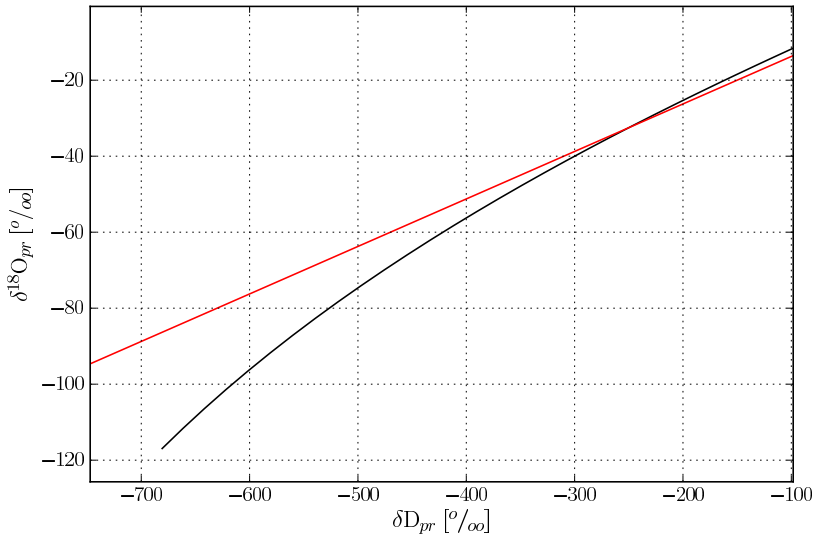

Figure A.4: Meteroric water line (red) compared to the prediction of a simple Rayleigh model (black)

A seen in figure A.4 the meteoric line expected from the Rayleigh fractionation model shows a non linear behavior in the regime of high depletion levels. This is an effect that is imposed by the combination of mass balance for the rare isotopologues and the stronger fractionation factors observed for δD as compared to δ^{18}O . As a result, we show that assuming an equilibrium Rayleigh fractionation scheme as demonstrated in this section, when working in the regime of very depleted precipitation, one needs to consider the non linear response of δ^{18}O to changes of δD and thus equation A.16 should be used with caution.

Bibliography

Abramowitz, M. and Stegun, I. A.: Handbook of Mathematical Functions with Formulas, Graphs, and Mathematical Tables, Dover, New York, ninth dover printing, tenth gpo printing edn., 1964.

Allan, D. W.: Statistics of atomic frequency standards, Proceedings of the IEEE, 54, 221–230, 1966.

Andersen, N.: Calculation Of Filter Coefficients For Maximum Entropy Spectral Analysis, Geophysics, 39, 69–72, 1974.

Arnaud, L., Barnola, J. M., and Duval, P.: Physical modeling of the densification of snow/firn and ice in the upper part of polar ice sheets, in: Physics of ice core records, pp. 285 – 305, Hokkaido University Press, 2000.

Barkan, E. and Luz, B.: High precision measurements of O-17/O-16 and O-18/O-16 ratios in H2O, Rapid Communications In Mass Spectrometry, 19, 3737–3742, doi:10.1002/rcm.2250, 2005.

Begley, I. S. and Scrimgeour, C. M.: High-precision δ^2H and δ^{18}O measurement for water and volatile organic compounds by continuous-flow pyrolysis isotope ratio mass spectrometry, Analytical Chemistry, 69, 1530–1535, 1997.

Berden, G., Peeters, R., and Meijer, G.: Cavity ring-down spectroscopy: Experimental schemes and applications, International Reviews In Physical Chemistry, 19, 565–607, 2000.

Bigeleisen, J., Perlman, M. L., and Prosser, H. C.: Conversion Of Hydrogenic Materials To Hydrogen For Isotopic Analysis, Analytical Chemistry, 24, 1356–1357, 1952.

Brand, W. A., Geilmann, H., Crosson, E. R., and Rella, C. W.: Cavity ring-down spectroscopy versus high-temperature conversion isotope ratio mass spectrometry; a case study on δ^2H and δ^{18}O of pure water samples and alcohol/water mixtures, Rapid Communications in Mass Spectrometry, 23, 1879–1884, URL `http://dx.doi.org/10.1002/rcm.4083`, 2009.

Brown, D. E. and George, S. M.: Surface and bulk diffusion of (H2O)-O-18 on single-crystal (H2O)-O-16 ice multilayers, Journal of Physical Chemistry, 100, 15 460–15 469, doi:10.1021/jp952670a, 1996.

Burg, J. P.: Maximum entropy spectral analysis, Ph.D. thesis, Stanford University, 1975.

Caillon, N., Severinghaus, J. P., Jouzel, J., Barnola, J. M., Kang, J. C., and Lipenkov, V. Y.: Timing of atmospheric CO2 and Antarctic temperature changes across termination III, Science, 299, 1728–1731, doi: 10.1126/science.1078758, 2003.

Craig, H., Gordon, L. I., and Horibe, Y.: Isotopic Exchange Effects In Evaporation Of Water .1. Low-Temperature Experimental Results, Journal Of Geophysical Research, 68, 5079–&, 1963.

Craig, H. & Gordon, L. I.: Deuterium and oxygen 18 variations in the ocean and the marine atmosphere., in: Stable Isotopes in Oceanographic Studies and Paleotemperatures, edited by Tongiorgi, E., pp. 9–130, Laboratorio di Geologia Nucleare, Pisa, Italy, 1965.

Crosson, E. R.: A cavity ring-down analyzer for measuring atmospheric levels of methane, carbon dioxide, and water vapor, Applied Physics B-Lasers And Optics, 92, 403–408, 2008.

Cuffey, K. M. and Vimeux, F.: Covariation of carbon dioxide and temperature from the Vostok ice core after deuterium-excess correction, Nature, 412, 523–527, 2001.

Cuffey, K. M., Alley, R. B., Grootes, P. M., and Anandakrishnan, S.: Toward Using Borehole Temperatures To Calibrate An Isotopic Paleothermometer In Central Greenland, Global And Planetary Change, 98, 265–268, 1992.

Cuffey, K. M., Alley, R. B., Grootes, P. M., Bolzan, J. M., and Anandakrishnan, S.: Calibration Of The Delta-O-18 Isotopic Paleothermometer For Central Greenland, Using Borehole Temperatures, Journal Of Glaciology, 40, 341–349, 1994.

Czerwinski, F., Richardson, A. C., and Oddershede, L. B.: Quantifying Noise in Optical Tweezers by Allan Variance, Optics Express, 17, 13 255–13 269, 2009.

Dahl Jensen, D. and Johnsen, S. J.: Paleotemperatures Still Exist In The Greenland Ice-Sheet, Nature, 320, 250–252, 1986.

Dahl Jensen, D., Mosegaard, K., Gundestrup, N., Clow, G. D., Johnsen, S. J., Hansen, A. W., and Balling, N.: Past temperatures directly from the Greenland Ice Sheet, Science, 282, 268–271, 1998.

Dansgaard, W.: Stable isotopes in precipitation, Tellus, 16, 436–468, 1964.

Dansgaard, W., Clausen, H., Gundestrup, N., Hammer, C., Johnsen, S., Kristinsdottir, P., and Reeh, N.: A new Greenland deep ice cores, Science, 218, 1273, 1982.

Dreyfus, G. B., Jouzel, J., Bender, M. L., Landais, A., Masson-Delmotte, V., and Leuenberger, M.: Firn processes and delta N-15: potential for a gas-phase climate proxy, Quaternary Science Reviews, 29, 28–42, 2010.

Epstein, S. Mayeda, T.: Variations of ^{18}O content of waters from natural sources., Geochimica Cosmochimica Acta, 4, 213?224, 1953.

Fuhrer, K., Neftel, A., Anklin, M., and Maggi, V.: Continuous Measurements Of Hydrogen-Peroxide, Formaldehyde, Calcium And Ammonium Concentrations Along The New Grip Ice Core From Summit, Central Greenland, Atmospheric Environment Part A-General Topics, 27, 1873–1880, 1993.

Gehre, M., Hoefling, R., Kowski, P., and Strauch, G.: Sample preparation device for quantitative hydrogen isotope analysis using chromium metal, Analytical Chemistry, 68, 4414–4417, 1996.

Gehre, M., Geilmann, H., Richter, J., Werner, R. A., and Brand, W. A.: Continuous flow H-2/H-1 and and(18)O/O-16 analysis of water samples with dual inlet precision, Rapid Communications In Mass Spectrometry, 18, 2650–2660, 2004.

Gkinis, V., Popp, T. J., Johnsen, S. J., and Blunier, T.: A continuous stream flash evaporator for the calibration of an IR cavity ring-down spectrometer for the isotopic analysis of water, Isotopes In Environmental and Health Studies, 46, 463–475, doi:10.1080/10256016.2010.538052, 2010.

Gkinis, V., Popp, P. J., Blunier, T., Bigler, M., Schüpbach, S., and Johnsen, S.: Water isotopic ratios from a continuously melted ice core sample, accepted to Atmospheric Measurement Techniques, 2011.

Goff, J. A.: Saturation pressure of water on the new Kelvin scale, Trans. Am. Soc. Heating Air-Cond. Eng., 63, 347–354, 1957.

Goujon, C., Barnola, J. M., and Ritz, C.: Modeling the densification of polar firn including heat diffusion: Application to close-off characteristics and gas isotopic fractionation for Antarctica and Greenland sites, Journal Of Geophysical Research-Atmospheres, 108, 4792, 2003.

Gupta, P., Noone, D., Galewsky, J., Sweeney, C., and Vaughn, B. H.: Demonstration of high-precision continuous measurements of water vapor isotopologues in laboratory and remote field deployments using wavelength-scanned cavity ring-down spectroscopy (WS-CRDS) technology, Rapid Communications In Mass Spectrometry, 23, 2534–2542, 2009.

Hall, W. D. and Pruppacher, H. R.: Survival of Ice Particles Falling From Cirrus Clouds In Subsaturated Air, Journal of the Atmospheric Sciences, 33, 1995–2006, doi:10.1175/1520-0469(1976)033¡1995:TSOIPF¿2.0.CO;2, 1976.

Hayes, M. H.: Statistical digital signal processing and modeling, John Wiley & Sons, 1996.

Herron, M. M. and Langway, C. C.: Firn Densification - An Empirical-Model, Journal Of Glaciology, 25, 373–385, 1980.

Horita, J., Rozanski, K., and Cohen, S.: Isotope effects in the evaporation of water: a status report of the Craig-Gordon model, Isotopes In Environmental and Health Studies, 44, 23–49, doi:10.1080/10256010801887174, 2008.

Huber, C. and Leuenberger, M.: Fast high-precision on-line determination of hydrogen isotope ratios of water or ice by continuous-flow isotope ratio mass spectrometry, Rapid Communications In Mass Spectrometry, 17, 1319–1325, 2003.

Iannone, R. Q., Kassi, S., Jost, H.-J., Chenevier, M., Romanini, D., Meijer, H. A. J., Dhaniyala, S., Snels, M., and Kerstel, E. R. T.: Development and airborne operation of a compact water isotope ratio infrared spectrometer, Isotopes in Environmental and Health Studies, pp. –, URL http://www.informaworld.com/10.1080/10256010903172715, 2009a.

Iannone, R. Q., Romanini, D., Kassi, S., Meijer, H. A. J., and Kerstel, E. R. T.: A Microdrop Generator for the Calibration of a Water Vapor Isotope Ratio Spectrometer, Journal Of Atmospheric And Oceanic Technology, 26, 1275–1288, 2009b.

Jean-Baptiste, P., Jouzel, J., Stievenard, M., and Ciais, P.: Experimental determination of the diffusion rate of deuterated water vapor in ice and application to the stable isotopes smoothing of ice cores, Earth And Planetary Science Letters, 158, 81–90, 1998.

Johnsen, S.: Stable isotope homogenization of polar firn and ice, Isotopes and impurities in snow and ice, pp. 210–219, 1977.

Johnsen, S. J., Dansgaard, W., and White, J. W. C.: The origin of Arctic precipitation under present and glacial conditions., Tellus, 41B, 452–468, 1989.

Johnsen, S. J., Clausen, H., Dansgaard, W., Fuhrer, K., Gundestrup, N., Hammer, C., Iversen, P., Jouzel, J., Stauffer, B., and Steffensen, J.: Irregular glacial interstadials recorded in a new Greenland ice core, Nature, 359, 311–313, 1992.

Johnsen, S. J., Clausen, H. B., Cuffey, K. M., Hoffmann, G., Schwander, J., and Creyts, T.: Diffusion of stable isotopes in polar firn and ice. The isotope effect in firn diffusion, in: Physics of Ice Core Records, edited by Hondoh, T., pp. 121–140, Hokkaido University Press, Sapporo, 2000.

Johnsen, S. J., DahlJensen, D., Gundestrup, N., Steffensen, J. P., Clausen, H. B., Miller, H., Masson-Delmotte, V., Sveinbjornsdottir, A. E., and White, J.: Oxygen isotope and palaeotemperature records from six Greenland ice-core stations: Camp Century, Dye-3, GRIP, GISP2, Renland and NorthGRIP, Journal Of Quaternary Science, 16, 299–307, 2001.

Jouzel, J. and Merlivat, L.: Deuterium and oxygen 18 in precipitation: modeling of the isotopic effects during snow formation, Journal of Geophysical Research-Atmospheres, 89, 11 749 – 11 759, 1984.

Jouzel, J., Alley, R. B., Cuffey, K. M., Dansgaard, W., Grootes, P., Hoffmann, G., Johnsen, S. J., Koster, R. D., Peel, D., Shuman, C. A., Stievenard, M., Stuiver, M., and White, J.: Validity of the temperature reconstruction from water isotopes in ice cores, Journal Of Geophysical Research-Oceans, 102, 26 471–26 487, 1997.

Jouzel, J., Masson-Delmotte, V., Cattani, O., Dreyfus, G., Falourd, S., Hoffmann, G., Minster, B., Nouet, J., Barnola, J. M., Chappellaz, J., Fischer, H., Gallet, J. C., Johnsen, S., Leuenberger, M., Loulergue, L., Luethi, D., Oerter, H., Parrenin, F., Raisbeck, G., Raynaud, D., Schilt, A., Schwander, J., Selmo, E., Souchez, R., Spahni, R., Stauffer, B., Steffensen, J. P., Stenni,

B., Stocker, T. F., Tison, J. L., Werner, M., and Wolff, E. W.: Orbital and millennial Antarctic climate variability over the past 800,000 years, Science, 317, 793–796, 2007.

Kaufmann, P. R., Federer, U., Hutterli, M. A., Bigler, M., Schüpbach, S., Ruth, U., Schmitt, J., and Stocker, T. F.: An Improved Continuous Flow Analysis System for High-Resolution Field Measurements on Ice Cores, Environmental Science & Technology, 42, 8044–8050, 2008.

Kavanaugh, J. L. and Cuffey, K. M.: Generalized view of source-region effects on delta D and deuterium excess of ice-sheet precipitation, Annals Of Glaciology, Vol 35, 35, 111–117, 2002.

Kawamura, K.: Variations of atmospheric components over the past 340,000 years from Dome Fulj deep ice core, Antarctica, Ph.D. thesis, Tohoku University, Japan, 2000.

Kay, S. M. and Marple, S. L.: Spectrum Analysis - A Modern Perspective, Proceedings Of The Ieee, 69, 1380–1419, 1981.

Kerstel, E. R. T.: Handbook of Stable Isotope Analytical Techniques, vol. 1, Elsevier B.V., Amsterdam, 2005.

Kerstel, E. R. T., van Trigt, R., Dam, N., Reuss, J., and Meijer, H. A. J.: Simultaneous determination of the $^{2}H/^{1}H$, $^{17}O/^{16}O$ and $^{18}O/^{16}O$ isotope abundance ratios in water by means of laser spectrometry, Analytical Chemistry, 71, 5297–5303, 1999.

Kerstel, E. R. T., Iannone, R. Q., Chenevier, M., Kassi, S., Jost, H. J., and Romanini, D.: A water isotope (^{2}H,^{17}O,^{18}O) spectrometer based on optical feedback cavity-enhanced absorption for in situ airborne applications, Applied Physics B-Lasers And Optics, 85, 397–406, 2006.

Landais, A., Barnola, J. M., Masson-Delmotte, V., Jouzel, J., Chappellaz, J., Caillon, N., Huber, C., Leuenberger, M., and Johnsen, S. J.: A continuous record of temperature evolution over a sequence of Dansgaard-Oeschger events during Marine Isotopic Stage 4 (76 to 62 kyr BP), Geophysical Research Letters, 31, L22 211, doi:10.1029/2004GL021193, 2004.

Landais, A., Barnola, J. M., Kawamura, K., Caillon, N., Delmotte, M., Van Ommen, T., Dreyfus, G., Jouzel, J., Masson-Delmotte, V., Minster, B., Freitag, J., Leuenberger, M., Schwander, J., Huber, C., Etheridge, D., and Morgan, V.: Firn-air delta N-15 in modern polar sites and glacial-interglacial ice: a model-data mismatch during glacial periods in Antarctica?, Quaternary Science Reviews, 25, 49–62, 2006.

Landais, A., Barkan, E., and Luz, B.: Record of delta O-18 and O-17-excess in ice from Vostok Antarctica during the last 150,000 years, Geophysical Research Letters, 35, L02 709, 2008.

Lang, C., Leuenberger, M., Schwander, J., and Johnsen, S.: 16C Rapid Temperature Variation in Central Greenland 70,000 Years Ago, Science, 286, 934–937, doi:10.1126/science.286.5441.934, URL `http://www.sciencemag.org/content/286/5441/934.abstract`, 1999.

Lee, X. H., Sargent, S., Smith, R., and Tanner, B.: In situ measurement of the water vapor O-18/O-16 isotope ratio for atmospheric and ecological applications, Journal Of Atmospheric And Oceanic Technology, 22, 555–565, 2005.

Lis, G., Wassenaar, L. I., and Hendry, M. J.: High-precision laser spectroscopy D/H and O-18/O-16 measurements of microliter natural water samples, Analytical Chemistry, 80, 287–293, 2008.

Lorius, C., Merlivat, L., and Hagenmann, R.: Variation In Mean Deuterium Content of Precipitations In Antarctica, Journal of Geophysical Research, 74, 7027–&, doi:10.1029/JC074i028p07027, 1969.

Luz, B. and Barkan, E.: Variations of 17O/16O and 18O/16O in meteoric waters, Geochimica et Cosmochimica Acta, 74, 6276 – 6286, doi:DOI: 10.1016/j.gca.2010.08.016, URL http://www.sciencedirect.com/science/article/B6V66-50T9X19-2/2/53f7e265670a81fe7c83 2010.

Majoube, M.: Fractionation In O-18 Between Ice And Water Vapor, Journal De Chimie Physique Et De Physico-Chimie Biologique, 68, 625–&, 1971.

Masson-Delmotte, V., Jouzel, J., Landais, A., Stievenard, M., Johnsen, S. J., White, J. W. C., Werner, M., Sveinbjornsdottir, A., and Fuhrer, K.: GRIP deuterium excess reveals rapid and orbital-scale changes in Greenland moisture origin RID A-7845-2009, Science, 309, 118–121, doi: 10.1126/science.1108575, 2005.

McManus, J. B. and Kebabian, P. L.: Narrow Optical Interference-fringes For Certain Setup Conditions In Multipass Absorption Cells of the Herriott Type, Applied Optics, 29, 898–900, 1990.

Meijer, H. A. J. and Li, W. J.: The use of electrolysis for accurate delta O-17 and delta O-18 isotope measurements in water, Isotopes In Environmental And Health Studies, 34, 349–369, 1998.

Melivat, L. and Nief, G.: Fractionnement Isotopique Lors Des Changements Detat Solide-Vapeur Et Liquide-Vapeur De Leau A Des Temperatures Inferieures A 0 Degrees C, Tellus, 19, 122–&, 1967.

members, N.: High-resolution record of Northern Hemisphere climate extending into the last interglacial period, Nature, 431, 147–151, 2004.

Merlivat, L. and Jouzel, J.: Global Climatic Interpretation of the Deuterium-Oxygen 18 Relationship for Precipitation, J. Geophys. Res., 84(C8), 5029–5033, 1979.

Mook, W.: Environmental Isotopes in the Hydrological Cycle: Principles and Applications, vol. I, IAEA, Unesco and IAEA, 2000.

Morville, J., Kassi, S., Chenevier, M., and Romanini, D.: Fast, low-noise, mode-by-mode, cavity-enhanced absorption spectroscopy by diode-laser self-locking, Applied Physics B-Lasers And Optics, 80, 1027–1038, 2005.

Murphy, D. M. and Koop, T.: Review of the vapour pressures of ice and supercooled water for atmospheric applications, Quarterly Journal Of The Royal Meteorological Society, 131, 1539–1565, 2005.

O'Keefe, A., Scherer, J. J., and Paul, J. B.: cw Integrated cavity output spectroscopy, Chemical Physics Letters, 307, 343–349, doi:10.1016/S0009-2614(99)00547-3, 1999.

Oppenheim, A. V.: Signals & Systems, Prentice Hall, 1997.

Parrenin, F., Barnola, J.-M., Beer, J., Blunier, T., Castellano, E., Chappellaz, J., Dreyfus, G., Fischer, H., Fujita, S., Jouzel, J., Kawamura, K., Lemieux-Dudon, B., Loulergue, L., Masson-Delmotte, V., Narcisi, B., Petit, J.-R., Raisbeck, G., Raynaud, D., Ruth, U., Schwander, J., Severi, M., Spahni, R., Steffensen, J. P., Svensson, A., Udisti, R., Waelbroeck, C., and Wolff, E.: The EDC3 chronology for the EPICA Dome C ice core, Climate of the Past, 3, 485–497, URL `http://www.clim-past.net/3/485/2007/`, 2007a.

Parrenin, F., Dreyfus, G., Durand, G., Fujita, S., Gagliardini, O., Gillet, F., Jouzel, J., Kawamura, K., Lhomme, N., Masson-Delmotte, V., Ritz, C., Schwander, J., Shoji, H., Uemura, R., Watanabe, O., and Yoshida, N.: 1-D-ice flow modelling at EPICA Dome C and Dome Fuji, East Antarctica, Climate Of The Past, 3, 243–259, 2007b.

Ramseier, R. O.: Self-Diffusion Of Tritium In Natural And Synthetic Ice Monocrystals, Journal Of Applied Physics, 38, 2553–&, 1967.

Rasmussen, S. O., Andersen, K. K., Johnsen, S. J., Bigler, M., and McCormack, T.: Deconvolution-based resolution enhancement of chemical ice core records obtained by continuous flow analysis, Journal Of Geophysical Research-Atmospheres, 110, doi:10.1029/2004JD005 717, 2005.

Rasmussen, S. O., Andersen, K. K., Svensson, A. M., Steffensen, J. P., Vinther, B. M., Clausen, H. B., Siggaard-Andersen, M. L., Johnsen, S. J., Larsen, L. B., Dahl-Jensen, D., Bigler, M., Rothlisberger, R., Fischer, H., Goto-Azuma, K., Hansson, M. E., and Ruth, U.: A new Greenland ice core chronology for the last glacial termination, Journal Of Geophysical Research-Atmospheres, 111, 10.1029/2005JD006 079, 2006.

Richter, D., Lancaster, D. G., and Tittel, F. K.: Development of an automated diode-laser-based multicomponent gas sensor, Applied Optics, 39, 4444–4450, doi:10.1364/AO.39.004444, 2000.

Richter, D., Fried, A., and Weibring, P.: Difference frequency generation laser based spectrometers, Laser & Photonics Reviews, 3, 343–354, doi: 10.1002/lpor.200810048, 2009.

Romanini, D., Chenevier, M., Kassi, S., Schmidt, M., Valant, C., Ramonet, M., Lopez, J., and Jost, H. J.: Optical-feedback cavity-enhanced absorption: a compact spectrometer for real-time measurement of atmospheric methane RID C-6602-2008, Applied Physics B-lasers and Optics, 83, 659–667, doi: 10.1007/s00340-006-2177-2, 2006.

Röthlisberger, R., Bigler, M., Hutterli, M., Sommer, S., Stauffer, B., Junghans, H. G., and Wagenbach, D.: Technique for continuous high-resolution analysis of trace substances in firn and ice cores, Environmental Science & Technology, 34, 338–342, 2000.

Schüpbach, S., Federer, U., Kaufmann, P. R., Hutterli, M. A., Buiron, D., Blunier, T., Fischer, H., and Stocker, T. F.: A New Method for High-Resolution Methane Measurements on Polar Ice Cores Using Continuous Flow Analysis, Environmental Science & Technology, 43, 5371–5376, doi:10.1021/es9003137, 2009.

Schwander, J., Stauffer, B., and Sigg, A.: Air mixing in firn and the age of air at pore close-off, Annals Of Glaciology, 10, 141–145, 1988.

Schwander, J., Sowers, T., Barnola, J. M., Blunier, T., Fuchs, A., and Malaize, B.: Age scale of the air in the summit ice: Implication for glacial-interglacial temperature change, Journal Of Geophysical Research-Atmospheres, 102, 19 483–19 493, 1997.

Schwander, J., Jouzel, J., Hammer, C. U., Petit, J. R., Udisti, R., and Wolff, E.: A tentative chronology for the EPICA Dome Concordia ice core, Geophysical Research Letters, 28, 4243–4246, 2001.

Severinghaus, J. P. and Brook, E. J.: Abrupt climate change at the end of the last glacial period inferred from trapped air in polar ice, Science, 286, 930–934, 1999.

Severinghaus, J. P., Sowers, T., Brook, E. J., Alley, R. B., and Bender, M. L.: Timing of abrupt climate change at the end of the Younger Dryas interval from thermally fractionated gases in polar ice, Nature, 391, 141–146, 1998.

Severinghaus, J. P., Albert, M. R., Courville, Z. R., Fahnestock, M. A., Kawamura, K., Montzka, S. A., Muhle, J., Scambos, T. A., Shields, E., Shuman, C. A., Suwa, M., Tans, P., and Weiss, R. F.: Deep air convection in the firn at a zero-accumulation site, central Antarctica, Earth and Planetary Science Letters, 293, 359–367, doi:10.1016/j.epsl.2010.03.003, 2010.

Sigg, A., Fuhrer, K., Anklin, M., Staffelbach, T., and Zurmuhle, D.: A Continuous Analysis Technique For Trace Species In Ice Cores, Environmental Science & Technology, 28, 204–209, 1994.

Steffensen, J., Andersen, K., Bigler, M., Clausen, H., Dahl-Jensen, D., Fischer, H., Goto-Azuma, K., Hansson, M., Johnsen, S., Jouzel, J., Masson-Delmotte, V., Popp, T. J., Rasmussen, S. O., R othlisberger, R., Ruth, U., Stauffer, B., Siggaard-Andersen, M. L., Sveinbjörnsdóttir, A., Svensson, A., and White, J. W. C.: High-resolution Greenland ice core data show abrupt climate change happens in few years, Science, 321, 680–684, 2008.

Ulmke, H., Wriedt, T., and Bauckhage, K.: Piezoelectric droplet generator for the calibration of particle-sizing instruments, Chemical Engineering & Technology, 24, 265–268, 2001.

Van der Wel, L. G., Gkinis, V., Pohjola, V. A., and Meijer, H. A. J.: Snow isotope diffusion rates measured in a laboratory experiment, Journal of Glaciology, 57, 30–38, 2011.

Vaughn, B. H., White, J. W. C., Delmotte, M., Trolier, M., Cattani, O., and Stievenard, M.: An automated system for hydrogen isotope analysis of water, Chemical Geology, 152, 309–319, 1998.

Waelbroeck, C., Labeyrie, L., Michel, E., Duplessy, J. C., McManus, J. F., Lambeck, K., Balbon, E., and Labracherie, M.: Sea-level and deep water temperature changes derived from benthic foraminifera isotopic records, Quaternary Science Reviews, 21, 295–305, doi:10.1016/S0277-3791(01)00101-9, 2002.

Wang, L. X., Caylor, K. K., and Dragoni, D.: On the calibration of continuous, high-precision delta O-18 and delta H-2 measurements using an off-axis integrated cavity output spectrometer, Rapid Communications In Mass Spectrometry, 23, 530–536, 2009.

Werle, P., Mucke, R., and Slemr, F.: The Limits Of Signal Averaging In Atmospheric Trace-Gas Monitoring By Tunable Diode-Laser Absorption-Spectroscopy (Tdlas), Applied Physics B-Photophysics And Laser Chemistry, 57, 131–139, 1993.

Whillans, I. and Grootes, P.: Isotopic diffusion in cold snow and firn, Journal of Geophysical Research, 90, 3910–3918, 1985.

Wiener, N.: Time Series, The MIT Press, Cambridge, Massachussetts, 1949.